2016

Investigating the Thermal and Phase Stability of Nanocrystalline Ni-W Produced by Electrodeposition, Sputtering, and Mechanical Alloying

Christopher Jonathan Marvel
Lehigh University

Investigating the Thermal and Phase Stability of Nanocrystalline Ni-W Produced by Electrodeposition, Sputtering, and Mechanical Alloying

by

Christopher Jonathan Marvel

A Dissertation
Presented to the Graduate and Research Committee
of Lehigh University
in Candidacy for the Degree of
Doctor of Philosophy

in

Materials Science and Engineering

Lehigh University

May 2016

Certificate of Approval

Approved and recommended for acceptance as a dissertation in partial fulfillment of the requirements for the degree of Doctor of Philosophy

Christopher Jonathan Marvel

Investigating the Thermal and Phase Stability of Nanocrystalline Ni-W Produced by Electrodeposition, Sputtering, and Mechanical Alloying

_____

Defense Date

_____

Approved Date

Committee Members:

_____

Dr. Martin P. Harmer
Chairperson, Professor, Lehigh University

_____

Dr. Masashi Watanabe
Professor, Lehigh University

_____

Dr. Richard P. Vinci,
Professor, Lehigh University

_____

Dr. Michael Widom,
Professor, Carnegie Mellon University

Acknowledgements

I need to thank several people for their help throughout this research. I express my greatest gratitude to my advisor Dr. Martin Harmer who is a terrific mentor. He has supported me immensely, shared his scientific philosophy with me, and has given me numerous opportunities to grow as a scientist. I would also like to thank the dissertation committee members, Professors Masashi Watanabe, Rick Vinci, and Mike Widom for their guidance, and the Office of Naval Research for financial support.

Other individuals that directly contributed to my scientific development were Dr. Patrick Cantwell and Dr. Animesh Kundu. Patrick taught me the intricacies of electron microscopy and to best summarize my results in journal papers and presentations, and Animesh taught me my lab common sense which was desperately needed.

I would also like to thank my group members: Denise Yin, Abby Lawrence, Apple Schumacher, Yan Wang, and Mike Kracum. Denise was especially instrumental and completed all of electrodeposition and processing that was done at Lehigh. I could not have finished nearly as much work as I did without her help. Thanks Denise! It was also a pleasure to work with the other graduate students in the department. Among them, two students that contributed to this research were Wanjun Cao, who completed the initial fracture toughness testing, and Dan Bechetti, who completed the DICTRA calculations. Several undergraduate students also helped, including Nora Stack, Nadia Krook, Andrew Caferra, and Austin Keller. The technical staff was also very helpful, including Mike Rex, Rob Keyse, Bill Mushock, and Laura Moyer. They all expertly maintained the machine shop, microscopy suite, and metallography labs and answered all my questions. The

support staff was also critical. Sue, Katrina, Lisa, and Janie have all kept me on track from the time I was an undergrad.

Several collaborators were also of great help. Jian Luo and his student Yuanyao Zhang electrodeposited the first round of Ni-W alloys. Mike Widom and his students Qin Gao and Sanxi Yao conducted thermodynamic calculations that clarified Ni-W phase diagrams. Kris Darling and Chad Hornbuckle at the Army Research Laboratory provided mechanically alloyed Ni-W samples and discussions with them were very fruitful.

Most importantly, I would like to acknowledge my parents Richard and Nancy Marvel. They provided a nurturing childhood and supported my education and I would not be here today if it were not for them. And of course, I would like to thank my fiancé Carly Geronimo. She has given me the happiness that I need to succeed and is ALWAYS willing to edit my writing and tell me when I am wrong. Her support has been incredible, and I hope that I can provide as much support while she is finishing her graduate studies.

Table of Contents

List of Tables

List of Figures

Abstract

The development of nanocrystalline materials has been increasingly pursued over the last few decades. They have been shown to exhibit superior properties compared to their coarse-grain counterparts, and thus present a tremendous opportunity to revolutionize the performance of nanoscale devices or bulk structural materials. However, nanocrystalline materials are highly prone to grain growth, and if the nanocrystalline grains coarsen, the beneficial properties are lost. There is a strong effort to determine the most effective thermal stability mechanisms to avoid grain growth, but the physical nature of nanocrystalline grain growth is still unclear due to a lack of detailed understanding of nanocrystalline microstructures. Furthermore, the influence of contamination has scarcely been explored with advanced transmission electron microscopy techniques, nor has there been a direct comparison of alloys fabricated with different bulk processes. Therefore, this research has applied aberration-corrected scanning transmission electron microscopy to characterize nanocrystalline Ni-W on the atomic scale and elucidate the physical grain growth behavior. Three primary objectives were pursued: (1) explore the thermal stability mechanisms of nanocrystalline Ni-W, (2) evaluate the phase stability of Ni-W and link any findings to grain growth behavior, and (3) compare the influences of bulk fabrication processing, including electrodeposition, DC magnetron sputtering, and mechanical alloying, on the thermal stability and phase stability of Ni-W.

Several thermal stability mechanisms were identified throughout the course of this research. First and foremost, W-segregation was scarcely observed to grain boundaries, and it is unclear if W-segregation improves thermal stability contrary to most reports in the

literature. Long-range Ni_4W chemical ordering was observed in alloys with more than 20 at.% W, and it is likely Ni_4W domains reduce grain boundary mobility. In addition, lattice diffusivity calculations conceptually suggested that increasing W alloying concentrations can decrease the grain growth rate. The strongest evidence of grain growth stagnation was via nanoscale oxide particle drag in highly contaminated electrodeposited alloys. Interestingly, W-segregation was also detected to the oxide phase boundaries and revealed a potential indirect mechanism of thermal stability.

The phase stability of pure and contaminated Ni-W alloys was investigated with density functional theory. Primarily, the calculations suggested that the intermetallic phases NiW and NiW_2 are thermodynamically unstable, meaning the binary phase diagram is incorrect, but the ternary carbides Ni_6W_6C and Ni_2W_4C are stable. Several Ni-W binary and Ni-W-C ternary phase diagrams were constructed using a simplified CALPHAD approach to improve the understanding of Ni-W phase stability. Lastly, it was determined that the fabrication process greatly influences the impurity types and concentrations of the alloys, and therefore greatly dictate which thermal stability mechanisms are active. Mechanically alloyed samples were found to be the most resistant to grain growth.

The findings of this research will hopefully guide future efforts to design more thermally stable nanocrystalline alloys. The link between phase stability and grain growth behavior of Ni-W was thoroughly discussed, as well as the dependence of bulk fabrication processing on the contamination found in the alloys. Ultimately, this research has greatly expanded the general understanding of nanocrystalline Ni-W microstructures, and it is likely that similar phenomena occur in other nanocrystalline systems.

Chapter 1 Introduction

Many fundamental properties of polycrystalline materials depend on the average grain size of the microstructure. This grain size relationship is especially important in nanocrystalline materials, which have an average grain size of less than 100 nm [1]. Nanocrystalline materials are of great scientific interest because they have been shown to exhibit superior properties compared to their bulk counterpart with larger grain sizes. In some cases nanograin materials are at least three times stronger than materials of the same composition but with grain sizes larger than 1 μm [2]. The unique properties of nanocrystalline materials is attributed to the relatively higher volume fraction of grain boundaries. Nanocrystalline materials with an average grain size of ~10 nm have a volume fraction of ~27%, whereas coarse-grain materials are considered to have a negligible volume fraction [3]. Unfortunately, due to the high volume fractions of grain boundaries, the driving force for nanocrystalline grain growth is amplified. Therefore, minimizing grain growth and maintaining their beneficial properties proves extremely challenging.

Thermal stability mechanisms that prevent nanocrystalline grain growth have been reviewed by several authors [4–6]. There are two main strategies that have garnered the most attention. The first strategy utilizes kinetic mechanisms that decrease grain boundary mobility, such as solute drag, reduced diffusivity, particle drag, and chemical ordering. The second strategy utilizes solute segregation to reduce the grain boundary energy and consequently the driving force. However, the most efficient thermal stability mechanisms are constantly debated, and it remains unknown which mechanisms are the most effective at limiting nanocrystalline grain growth.

Determining if one system is kinetically or thermodynamically stabilized is complicated. The small length scales of nanocrystalline materials increases the difficulty in characterizing them, and in some cases, stability mechanisms have not yet been decoupled. For instance, both solute drag and the thermodynamic mechanism require solute segregation, but it is unclear if reduced grain growth is attributed to solute drag or a reduction in the grain boundary energy. It is also possible that several thermal stability mechanisms collectively reduce grain growth, but again, it is difficult to determine the contribution of each individual mechanism.

The predictability of nanocrystalline thermal stability is also complex. Many assumptions are used to design nanocrystalline materials, but they are not always accurate and research must be conducted to modify them. One misleading assumption is that impurities do not greatly influence the thermal stability mechanisms, nor the phase stability of nanocrystalline microstructures. If impurities are present, they can directly alter the thermodynamics and kinetics of nanocrystalline grain growth and thereby diminish the predictability of alloy design. Another misguided assumption is that the thermal stability mechanisms of any given material are the same regardless of the bulk fabrication process. However, different fabrication processes can introduce varying levels or types of impurities, which then may alter the phase stability and the thermal stability mechanisms.

One methodology to identify the thermal stability mechanisms, evaluate the phase stability, and accurately compare different bulk fabrication processes of any particular material system is to apply high resolution techniques that can directly observe nanocrystalline microstructures. This suggestion was best expressed by Saber *et al.* [7]:

> "Atomic scale resolution for structure and chemistry of solute segregation to grain boundaries and precipitation of nanoscale phases, for example by the use of atom probe tomography or high-resolution scanning transmission electron microscopy, is necessary to confirm the relevance and interplay of thermodynamic and kinetic mechanisms." [7]

Unfortunately, and contrary to their suggestion, a limited number of studies have actually used these atomic resolution techniques to determine which stability mechanisms are the most prevalent. Therefore, this research applied aberration-corrected scanning transmission electron microscopy to characterize nanocrystalline microstructures on the atomic scale and determine the influence of impurities and processing on the thermal stability mechanisms of nanocrystalline Ni-W. Nanocrystalline Ni-W was chosen as the material system because the thermal stability mechanisms are heavily debated.

Chapter 2 Background

This chapter summarizes the nanocrystalline literature that is the most relevant to this research. First, the unique behavior of nanocrystalline materials will be discussed. Next, the fundamental laws of grain growth and the central thermal stability strategies to limit grain growth will be outlined. Then, previous research on the thermal stability of nanocrystalline Ni-W will be presented. Lastly, the influence of fabrication methods on thermal and phase stability will be reviewed.

2.1 Nanocrystalline Materials

Gleiter and Suryanarayana defined nanocrystalline materials (*i.e.* average grain size less than 100 nm) as a new class of disordered solids due to the high amount of grain boundaries [1,3,8,9]. Nanocrystalline materials sometimes contain 100x higher volume fractions of intercrystalline regions than materials with average grain sizes larger than 1 μm. Assuming that grains are spherical and the material is fully crystalline, Figure 2.1a shows the volume fraction of intercrystalline regions as a function of grain size. Here the total intercrystalline region is the sum of the grain boundaries and triple junctions [3]. When the grain size is reduced to less than 20 nm, 10% of the atoms within the microstructure are located in grain boundaries. Similarly, once the grain size is less than 5 nm, 10% of the atoms are in triple junctions. Once so many grain boundaries and triple junctions are introduced into a material, the atomic structure of the grain boundaries and intercrystalline regions become increasingly disordered. Figure 2.1b is a schematic of nanocrystalline grains where the white circles represent atoms on the grain boundaries and black circles are atoms in the grains [3]. Note that the grain boundaries do not have the

same symmetry as more ordered grain boundaries, and the free volume between the nanocrystalline grains may also be increased compared to larger grained materials.

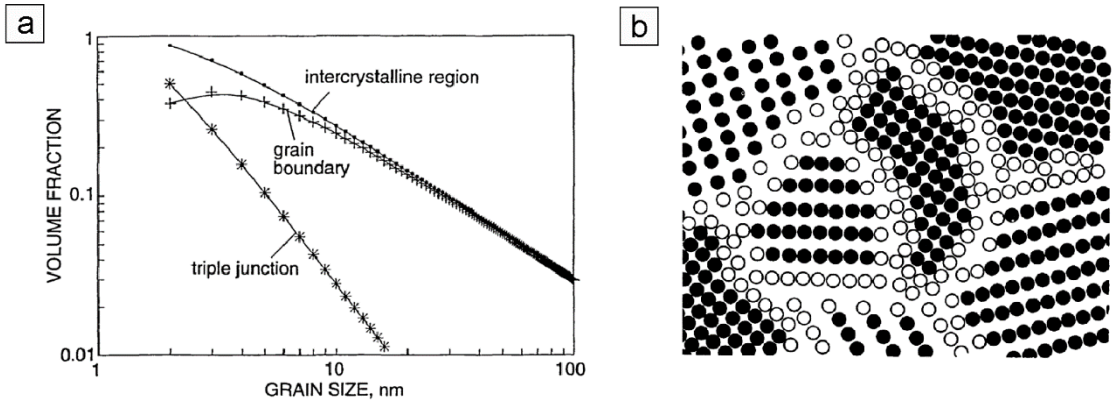

Figure 2.1. (a) Effect of grain size on intercrystalline, grain boundary, and triple junction regions assuming a grain boundary width of 1 nm, and (b) schematic of nanocrystalline grains showing the high disorder on the grain boundaries [3].

The high number of grain boundaries and increased free volume undoubtedly change the fundamental behaviors of nanocrystalline materials. One unique behavior is the Hall-Petch relationship where material hardness increases with decreasing grain size. The concept here is that the grain boundaries impede dislocation motion and shield the material against plastic deformation. Figure 2.2 shows a Hall-Petch plot of several Ni based nanocrystalline materials [10]. The y-axis is the hardness measured in GPa, and the x-axis is inverse root of the grain size. The maximum strength shown in Figure 2.2 was ~9 GPa from a Ni-W alloy with an average grain size of ~10 nm. If the grain size is increased to over 100 nm, the hardness is reduced to ~1 GPa. Otherwise if the grain size is decreased to below 7 nm, an inverse Hall-Petch effect occurs where the hardness declines with decreasing grain size. Here, the grain size approaches the amorphous limit, and the mechanical behavior is different.

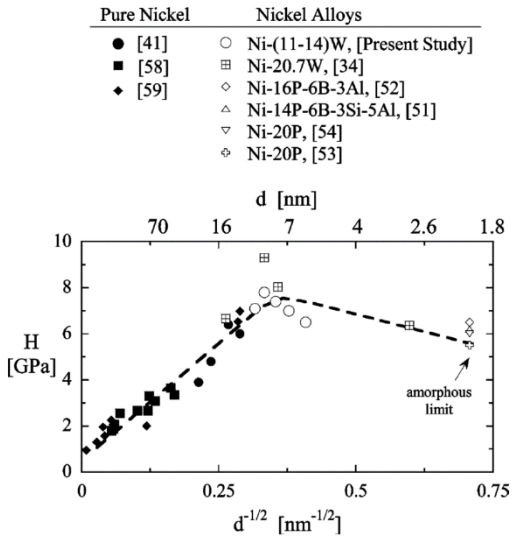

Figure 2.2. Hall-Petch hardness plot of Ni-based alloys showing that strength significantly decreases with increasing grain size [10].

Another potential nanocrystalline phenomenon is significantly faster bulk diffusion. Throughout this thesis, bulk diffusion is defined as the sum of lattice, grain boundary, and triple junction diffusion. Intergranular regions are high diffusion pathways, and since there is a significantly higher volume fraction of intergranular regions in nanocrystalline materials, the bulk diffusion should increase in nanocrystalline materials [9]. In one case Schumacher *et al.* showed that the diffusion of Ag in nanocrystalline Cu was 2-4 orders of magnitude faster than grain boundary diffusion in Cu bi-crystals [11]. Now, the question is whether grain boundary diffusion itself is faster, possibly due to more free volume in highly disordered grain boundaries, or if there is another unique behavior of nanocrystalline materials. For example, Dillon *et al.* argued that diffusion along grain boundaries does not depend on the grain size, and therefore there is not a scaling effect of grain size on grain boundary diffusion [12]. On the other hand, it could also be argued that the diffusion along triple junctions must be considered since the volume fraction of triple

junctions increases with decreasing grain size [13]. In this case, the overall bulk diffusion should increase because diffusion along triple junctions is even higher than diffusion along grain boundaries. High strength and increased diffusivity are both fundamentally important aspects, but there are also several other that are unique to nanocrystalline materials compared to coarse-grain materials.

While the fundamental behaviors of nanocrystalline materials are relatively unknown, there are many recognized applications for nanocrystalline materials. Due to their high strength, nanograin materials are often used as wear resistant coatings [14]. Rupert and Schuh have shown that the wear rate of 5 nm Ni-W was roughly half that of 105 nm Ni-W [15]. Other reports have discussed the possibility of using nanocrystalline materials because of their improved magnetic properties. Pal and Chakravorty have shown that coercivity is decreased with decreasing grain size in barium hexaferrite at temperatures below 300 K [16]. Furthermore, nanocrystalline Ni has been shown to be a viable corrosion resistant material that could be used as a chemical barrier. For instance, Mishra and Balasubramaniam observed that the corrosion rate of 8 nm Ni was 25% of the corrosion rate of 61 μm Ni in a sulfuric acid bath [17].

The most important limitation of nanocrystalline materials is that grain growth occurs with minimal temperature or pressure. If grain growth occurs, the beneficial properties of nanocrystalline materials are lost. For instance, pure Pd with an average grain size of 9 nm has been shown to coarsen to at least 50 nm after one day at room temperature [18]. This grain size trend is shown in Figure 2.3. In accordance with the Hall-Petch plot seen in Figure 2.2, this could mean the strength of originally 9 nm material could be cut in

half once the grain size reaches 50 nm. Understandably, this is a huge scientific problem. The following sections will define the laws of grain growth and present strategies to stabilize nanoscale grain sizes.

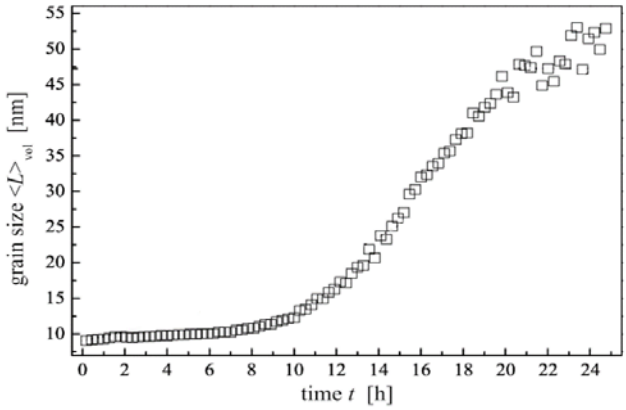

Figure 2.3. Room temperature grain growth of pure nanocrystalline Pd. Modified from [18].

2.2 Grain growth

Burke and Turnbull derived the classic law of grain growth assuming grain boundaries migrate because of curved interfaces [19]:

$$\upsilon = MF = M\gamma_b\kappa \quad (1)$$

where the grain boundary velocity (ν) depends on the mobility (M) and the driving force (F). The driving force can be further described as the product of the grain boundary energy (γ_b) and curvature of the grains (κ). The grain boundary mobility obeys Arrhenius behavior:

$$M = M_o exp\left[\frac{-Q}{k_B T}\right] \quad (2)$$

where the mobility depends on the pre-exponential mobility (M_o) multiplied by the exponential of the activation energy (Q) divided by Boltzmann's constant (k_B) and

temperature (T). Therefore, temperature has a strong influence on grain boundary velocity. The global driving force is to reduce the total grain boundary volume. Grain boundaries are usually the most energetic components of a microstructure and it is energetically favorable to remove them. In addition, curved grain boundaries induce local tensile and compressive stresses on the crystal lattice, so the local driving force for grain growth is to decrease grain curvature [20]. The proposed mechanism for grain growth is that atoms hop across grain boundaries to relieve the local pressure differences. Macroscopically, curvature driven grain growth dictates that the smallest grains shrink and the largest grains grow.

For a single phase microstructure that has a given average grain size, the grain growth rate is proportional to the average grain boundary velocity [21]:

$$\frac{d\bar{G}}{dt} = \alpha\bar{v}_b = \frac{D_b^{\perp} 2\gamma_b V_m}{\beta RT\bar{G}\omega} \tag{3}$$

where the grain growth rate ($\frac{d\bar{G}}{dt}$) depends on the diffusivity across the grain boundary ($D_b^{\perp}$), the grain boundary energy (γ_b), the molar volume (V_m), a proportionality constant (β), the universal gas constant (R), temperature (T), average grain radius ($\bar{G}$), and grain boundary thickness (ω). If Equation 2 is integrated from t to t_0, the difference between the final grain size and the original grain size is [21]:

$$\bar{G}^2 - \bar{G}_0^2 = \left[\frac{4D_b^{\perp}\gamma_b V_m}{\beta RT\omega}\right] t = kt \tag{4}$$

where the difference of the final grain size ($\bar{G}$) minus the original grain size ($\bar{G}_0$) depends on the variables described in Equation 2 multiplied by time (t). The variables in the square brackets are assumed to be constant, and are combined into a single rate constant (k).

Equations 2 and 3 define grain growth as a function of known material constants, but there are multiple simplifying assumptions: (1) all grain boundary energies in the microstructure are equal (despite differences in grain boundary character), (2) the grain size distribution follows a unimodal log-normal distribution, (3) all grain boundaries have similar widths, and (4) the grain boundaries are free of impurities. Predictably, experimental observations rarely match theoretical predictions. This paradox is especially true when considering nanocrystalline materials where even the atomic mechanisms of grain growth may be different. Instead of atom hopping across grain boundaries, grain rotation has been proposed where entire grains realign until they share a common crystal direction (*i.e.* the grain boundary is removed) [22,23]. Interestingly, grain rotation is a mechanism where the smallest grain sizes do not shrink, which is required for the curvature driven grain growth. In another report, Krill *et al.* observed that the grain growth rate is linear, not parabolic, in nanocrystalline Fe with an average grain size below 150 nm [24]. They attributed the difference to the excess free volume found in nanocrystalline materials. Ultimately, the atomic mechanisms of nanocrystalline grain growth are still unknown and it is possible that other unique behaviors have not yet been discovered.

There have been a few studies on nanocrystalline grain growth that have used in-situ TEM measurements to track the microstructural evolution. Hibbard *et al.* monitored nominally pure Ni grain growth at 420 °C and the results are shown in Figure 2.4. Their main observation was that grain growth progressed through cycles of normal and abnormal grain growth. The as-deposited alloy exhibited a uni-modal grain size distribution, then after annealing for ~1 sec several abnormal grains grew and produced a bi-modal grain size

distribution, afterwards the microstructure returned to a uni-modal distribution after annealing for 60 min. Remarkably, the abnormal grains after annealing for 11 hrs were orders of magnitude larger than the smaller matrix grains. The cause of abnormal grain growth was attributed to impurity sulfur segregation to the abnormal grain boundaries. Figure 2.5 shows a STEM-BF image of an abnormal grain boundary and two EDS spectra that compare the composition of the bulk grains and the grain boundary [25]. It is clear that there is more sulfur on the grain boundary than in the grain interior.

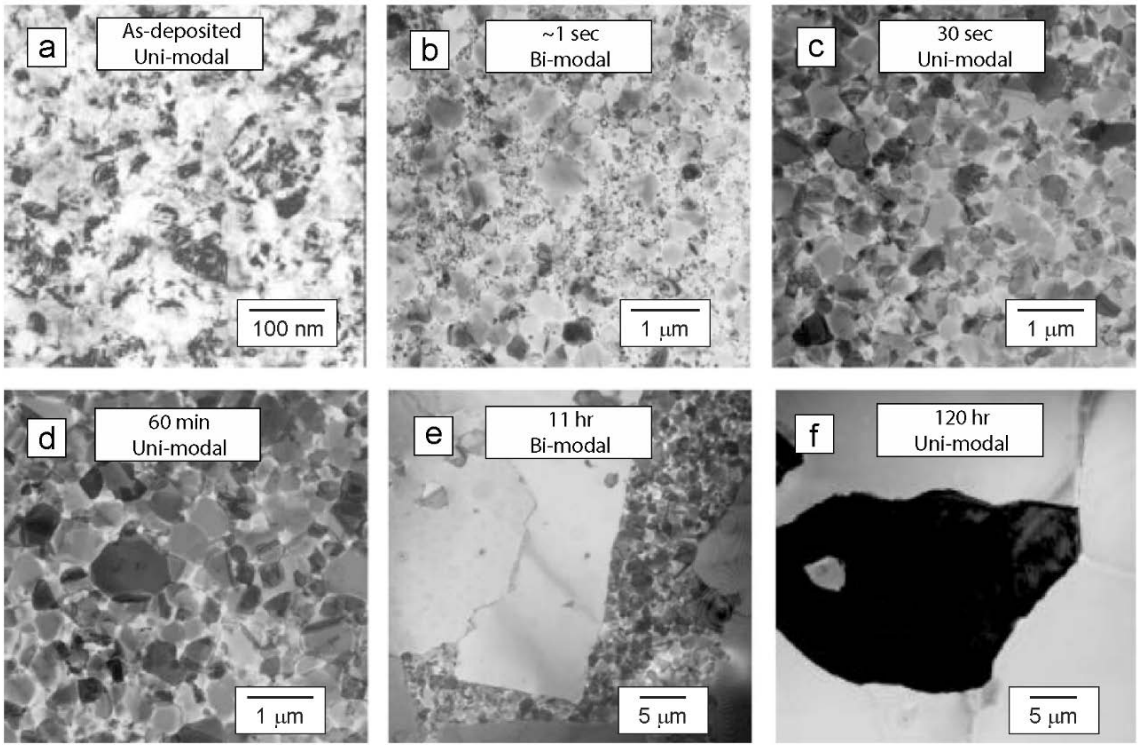

Figure 2.4. In-situ TEM grain size observations of nominally pure nanocrystalline Ni at 420 °C: (a) as-deposited, (b) after ~1 sec, (c) after 30 sec, (d) after 60 min, (e) after 11 hr, and (f) after 120 hr. All parts modified from [25].

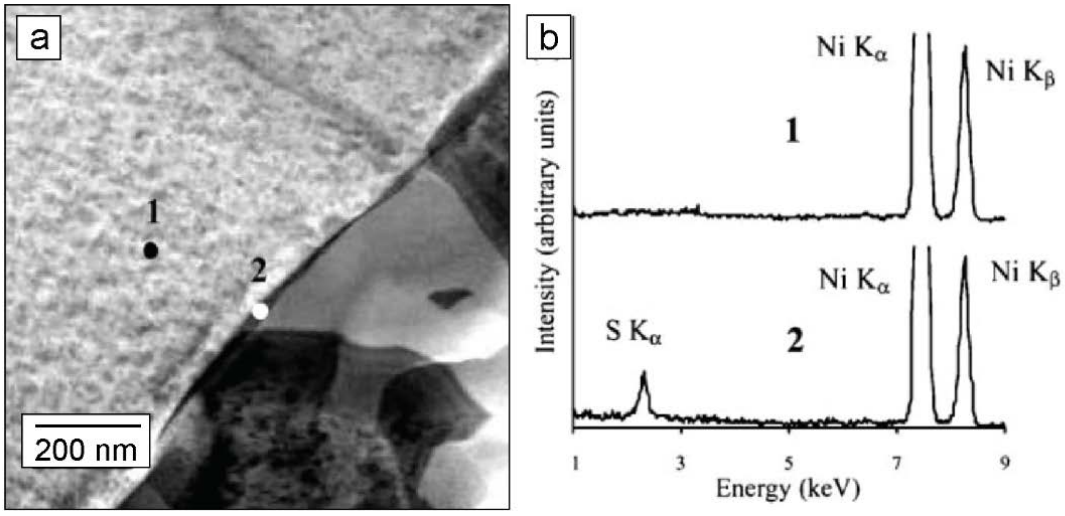

Figure 2.5. Confirmation of sulfur segregation in nominally pure Ni: (a) STEM-BF image showing abnormal grain boundary and the locations of the two EDS spectra shown in (b). Modified from [25].

Higher grain growth rates because of solute segregation have been extensively studied, especially in the ceramics community. Doping pure Al_2O_3 with SiO_2 and CaO has been shown to increase the grain boundary mobility, oftentimes two orders of magnitude [26]. Here, several grain boundary equilibrium structures were identified and called complexions. Each complexion exhibited different grain boundary mobilities, and contrary to the belief at the time, grain boundaries with more solute were significantly faster than the grain boundaries with the least amount of solute. More solute on the grain boundary should decrease the grain boundary velocity because of increasing solute drag effects (see section §2.3.2). Furthermore, this observation directly contradicts what is expected for the thermodynamic stabilization mechanism, which says that grain growth should be reduced because solute segregation lowers the grain boundary energy (see section §2.3.1). Nanocrystalline complexions and their corresponding transitions have not been thoroughly studied in the literature even though they are highly relevant to nanocrystalline grain growth. If a complexion transition grants a mobility advantage to some grain boundaries,

the microstructure can de-stabilize very quickly. Overall, the link between nanocrystalline grain boundary behavior and solute segregation is still unknown, and additional studies must be conducted to understand thermal stability mechanisms.

2.3 Thermal Stability Strategies

Equation 1 showed that grain boundary velocity depends on grain boundary mobility and the driving force. Thus, there are two viable routes to reduce grain boundary velocity: reduce grain boundary mobility with kinetic barriers, or lessen the thermodynamic driving force with solute segregation. This section will discuss the thermal stability strategies to limit nanocrystalline grain growth using the fundamental equations derived in section §2.2.

2.3.1 Thermodynamic Stabilization

The thermodynamic mechanism removes the global driving force for grain growth via solute segregation. The progression of the thermodynamic models that mathematically describe solute segregation in nanocrystalline materials was recently reviewed by Saber *et al.* [7]. It is important to highlight each model to understand the necessary assumptions included within them. The Gibbs adsorption isotherm shows the relationship between the free energy of the system and grain boundary energy:

$$dG = \gamma dA \tag{5}$$

where the change in the free energy of the system (dG) is related to the grain boundary energy (γ) and the change in grain boundary area. Thus, it is possible to reduce the total energy of the system by reducing the grain size or minimizing the grain boundary energy.

Since it is desired to keep grain growth to a minimum, the best case scenario is to reduce the grain boundary energy.

Weissmuller has shown that solute segregation can decrease grain boundary energy. Assuming the dilute solution limit and that grain boundary energy does not depend on crystal orientation [27,28]:

$$\gamma = \gamma_0 - \Gamma_{sat}[\Delta H_{seg} + RTlnx_b] \quad (6)$$

where γ_0 is the energy of a "clean" boundary, Γ_{sat} is solute excess assuming the grain boundary is fully saturated, ΔH_{seg} is the enthalpy of segregation, R is the gas constant, T is the temperature, and x_b is the bulk solute concentration. Kirchheim extended this model to determine an equilibrium grain size by assuming that a fully saturated grain boundary is covered by a monolayer of solute [29]:

$$\bar{G} = \frac{3\Gamma_{sat}V_M}{x_b} \quad (7)$$

where the grain diameter ($\bar{G}$) depends on the grain boundary saturation, molar volume (V_M), and the solute concentration. Of course, these models are restricted to highly segregating systems in the dilute limit, where it is assumed that all the solute is located on the grain boundaries and not dissolved in the solid solution or precipitated into secondary phases.

The next generation of models were more complex and included both chemical and elastic effects on the enthalpy of segregation to predict the equilibrium grain size. Please refer to the original publications for the complete derivation of the models. Darling *et al.* formulated a modified Wynblatt-Ku segregation model [30], and used elastic and mixing enthalpies to estimate the minimum grain boundary energy that is possible for each solute-solvent pair. Atwater and Darling also assumed a bi-layer grain boundary structure. While

their model captures the fundamentals of nanocrystalline segregation, there are many critical assumptions that must be emphasized. First, it is assumed that second phases do not precipitate (*e.g.* Ni_4W, Ni_6W_6C, or pure W). Second, the energetic effects of multispecies co-segregation are ignored (*e.g.* carbon and oxygen). The model also assumes the dilute limit and full grain boundary saturation. Because of these limitations, Atwater and Darling suggest that the use of their model should be coupled with binary phase diagrams to improve the physical accuracy of solute segregation in real material systems [31]. Atwater and Darling also constructed a database that compared 2288 distinct binary systems using their model [31]. Figure 2.6 shows the energetics of Ni-based nanocrystalline alloys.

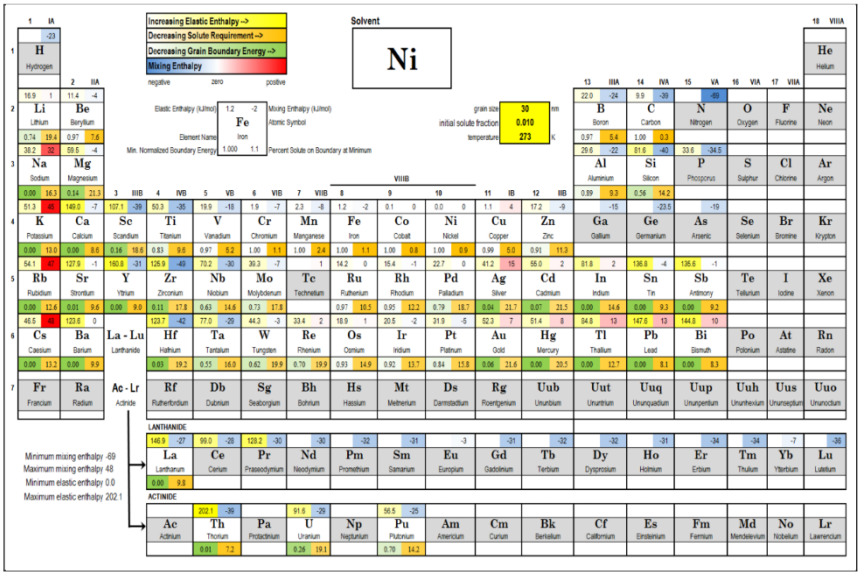

Figure 2.6. Solvent stability table of Ni-based nanocrystalline alloys derived by Atwater and Darlings using their free energy model [31].

Trelewicz and Schuh independently derived a regular solution model that overcame the dilute solution limit to study alloys that are not strongly segregating nor achieve fully saturated grain boundaries [32]. Despite these improvements, this model still assumes that

second phase formation is kinetically hindered (*e.g.* chemical ordering or precipitation), and in the cases where a high solute content is required, it is possible that in real systems the segregation mechanism may not work in favor of secondary phase formation. However, the high grain boundary volume of nanocrystalline materials provides more sites for the solute to occupy, meaning that the bulk thermodynamics presented on phase diagrams may not apply to nanocrystalline materials (*i.e.* nanograin materials can be super saturated with solute but still be deemed thermodynamically stable). Nonetheless, aware of the shortcomings of the Trelewicz-Schuh model, Murdoch and Schuh extended the regular solution model to include the enthalpy of mixing and identified material systems that are optimal for solute segregation *and* resistance to phase separation [33,34]. Interestingly, their results showed that a high enthalpy of segregation is not necessary, rather the ratio between the enthalpy of segregation and the enthalpy of mixing is crucial. Lastly, Saber *et al.* combined the approaches of Darling and Trelewicz-Schuh to generate the latest thermodynamic model for binary and ternary systems [35,36].

It is important to mention again that there are other assumptions integrated into these thermodynamic models that have not been resolved: the materials are fully crystalline (*i.e.* devoid of amorphous regions and pores), there are zero impurities in the lattice and on the grain boundaries that may alter the energetics of the enthalpies of mixing and segregation, and all grain boundaries have the same character, meaning each boundary has the same energy and accumulates the same amount of solute. Nonetheless, these models have built a theoretical foundation that has improved the overall understanding of solute segregation in nanocrystalline materials.

Several nanocrystalline systems have been designated as thermodynamically stable via solute segregation. Krill *et al.* studied nanocrystalline Pd-19 at.% Zr and observed that it was stable, or the XRD grain size was below 100 nm, up to 1125 °C after annealing for 24 hrs [37]. In addition, the lattice constant decreased over time and secondary phases were not detected, which indicated that Zr was segregating from the solid solution phase to the grain boundaries. Interestingly, Pd-Zr was also investigated by VanLeeuwen *et al.* to validate Krill's findings, and determined that while the grains were stable below 700 °C, grain growth was observed at higher temperatures after TEM characterization [38]. Another promising thermodynamic system is Fe-Zr that was investigated by Darling *et al.* [39]. They showed that 52 nm grains are stable after annealing at 913 °C with an addition of 4 at.% Zr.

2.3.2 Kinetic Stabilization

Kinetic stabilization mechanisms stagnate grain growth with kinetic barriers. Assuming solute segregates to the grain boundaries, solute drag can limit grain growth. Here, the grain boundary must carry the excess solute atoms as it moves, which counteracts the driving force for grain growth and consequently decreases the grain boundary velocity. The total drag force is described according to the following equation [40]:

$$F_b^t = F_b^0 + F_b^d \tag{8}$$

where the total drag force (F_b^t) is equal to the sum of the inherent driving force for grain boundary migration without solute segregation (F_b^0), which is simply v_b/M, and the solute drag force with solute segregation (F_b^d), which can be further defined as:

$$F_b^d = \frac{\alpha C_\infty v_b}{1 + \beta^2 v_b^2} \quad (9)$$

where the solute drag force (F_b^d) is related to the drag force for unit concentration of solute per unit velocity of a moving boundary (α), bulk solute concentration (C_∞), the grain boundary velocity (v_b), and the time required for solute atoms to diffuse one unit distance (β). Here α is approximately inversely proportional to the atomic diffusivity across the grain boundary, so a slower diffusing species will invoke a higher drag force. Finally, Equation 8 can be substituted into Equation 7:

$$F_b^t = F_b^0 + F_b^d = \frac{v_b}{M} + \frac{\alpha C_\infty v_b}{1 + \beta^2 v_b^2} \quad (10)$$

Another kinetic mechanism that has been shown to limit grain growth is Zener particle drag [21]. This mechanism argued that particles sitting on grain boundaries similarly decrease the total grain boundary velocity. The simplifying assumptions for this analysis include the following: that the particles are randomly distributed, that they are inert with the matrix, that they do not move nor coarsen, and that the particles are spherical. The maximum drag force limiting grain boundary velocity is:

$$F_b^p = \frac{3 f_v \gamma_b}{2r} \quad (11)$$

where the particle drag force (F_b^p) depends on the volume fraction of particles (f_v), the grain boundary energy, and the particle radius (r). If the particle drag force is equivalent to the intrinsic driving force, the limiting grain radius ($\bar{R}$) is:

$$\bar{R} = \frac{4r}{3 f_v} \quad (12)$$

There is some evidence that particle pinning is a viable method to limit nanocrystalline grain growth. It has been shown that nanocrystalline Cu-Zr can be stabilized with additions of a few at.% Zr where intermetallic Cu_5Zr and impurity ZrO_2 nanoscale particles migrated to the grain boundaries [41]. Dark field transmission electron microscopy was used to characterize the average grain and particle sizes, 29.5 nm and 3.5 nm, respectively, and it was determined that the average volume fraction required to counteract the intrinsic driving force was 2.4%. Overall, the authors argued that a particle volume fraction of 2.4% was within reason. Impurity phase particle pinning, similar to ZrO_2 in Cu-Zr, has recently been reviewed by Koch *et al.* [4]. Among the systems reviewed in the literature that benefited from particle pinning, impurity phases were identified as the most effective pinning agents, not the intentional intermetallic particles that are seen in equilibrium phase diagrams. For instance, Al_2O_3 and Al_4C_3 particles stagnated grain growth in pure Al up to 0.78 Tm, and Al_2O_3 and AlN particles stagnated grain growth in Fe-Al up to 0.68 Tm. While intentional phases precipitated, the formation of impurity phases may occur more often than currently realized (see section §5.5).

Another strategy to limit grain growth of nanocrystalline materials is to reduce the diffusivity of the solute and solvent atoms, either along or across the grain boundaries and through the lattice. According to the equations summarized in section §2.2, the grain growth rate depends on the atomic diffusivity across the grain boundary. Thus, if heavy solute atoms can be selectively placed on the grain boundaries by solute segregation, the grain growth rate can be greatly diminished. This scenario is similar to that explained above

regarding solute drag. Otherwise, heavy solute atoms located in the lattice can increase the activation energy, and consequently increase the onset temperature for grain growth.

Chemical ordering has been cited as another kinetic stability mechanism to reduce diffusivity through the lattice or a grain boundary [5]. Chemical ordering can exist as either short-range or long-range atomic configurations. Short-range ordering is generally classified as solid solution with non-random neighbors. Short-range ordering is also usually a pre-cursor for long-range ordering. Long range-ordering is a non-homogenous nucleation and growth process where ordered precipitates form in larger grains. This effect has been observed in Fe-Si and Fe-Si-Nb nanocrystals [42–44]. Furthermore, Bansal *et al.* have shown that short-range ordering decreases grain boundary mobility [42]. Figure 2.7 shows the non-monotonic decrease of grain boundary mobility with increasing short-range ordering. The degree of short-range ordering was determined by Mössbauer spectroscopy and the corresponding model-independent hyperfine magnetic field distributions.

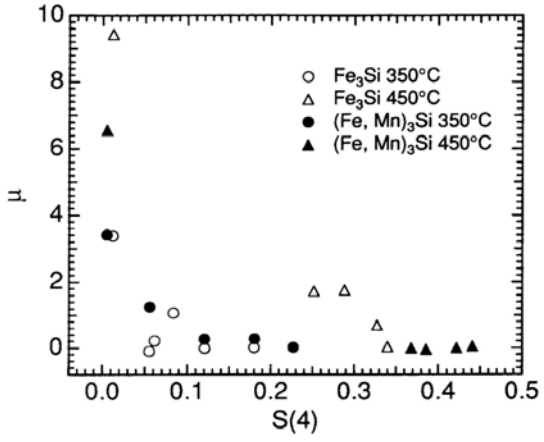

Figure 2.7. The relationship between grain boundary mobility (μ) and degree of short-range ordering (S(4)) in Fe_3Si and $(Fe,Mn)_3Si$ alloys [42].

2.3.3 Multiple Stability Mechanisms

Many experimental investigations of nanocrystalline materials conclude that multiple stability mechanisms simultaneously limit grain growth. If solute segregation is observed, it is possible that the combination of grain boundary energy reduction and solute drag slows grain growth [37]. In fact, it is unclear if the thermodynamic mechanism or solute drag is responsible for slowing grain growth, and to the present date, the effects of solute drag and grain boundary energy reduction have not been decoupled. Furthermore, when nanoscale particles are in a microstructure, it is possible that both solute and particle drag can reduce the grain growth rate. Ni-P and Cu-Ta are two materials systems that have exhibited several stability mechanisms. Nanoscale Ni_3P particles caused Zener pinning and P-segregation to Ni grain boundaries [45,46]. In Cu-Ta, Ta-segregation was hypothesized to limit grain growth at low temperatures, and at higher temperatures Ta dispersoids precipitated and pinned grain boundary motion [47,48].

2.4 Processing and Impurities

There are many fabrication processes to create nanocrystalline materials. However, there are vast differences in impurity concentrations and other unique microstructural characteristic between the many processes. The following sections will briefly outline the advantages and shortcomings of electrodeposition, DC magnetron sputtering, and mechanical alloying.

2.4.1 Electrodeposition

Electrodeposition is a common technique to produce nanocrystalline materials. Metallic salts are dissolved in aqueous or non-aqueous baths, combined with additives that

improve the quality of the films, and an electric field is applied to the bath to force the metallic ions towards the cathode to grow the film. One advantage of electrodeposition is that it produces practically dense materials. However, the microstructures are typically metastable and contamination is common. For instance, nominally pure electroplated Ni alloys can have up to 6000 wt. ppm of oxygen [49], or up to ~400 wt. ppm of carbon [50]. Consequently, there have been many efforts to produce high quality Ni films by altering the plating parameters [49–56]. The main parameters that have been adjusted to control Ni-W films include the bath temperature, the pH, and the electric field potential [57].

2.4.2 DC Magnetron Sputtering

DC magnetron sputtering is classified as physical vapor deposition and produces thin films that predominantly have a columnar microstructure [ref]. Sputtering is conceptually cleaner than electrodeposition or mechanical alloying; it is conducted under vacuum and the only sources of contamination are from the sputtering targets, the processing gas, or components installed in the sputtering chamber. The disadvantages of sputtered films are that the maximum film thickness is a few microns, the working gas can become trapped in the films, and residual stresses accumulate during deposition. The sputtering parameters that influence thin film growth and residual stress are listed below. Each parameter either influences the energy of the plasma gas or adatom mobility on the film surface [58]:

1. Sputtering temperature - higher temperatures give the adatoms more energy to migrate along the substrate surface. In addition, it has been shown that lower

sputtering temperatures reduce the columnar width of nanocrystalline Ni, but lower temperatures also expand the lattice parameters [59].

2. Working gas pressure - lower gas pressures limit the number of collisions between metallic ions and therefore increase the ionic momentum as it compacts the thin film surface. In pure W, films had -2.5 GPa or +1.5 GPa residual stresses after sputtering in Ar gas at pressures of ~2.5 mTorr or ~30 mTorr, respectively [60]. Furthermore, higher gas pressures reduce the sputtering rate but incorporate higher amounts of trapped gas bubbles.
3. Sputtering gun power - higher gun power creates higher ion fluxes off the sputtering targets and increases the film growth rate.
4. Substrate bias - higher substrate biases increase the momentum of the ions towards the substrate. Generally, the substrate bias and working gas pressure generate the same effects on residual stress where lower biases and pressures induce higher compressive stresses [58]. Detor et al. investigated the interplay between substrate bias and gas pressure on residual stress in great detail [61].

2.4.3 Mechanical Alloying

Mechanical alloying is defined as the continuous fracturing and cold welding of particulate materials [62]. Pure elemental or alloyed particles are milled until they are combined and the average grain size of the particles is decreased. In fact, the powders can be amorphized if the milling time is long enough [63], and the lattice parameter can increase because of increasing lattice strain or solute super-saturation during milling [62,64,65]. Mechanical alloying is considered a top-down approach and can produce up to

a few kilograms of powder, contrary to electrodeposition and sputtering that produce milligrams of material [66]. Therefore, mechanical alloying in the most promising fabrication process to produce bulk material. To exploit the bulk-scale manufacturing, the mechanically alloyed powders need to be consolidated with sintering or plastic deformation. However, grain growth commonly occurs during these processes because of the high processing temperatures and pressures. Another disadvantage of mechanical alloying is that contamination is much more prevalent. The main sources of contamination are native impurity layers on the particles that exist at the start of milling, and the fragmentation of the milling media [62,64]. Overall, the thermal stability mechanisms of mechanically alloyed materials may be much different than other fabrication techniques.

There are several milling parameters that can influence the purity of mechanically alloyed samples. First, the energy of the milling is important. The effects of a high energy shaker mill and a lower energy planetary mill on the microstructure of Ni-15 at.% W alloys were compared, and it was observed that the shaker mill produced greater amounts of impurity carbide formation [67]. A second important parameter is the composition of the milling vials and media. If stainless steel is used, it has been shown that impurity Fe concentrations of up to 60 at.% were incorporated into Ni-95 at.% W [68]. Another important parameter is the total milling time. Longer milling times decrease the particulate grain size until the amorphous limit is reached, but contamination also increases with time. Milling pure Ru for 8 hr, 16 hr, and 32 hr produced Fe contaminations of 3 at.%, 8 at.%, and 22 at.% from hardened steel balls, respectively [69]. Lastly, the atmosphere trapped in the milling vials is important. Since fresh particle surfaces are constantly created during

milling, light elements like carbon, oxygen, or nitrogen can become mixed into the bulk. In Al-25 at.% Ti, 10 wt.% O was incorporated after milling in air, but only 3 wt.% O was incorporated after milling in Ar [70].

2.5 Nanocrystalline Ni-W System

The Ni-W system has attracted much scientific interest for its high strength and corrosion resistance. Additionally, Ni-W is intriguing for its unresolved thermal stability mechanisms. Similar to Ni-P and Cu-Ta, it is likely that there are several active stability mechanisms and it is important to determine which mechanisms are the most prominent. A Ni-W binary phase diagram is shown in Figure 2.8 [71]. There is a large solid solubility limit of 12 at.% at room temperature. At higher W concentrations the intermetallics Ni_4W, NiW, and NiW_2 are stable up to ~1066 °C. Above 1066 °C, the intermetallics are unstable and there is a two-phase region of Ni(W) and pure W.

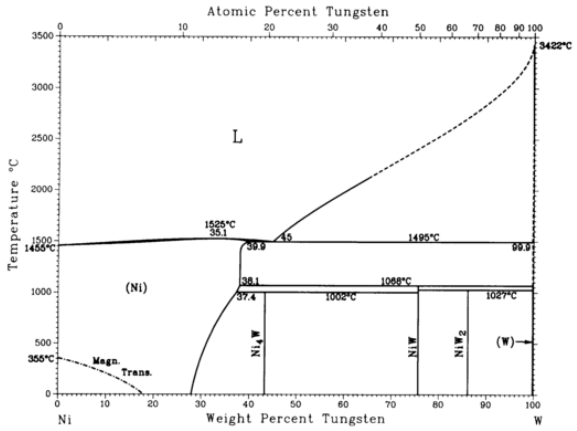

Figure 2.8. Experimental Ni-W binary phase diagram that shows a large solubility limit and several intermetallic phases [71].

Detor and Schuh were the first to investigate Ni-W thermal stability mechanisms in great detail [57,72–75]. They mostly studied electrodeposited alloys. One of their main

findings was that the equilibrium grain size monotonically decreases with W concentration [57]. Figure 2.9 shows the grain size trend of nanocrystalline Ni-W and also compares the grain size trend to nanocrystalline Ni-P alloys. The difference between the two material systems is that the grain size of Ni-P sharply decreases with solute additions. Ni-P and Ni-W have grain sizes below 20 nm with ~2 at.% P and ~20 at.% W, respectively. The gradual decrease of Ni-W grain size is caused by a weaker segregation tendency. The segregation tendency of Ni-W has been experimentally measured as 1 kJ/mol [57] and computationally quantified as 9 kJ/mol [34]. In comparison, the segregation tendencies of Ni-P [76], Pd-Zr [37], and Y-Fe [77] were measured to be 55 kJ/mol, 31 kJ/mol, and 55 kJ/mol, respectively. Pd-Zr and Y-Fe are considered "classic" thermodynamically stabilized nanocrystalline materials and are a good basis for comparison.

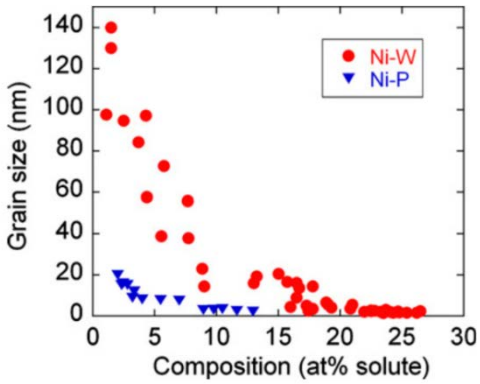

Figure 2.9. Grain size - solute concentration relationship of Ni-W (red circles) and Ni-P (blue circles) [74]. The relatively gradual decrease of Ni-W grain size is attributed to a lower segregation tendency.

Quantifying the grain boundary energy experimentally is difficult and success is more appropriately considered as simply the detection of W-segregation. The strongest evidence of W-segregation in the literature has been through the use of atom probe tomography [73,75,78]. Detor and Schuh determined that grain boundaries were enriched

with an excess of 5-10 at.% W in as-deposited 10.7 at.% W, 14.5 at.% W, and 17.5 at.% W alloys [73]. Furthermore, they annealed 13 at.% W and 21 at.% W alloys at 600 °C and quantified W enrichments of 6.6 at.% W and 6 at.% W, respectively [75]. Interestingly, they did not detect differences in grain boundary enrichment between the different alloy compositions, nor between as-deposited and heat treated alloys.

Chemical ordering has also been discussed as a potential stability mechanism. Detor and Schuh identified short range and long range ordering in a 21 at.% W annealed at 750 °C [72], and Choi *et al.* identified Ni_4W in their nanocrystalline heat treated 18 at.% W alloys [78]. Choi also argued that reduced diffusivity is a stability mechanism for Ni-W. They argued that heavy W atoms dissolved in the Ni(W) lattice increases the activation barrier because more strain is introduced into the lattice. Lastly, assuming that W does in fact segregate to the grain boundaries, it remains unknown if grain growth is limited due to reduced grain boundary energy or solute drag. Again, heavy W likely increases the solute drag force and limits grain boundary velocity.

Aware of the many potential stability mechanisms, and to best estimate which mechanisms are slowing grain growth in Ni-W, Detor and Schuh derived microstructure evolution maps to predict when an initial average size will double [74]. One figure from their original work has been modified into three progressive maps to best compare the contribution from each stability mechanism. The maps are shown in Figure 2.10. Figure 2.10a shows the simple case where the line represents the temperature at which a starting grain size doubles for a starting grain boundary energy (γ_0) and starting activation energy for grain boundary diffusion in lieu of solute drag (Q_m). Figure 2.10b represents the onset

conditions if γ_0 is reduced by 60% (*e.g.* $0.4\gamma_0$). Here the onset temperature is not heavily influenced by a reduction in grain boundary energy, which contradicts the thermodynamic mechanism. Lastly, Figure 2.10c shows the onset temperature if Q_m is increased by 50% (*e.g.* $1.5Q_m$) in addition to $0.4\gamma_0$. Here the onset temperature is greatly reduced and the grain size is significantly more stable. Overall, a decrease in grain boundary energy may not be sufficient to stop grain growth, but when combined with high solute drag effects, the microstructural stability can be greatly enhanced.

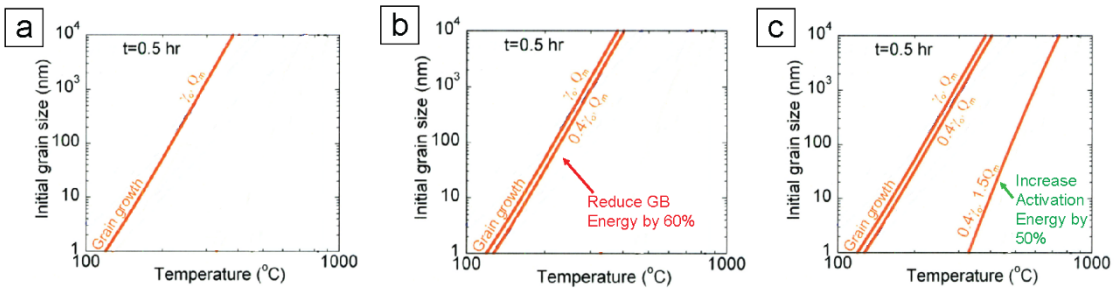

Figure 2.10. Microstructure evolution maps of Ni-W showing the onset of grain growth for solute segregation and kinetic thermal stability mechanisms. All parts are modified from Ref [148]. It is revealed here that a decrease in grain boundary energy is not as significant as an increase in activation energy.

Chapter 3 Statement of Purpose

Nanocrystalline materials have beneficial properties, but it remains unclear which thermal stability mechanisms are the most promising to limit grain growth. Many studies in the literature have computationally investigated thermal stability, but few advanced characterization studies that evaluate the physical nature of nanoscale grain growth have been successfully implemented. Furthermore, the influence of impurities on phase stability and thermal stability mechanisms has not been extensively explored. Therefore, the purpose of this thesis is to apply aberration-corrected scanning electron microscopy to study the thermodynamics and kinetics of Ni-W, and to investigate the physical nature of nanocrystalline grain growth in pure and contaminated alloys. There are three primary objectives in this work: (1) explore potential thermal stability mechanisms of pure and contaminated nanocrystalline Ni-W, (2) re-evaluate Ni-W phase stability and link findings to grain growth behavior, and (3) compare electrodeposited, DC magnetron sputtered, and mechanically alloyed samples to assess the microstructural evolution of each fabrication method. Overall, this thesis will expand the field's knowledge on the grain growth behavior of nanocrystalline Ni-W and guide future research on other nanocrystalline material systems.

Chapter 4 Experimental Procedure

4.1 Nanocrystalline Ni-W Sample Fabrication and Heat Treating

4.1.1 Electrodeposition

Electrodeposited films were produced by Denise Yin at Lehigh University or by our collaborators Yuanyao Zhang and Jian Luo at the University of California, San Diego (UCSD). Both deposition configurations used the aqueous bath composition listed in Table 4.1 [79]. Trisodium citrate and ammonium chloride were used as complexing agents, and sodium bromide was used to improve the conductivity. The alloys produced at Lehigh and UCSD are summarized in Table 4.2. To control the W concentration, a continuous forward (cathodic) current density of 0.2 A/cm^2 was alternated with different magnitudes of reverse currents between 20 ms and 3 ms durations, respectively [57]. At Lehigh and UCSD, the bath temperatures were maintained at 75 °C, the baths were stirred during deposition to produce uniform films, and platinum mesh was used as the anode. At Lehigh, the anode was placed 15 mm from the cathode, the total deposition time was varied between 1 hr and 2.5 hr to produce films roughly 30 μm thick, and the bath pH was held constant at 8.0. The Lehigh films were plated onto 99.95% Cu (1 cm × 1 cm × 0.5 mm) that were plasma cleaned for five minutes, immersed in 10 vol.% HCl for 10 s, and rinsed with DI water to create a clean surface prior to deposition. The Ni-W films were separated from the Cu substrate after deposition by soaking in solutions containing CrO_3 (250 g/L) and H_2SO_4 (15 cc/L). At UCSD, the anode was placed 10 mm from the cathode, films were plated onto

either 99.99% pure Ni or Cu substrates (5 cm × 1 cm × 1 mm), and the deposition time was held at 30 min to produce 10 µm thick films.

Table 4.1. Chemical composition of plating bath

Chemical	**Amount**
Nickel sulfate, $NiSO_4 \cdot 6H_2O$	0.06 mol/L
Trisodium citrate, $Na_3C_6H_5O_7 \cdot 2H_2O$	UCSD: 0.3 mol/L Lehigh: 0.5 mol/L
Sodium tungstate, $Na_2WO_4 \cdot 2H_2O$	0.14 mol/L
Ammonium chloride, NH_4Cl	0.5 mol/L
Sodium bromide, NaBr	0.15 mol/L

Table 4.2. Differences in electrodeposition plating conditions between Lehigh University and UCSD

	Lehigh		**UCSD**	
Current Density	3 at.% W:	0.2 A/cm^2 (20 ms), -0.2 A/cm^2 (3 ms)	23 at.% W:	0.2 A/cm^2 (20 ms), -0.10 A/cm^2 (3 ms)
	5 at.% W:	0.2 A/cm^2 (20 ms), -0.25 A/cm^2 (3 ms)		
	12 at.% W:	0.2 A/cm^2 (20 ms), -0.075 A/cm^2 (3 ms)		
	15 at.% W:	0.2 A/cm^2 (20 ms), -0.0175 A/cm^2 (3 ms)		
	17 at.% W:	0.2 A/cm^2 (20 ms), -0.01 A/cm^2 (3 ms)		
	21 at.% W:	0.2 A/cm^2 DC mode		
Film Thickness	~ 30 µm		~10 µm	
Bath pH	~8.0		Unknown	
Stirring Rate	300 RPM		Unknown	
Anode-Cathode Distance	15 mm		10 mm	

4.1.2 DC Magnetron Sputtering

Sputtered alloys were produced with an AJA International ATC 2200 DC Magnetron Sputtering System via a co-deposition process using Ni-7 at.%W (99.9%

purity) and W (99.95% purity) targets purchased from Plasmaterials, Inc. The films were deposited onto 5x7 mm diced Ultraflat <100> Si wafers with a 200 nm thermally oxidized SiO_2 diffusion barrier. The global sputtering conditions can be found in Table 4.3, and sputtering conditions tailored for specific alloy compositions can be found in Table 4.4. Furthermore, the gun power, gun pulse rate, substrate bias, and Ar working pressure were systematically controlled to determine the influence of the global sputtering conditions on microstructure and grain growth. The possible parameter combinations in this experiment are summarized in Table 4.5. The pulse rate was adjusted with a Sparc-le 20 accessory.

Table 4.3. DC magnetron global sputtering conditions

Parameter	**Value**
Base Pressure	$< 5x10^{-7}$ Torr
Ar Working Pressure	5 mTorr
Process Temperature	298 K
Stage Rotation	20 rpm
Target Diameter	2”
Target Thickness	0.25”
Substrate Bias	None

Table 4.4. DC magnetron alloy preparation conditions

	7 at.% W	**21 at.% W**
NiW Gun Power	300 W	235 W
W Gun Power	0 W	65 W
Deposition Rate	13.5 nm/min	18.0 nm/min
Film Thickness	850 nm	1150 nm

Table 4.5. Possible array of 7 at.% W sputtering conditions

Parameter	**Value**
Power	50, 300 W
Pulse Rate	0, 20 kHz
Substrate Bias	0, -50, -100, -150 V
Ar Working Pressure	2, 5, 30 mTorr

4.1.3 Mechanical Alloying

All mechanically alloyed samples were fabricated by Kris Darling and Chad Hornbuckle at the Army Research Laboratory in Aberdeen, MD. Elemental Ni (99.8% purity) and W (99.9% purity) powders were sealed in the stainless steel vials in an Ar back-filled glove box to limit contamination. The powders were cryomilled for 4 hrs with stainless steel milling balls in a SPEX 8000M shaker mill with a 10:1 powder to ball weight ratio. Next, the powders were compacted into 3 mm diameter discs with a tungsten carbide die at a pressure of 3.5 GPa at room temperature. A more detailed description of the mechanical alloying procedures can be found elsewhere [47]. In total, four Ni-W alloys were produced: 1 at.% W, 5 at.% W, 15 at.% W, and 28 at.% W.

4.1.4 Sample Heat Treating

Alloys from each fabrication process were annealed in horizontal tube furnaces. The heating rates varied between 7 °C/min and 10 °C/min, and the samples were quenched in air after the dwell was completed. The furnace tubes were purged several times to purify the atmosphere prior to each heat annealing run. Afterwards the furnace was filled with the desired atmosphere, and were closed or continuously replenished with a gas flow rate of 1 ccm/min. All annealing atmospheres, temperatures, and times are summarized in Table 4.6.

Table 4.6. Potential annealing atmospheres and temperatures

	Atmosphere	Temperature	Time
Lehigh University	N_2 – 5% H_2 Pure N_2 N_2-1000 ppm O_2	400 °C 437 °C 700 °C 728 °C 1019 °C 1164 °C	1 Hr 4 Hr 12 Hr 24 Hr
UCSD	Ar – 5% H_2	300 °C 400 °C 700 °C	1 Hr 4 Hr
ARL	N_2 – 5% H_2	437 °C 728 °C 1019 °C 1164 °C	24 Hr

4.2 Microstructural Characterization

4.2.1 Metallography

Electrodeposited samples were metallographically prepared to facilitate electron probe microanalysis (section §4.2.2), focused ion beam microscopy (section §4.2.3), and grain size analysis (section §4.2.5). The free-standing electrodeposited films were clamped in-between two Ni plates to provide mechanical stability during grinding and polishing, and mounted in epoxy (Ultrathin resin and hardener). Ni plates were chosen to match the mechanical properties of the Ni-W alloys. The pre-cured epoxy mounts were cycled under vacuum to remove porosity in-between the Ni plates in the electrodeposited samples. Once the epoxy cured, samples were beveled to remove sharp edges on the mounts by hand, and ground and polished using a Magner Scientific Sapphire 550 automatic polisher with diamond slurries. The final polishing step used a Buehler Vibromet I vibratory polisher with a 0.05 µm diamond slurry.

4.2.2 Electron Probe Microanalysis

Wavelength dispersive spectroscopy (WDS) analysis was conducted with a JEOL JXA-8900 SuperProbe to confirm the compositions of all electrodeposited and sputtered alloys. The instrument was equipped with a silicon drift detector, three WDS crystal spectrometers, and Probe for EPMA software. The cross sections in the polished electrodeposited samples and the top surfaces of the sputtered alloys were analyzed. The sputtered films were too thin to metallographically prepare, but the top surface was sufficiently flat. The WDS analysis was calibrated with a small section of an expired Ni-7 at.% W sputtering target that was also metallographically prepared. The alloy standard produced better results than pure metallic standards. For the sputtered alloys, the microprobe acquisition conditions were 12 kV accelerating voltage, 10 μm spot size, and 20 nA probe current. A low accelerating voltage was used to minimize the X-ray generation volume to limit X-ray signal from the Si substrate. An accelerating voltage of 15 kV was used for the electrodeposited samples. At least 10 spots were analyzed for each specimen to determine statistically reliable compositions.

4.2.3 Focused Ion Beam Microscopy

The focused ion beam (FIB) was used to create thin foils for transmission electron microscopy (TEM). TEM specimens were fabricated using the in-situ liftout method in a FEI Scios or a FEI DB-235 instrument [80]. Most of the milling was conducted with a 30 kV Ga beam, but a 5 kV beam was used to polish the foil after 30 kV thinning [81]. In addition, the TEM specimens were thinned to a wedge shape to create local regions that were below 20 nm in thickness [81]. Lastly, the samples were final polished using a Model

1040 Fischione NanoMill operated at 900 eV [82]. A detailed procedure of TEM sample preparation and in-situ thickness determination can be found in Appendix A and Appendix B, respectively. The FIB was also used to etch polished surfaces of electrodeposited samples for grain size quantification [83,84]. The images were etched using a 30 kV ion beam and 1 nA, then imaged with 50 pA.

4.2.4 Transmission Electron Microscopy

Transmission electron microscopy was conducted using a JEOL JEM-2000FX instrument. All experiments were conducted with a high tension voltage of 200 kV and a lanthanum hexaboride (LaB_6) thermionic gun. Bright field (TEM-BF) images were recorded to observe differences in grain size and phase distributions. Selected area diffraction (SAD) patterns were recorded to identify the phases present in each sample and to determine crystal lattice parameters. Nanocrystalline NiOx was used as a diffraction standard to calibrate the camera length. The DiffTools software plugin written by David Mitchell was used to analyze the diffraction patterns [85].

4.2.5 Scanning Transmission Electron Microscopy

Scanning transmission electron microscopy (STEM) was conducted with a JEOL-ARM200CF instrument. The microscope is equipped with a cold field emission gun and the latest generation CEOS CESCOR spherical aberration corrector. Typical operating conditions to perform high-angle annular dark field (HAADF) imaging, annular bright field (ABF) imaging, and X-ray energy dispersive spectroscopy (EDS) are listed in Table 4.7. EDS analysis was performed using a JEOL 100 mm^2 X-ray detector. A SPI plasma cleaner was used to remove organic molecules from the sample surface prior to inserting into the

microscope chamber. Furthermore, a beam shower was used to prevent carbon build-up during imaging or EDS analysis.

Table 4.7. STEM operating conditions for HAADF imaging, BF imaging, and EDS.

	HAADF	**ABF**	**EDS**
Accelerating Voltage	200 kV	200 kV	200 kV
Probe Current	78.5 pA	44.3 pA	303 pA
Condenser Aperture Size	40 µm	30 µm	40 µm
Camera Length	8 cm	8 cm	8 cm

4.3 Grain Growth Measurements

Two methods were used to determine average grain size. Average grain sizes larger than 100 nm were quantified with ion-channeling contrast (iCC) imaging. In this case, images were recorded on polished cross-sections and outlines were drawn on the grain boundaries to isolate individual grains for analysis. A detailed discussion and procedure for iCC imaging is outlined in Appendix C. Average grain sizes smaller than 100 nm were quantified with TEM-DF imaging. ImageJ was used to fill in grain areas highlighted with TEM-DF imaging and extract the grain area [86]. Next, the grain areas were converted into equivalent spherical diameters. Both grain size determination methods generated grain size distributions, and error bars were calculated using the student t-test with a 95% certainty.

4.4 Computational Modeling

DIffusion **C**ontrolled phase **TRA**nsformations (DICTRA) was used to simulate Ni and W interdiffusivity ($\widetilde{D}$) through the Ni(W) lattice at different temperatures and W-concentrations. The alloy compositions ranged from pure Ni to 15 at.% W in increments of 0.1 at.% W, and the temperatures were chosen to match annealing experiments of the

electrodeposited and mechanically alloyed samples. The TCNI7 (thermodynamic) and MOBNI3 (kinetic) databases that are specifically designed for Ni-based alloys were used to produce the best results. All of the DICTRA calculations were performed by Dan Bechetti.

Density functional theory (DFT) was used to validate Ni-W and Ni-W-C phase stability. Free energy models for the Ni-rich Ni(C,W) solid solution and the ternary Ni_6W_6C and Ni_2W_4C crystal structures were calculated, which included phonon and vibrational entropies. Using these energies, binary and ternary phase diagrams were calculated similarly to the **CAL**culated **PHA**se **D**iagrams (CALPHAD) approach. All of the DFT work was completed by Dr. Mike Widom and his graduate students Qin Gao and Sanxi Yao at Carnegie Mellon University.

Chapter 5 Ni-W Thermal Stability Mechanisms

This chapter summarizes the grain growth behavior of electrodeposited Ni-W alloys and highlights several potential thermal stability mechanisms. Two sets of electrodeposited alloys will be discussed: alloys that have negligible oxygen impurities and alloys that are heavily contaminated with oxygen impurities. The investigated thermal stability mechanisms include W-segregation, Ni_4W chemical ordering, reduced atomic diffusivity, and nanoscale oxide particle pinning. At the conclusion of this chapter, it will be clear how the dominant thermal stability mechanisms depend on the alloys purity, and why it is important to reliably predict their stability to control the overall influence on grain growth behavior.

5.1 Electrodeposited Grain Growth Overview

5.1.1 Alloys with Negligible Oxygen Impurities

Six alloy compositions from the Ni-rich portion of the phase diagram were electroplated, annealed, and characterized. The specific compositions were 3, 5, 12, 15, 17, and 21 at.% W and were chosen to replicate the thermal stability studies conducted by Schuh *et al.* [57,72–75]. Figure 5.1 compares the grain size – composition relationship from the alloys of this study and Detor and Schuh [57]. Both experiments proved that the average grain size decreased with increasing W content. The large difference in grain size at the lower W concentrations is because Detor and Schuh plotted XRD grain sizes and this study plotted TEM grain sizes. The XRD grain size determination method is known to overestimate grain sizes that are above 100 nm [38].

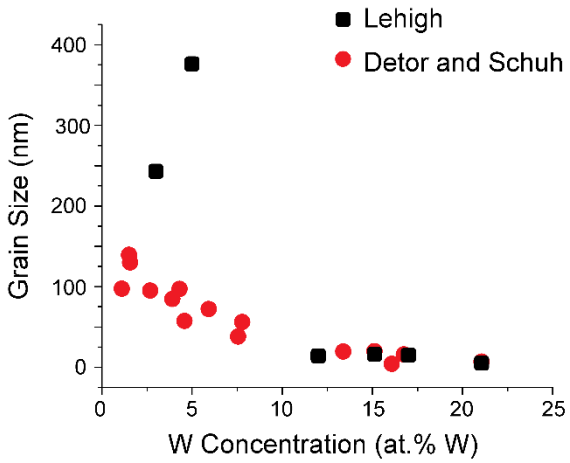

Figure 5.1. Grain size and composition relationship that shows increasing W concentrations decreases grain size. Grain sizes from this study are compared to Detor and Schuh that were fabricated with their reverse pulse plating technique [57].

Figure 5.2 summarizes the grain growth and lattice parameters trends as a function of temperature. Here it is clear that the 3 at.% W and 5 at.% W alloys were not stable above 437 °C while the higher W concentrations were stable until 728 °C. All the alloys were a single phase Ni(W), except for the 21 at.% W alloy that consisted of Ni_4W, Ni_6W_6C and pure W. Figure 5.2b shows that the lattice parameters of each alloy were initially larger in the as-deposited state, contracted after annealing at 437 °C, and then expanded after annealing at 728 °C. The lattice parameters were determined from the selected area diffraction patterns. The relatively large lattice parameters in the as-deposited state suggest that the Ni(W) solid solution was super-saturated with W. The decrease in lattice parameter after 437 °C annealing suggests that W left the solid solution. Here, the question is where did the W go? Since the microstructures were fully crystalline and secondary phases were not detected, the practicable position for the W excess is on the grain boundaries. This possibility is discussed in section §5.2. The lattice expanding after 728 °C suggests that W

dissolved back into the Ni(W) solid solution. Lattice expansion at higher temperatures is commonly observed as the solid solubility limit increases with temperature. However, it is unclear if the W is de-segregated from the grain boundaries, which may have caused the large jump in grain size between 437 °C and 728 °C, or if the lattice expanded because of different phenomena. A further discussion on the lattice contraction and expansion is found later in section §6.4.

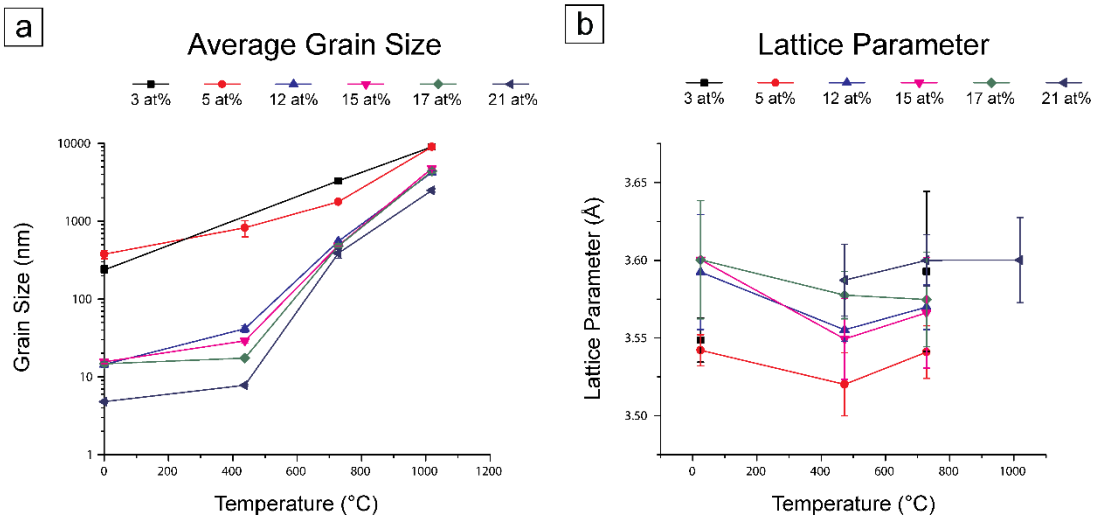

Figure 5.2. (a) Average grain size and (b) lattice parameter measurements of the electrodeposited alloys annealed for 24 hrs. Error bars represent 95% certainty.

The grain size distributions must be considered, in addition to the average grain size, because abnormal grain growth could signify differences in grain boundary behavior. Abnormal grains in this thesis are defined as at least 3x the average grain size, and the signature of an abnormal microstructure is a multi-modal grain size distribution. After analyzing the electrodeposited alloys, it was determined that the distributions for all the alloys were unimodal in the as-deposited state (*i.e.* normal), but the 12 at.% W, 15 at.% W

and 17 at.% W alloys were bi-modal at the intermediate temperatures (*i.e.* abnormal). Annealing at 1019 °C returned the alloys to unimodal distributions.

Figure 5.3 compares TEM-BF images of the 12 at.% W and 15 at.% W alloys after annealing at 437 °C. The abnormal grains can been easily seen in 12 at.% W alloy in Figure 5.3a and the higher magnification image in Figure 5.3b shows an abnormal grain that is ~10-20x larger than the smaller population. The 17 at.% W exhibited fewer abnormal grains, but one abnormal grain is shown in Figure 5.3d. Figure 5.4 compares the microstructures after annealing at 728 °C. Two iCC and corresponding grain size histograms compare the microstructures of the 5 at.% W (unimodal) and 15 at.% W (bimodal) alloys. The average grain size of the 5 at.% W alloy was ~2.6 μm, and the average grain sizes of the small and large populations of the 15 at.% W were ~310 nm and ~3 μm, respectively. Unfortunately there were not enough abnormal grains to generate a well-rounded peak in the histogram so the larger population size of 3 μm is a rough estimate. In total there were 3476 grains measured and only 30 of the grains were considered abnormal.

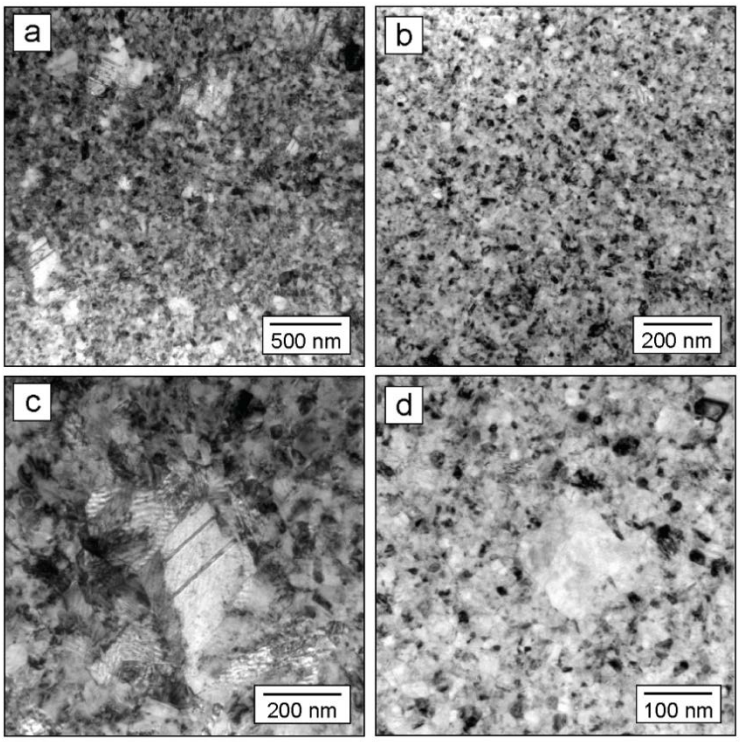

Figure 5.3. BF-TEM images of the (a,c) 12at% and (b,d) 17at% alloys at low and high magnifications, respectively, after annealing at 437 for 24 hrs..

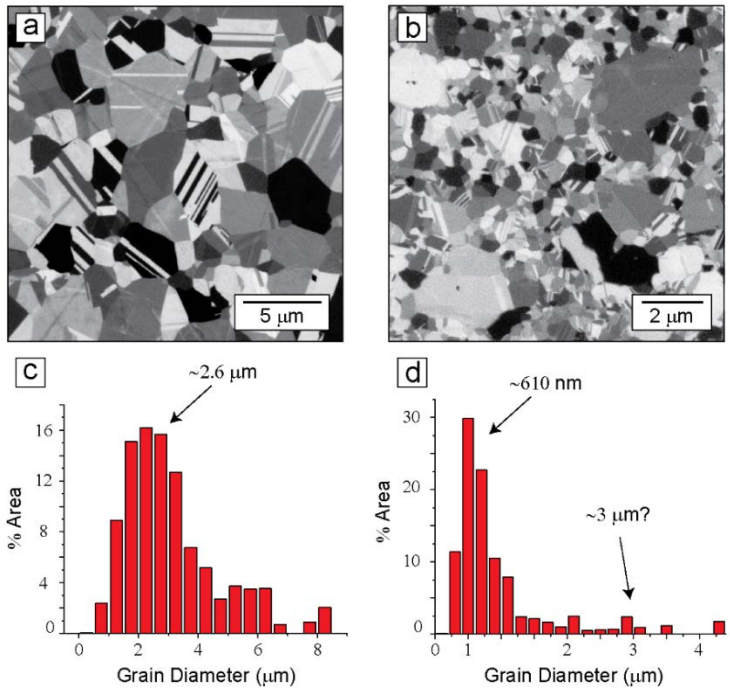

Figure 5.4. Comparison of ion channeling contrast images and grain size distributions of the (a,c) 5 at.% W and (b,d) 15 at.% W alloys annealed at 728 °C for 24 hrs, respectively.

The impurity concentrations of the electrodeposited alloys were determined to compare the purity of these alloys to those in the literature. Table 5.1 shows the carbon, oxygen, and sulfur concentrations, which were determined by hot extraction performed by Evans Analytical Group. The carbon and oxygen impurity concentrations were relatively high compared to similar alloys [50].

Table 5.1. Impurity concentrations of carbon, oxygen, and sulfur in the electrodeposited alloys determined with hot extraction analysis.

	Carbon (wt. ppm)	**Oxygen (wt. ppm)**	**Sulfur (wt. ppm)**
3 at.% W	993	695	< 10
11 at.% W	924	695	< 10
21 at.% W	710	738	17

5.1.2 Alloys with High Oxygen Impurities

These alloys were fabricated by our collaborators at UCSD. Ni-23 at.%W alloys were analyzed before and after annealing at 300 °C, 400 °C, and 700 °C for 4 hrs in a reducing Ar-5% H_2 atmosphere [87]. Another specimen was annealed at 700 °C for 1 hr to compare the growth of the particles and Ni(W) grain size at a single temperature. Overall, there were more impurity phases identified in the UCSD alloys than similar alloys produced by Lehigh. The source of the oxide particles in the UCSD alloys is unknown. Table 5.2 summarizes the identified phases, Ni(W) grain size, and oxide particle sizes, and Figure 5.5 shows TEM-BF or STEM-HAADF micrographs of each specimen.

Table 5.2. Summary of the identified phases, Ni(W) grain size, and oxide particle size in the as-deposited and annealed UCSD Ni-23at.% W alloys.

Heat Treatment	**Identified Phases**	**Ni(W) Grain Size**	**Oxide Particle Size**
As-deposited	Amorphous, Ni(W), WOx	~5 nm	Streaks
300 °C – 4 Hr	Amorphous, Ni(W), WOx	~5 nm	Streaks
400 °C – 4 Hr	Amorphous, Ni(W), WOx	20 nm ± 1 nm	~3 nm
700 °C – 1 Hr	Ni(W), Ni_4W, Ni_6W_6C, WOx	~20 nm	~3 nm
700 °C – 4 Hr	Ni(W), Ni_4W, Ni_6W_6C, WOx	25 nm ± 2 nm	4.5 nm ± 0.2 nm

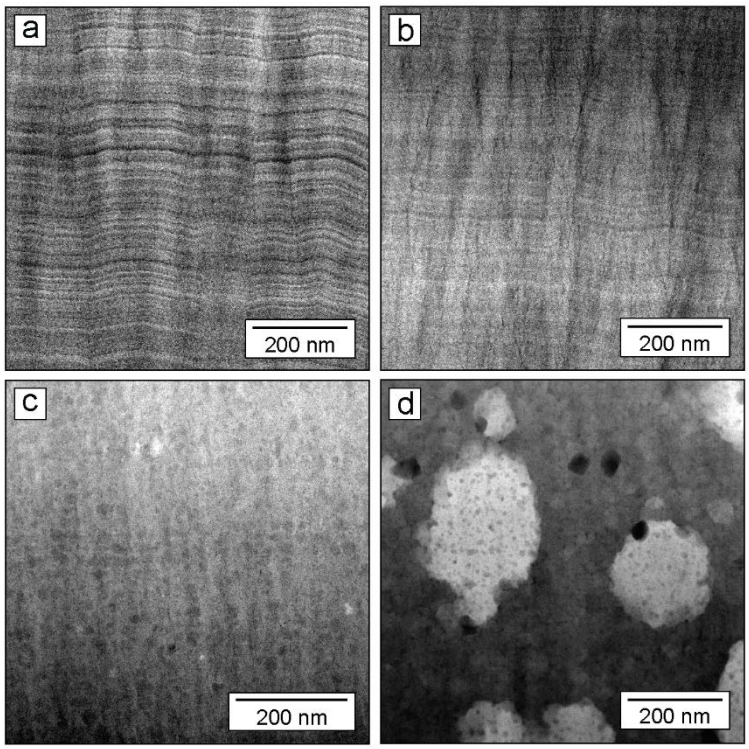

Figure 5.5. STEM-HAADF images comparing the as-deposited and annealed UCSD Ni-23at.%W alloys: (a) as-deposited, (b) 300 °C, (c) 400 °C, and (d) 700 °C [87].

The as-deposited alloy was roughly 95% amorphous and the small number of grains averaged 5 nm. Similarly, the 300 °C alloy was mostly amorphous and the grains averaged 5 nm. The as-deposited and 300 °C alloy also exhibited impurity oxide streaks that ran

vertically (perpendicular to the substrate), and other compositional differences that ran horizontally (parallel to the substrate). Figure 5.6 shows the oxide streaks and layers at higher magnifications. The vertical oxide streaks in both alloys were confirmed as oxygen-rich with STEM-EDS. Furthermore, the oxide streaks in the 300 °C exhibited a branched morphology. The oxide streaks were located in-between columnar colonies that formed during deposition. Similar observations of columnar colonies in electrodeposited Ni-W have been made in the past by Ruan and Schuh [88].

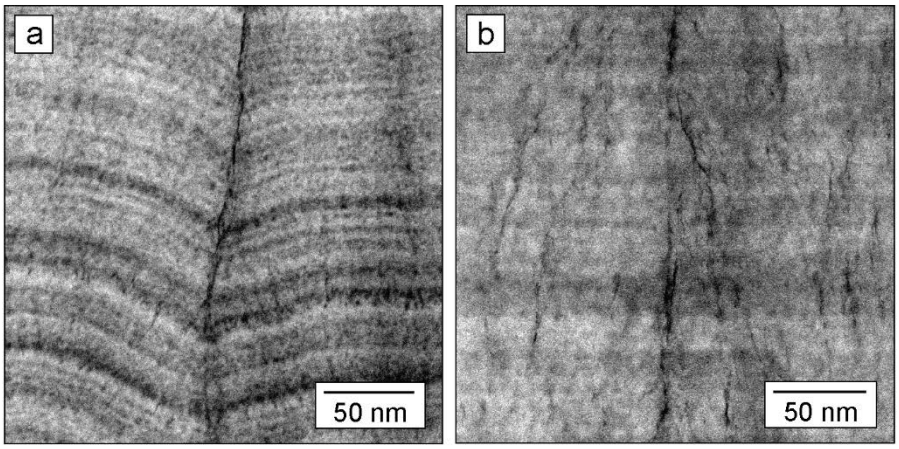

Figure 5.6. STEM-HAADF images of the oxide streaks found in the (a) as-deposited and (b) 300 °C specimens. Modified from Ref. [87].

The microstructure mostly crystallized after annealing at 400 °C. The grains coarsened to 20 ± 1 nm in diameter, and in addition, nanoscale W-rich oxides precipitated. Annealing at 700 °C fully crystallized the microstructure, precipitated Ni_6W_6C and Ni_4W phases, and coarsened the grains and oxide particles to 25 ± 2 nm and 4.5 ± 0.2 nm in diameter, respectively. Figure 5.7 shows the oxide particles that were found in the 400 °C and 700 °C alloys. The composition of the oxide particles was confirmed with STEM-EDS and the results are shown in Figure 5.8. The EDS results here were not standardized so the

exact stoichiometry is unknown, but using Ni-W-O ternary phase diagrams found in the literature, the most likely stoichiometry of the oxide particles is WO_2 [89]. The morphology of the particles between 400 °C and 700 °C were different, which may have different effects on pinning grain growth. The particles in the 400 °C alloy were more elongated along grain boundaries, whereas the 700 °C particles were spherical and located on grain boundaries, especially the triple points. The growth of the oxide particles corresponded well with the growth of the Ni(W) grains. The oxide particles coarsened from 3 nm to 4.5 nm, and the Ni(W) grains coarsened from 20 nm to 25 nm.

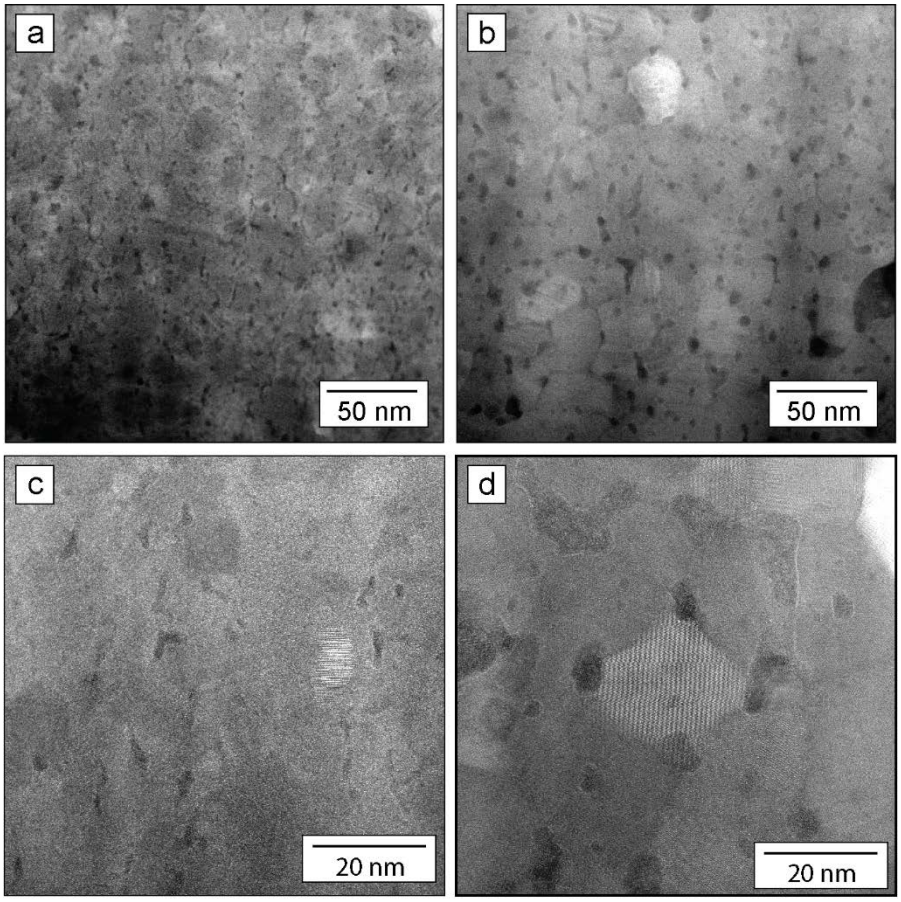

Figure 5.7. STEM-HAADF images of the oxide particles at high and low magnifications of the (a,c) 400 °C and (b,d) 700 °C alloys annealed for 4 hrs. Parts (a), (b), and (c) were modified from Ref. [95].

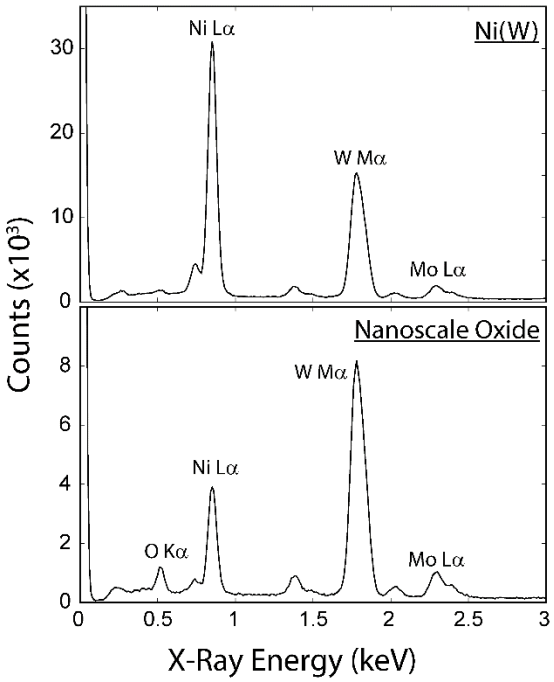

Figure 5.8. STEM-EDS spectra of the (a) Ni(W) matrix and (b) nanoscale oxide precipitates in the 700 °C - 4 hr alloy.

The oxide particles were crystalline (see section §5.4.3) and an attempt was made to determine the crystal structure. A large Ni_6W_6C that contained oxide particles was oriented to a low index direction, and since the crystal structure of the Ni_6W_6C was known, any unknown diffraction spots would belong to the oxide particles. Figure 5.9 shows a Ni_6W_6C grain that had several oxide particles, and at higher magnifications, it was clear that the oxide particles were faceted. Unfortunately, non-carbide diffraction spots were not detected and the analysis was inconclusive.

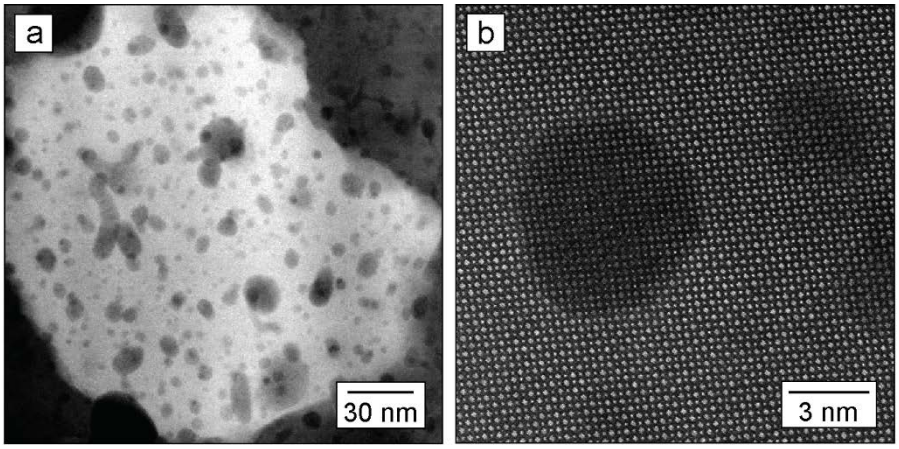

Figure 5.9. STEM-HAADF images showing (a) the nanoscale oxides in a Ni6W6C grain and (b) faceted edges of the oxide particles within a carbide that was oriented to the [110] crystal direction.

5.2 W-segregation to Ni(W) Grain Boundaries

W-segregation is the most commonly cited mechanism for Ni-W thermal stability. However, few studies have applied aberration-corrected STEM to analyze the grain boundaries on the atomic scale. This research has attempted to fill that knowledge gap. First, the tendency of W-segregation in Ni-W will be discussed, followed by experimental difficulties in detecting W-segregation with analytical STEM, and analysis of grain boundaries in the electrodeposited alloys will be summarized.

5.2.1 W-segregation Tendency in Ni-W Alloys

The segregation tendency of a solute in a crystalline matrix scales inversely with solid solubility [90]. According to the Hume-Rothery rules of solid solubility, the solute and solvent should have similar atomic radii, crystal structure, electronegativity, and valency to maximize the solubility. If these simple rules are used to evaluate the N-W system, it would be concluded that there should be a low W solubility limit in Ni and the

segregation tendency of W should be high. One rationale for the high W solubility in Ni is the magnetic contribution to the Gibb's free energy of the lattice, similar to the Fe-Ni system [91]. Thus, Ni-W exhibits a high W solubility limit despite the W atomic radius being much larger than Ni (1.93 Å vs 1.49 Å) and the crystal structure being BCC instead of FCC. Overall the solid solubility and segregation tendency of W in Ni is complicated.

Several authors have used the thermodynamic models discussed in section §2.3.1 to estimate the minimum grain boundary energy due to W-segregation. Atwater and Darling predicted the minimum grain boundary energy is 62% of pure Ni boundaries when the alloy composition is 19.9 at.% W [31]. Likewise, Detor and Schuh predicted that the grain boundary energy can be reduced to 60% after alloying with 22 at.% W [74]. These results are interesting for two reasons: (1) a minimum value of 62% indicates that the thermodynamic driving force for grain growth is not completely removed, meaning other mechanisms are possibly responsible for the high stability of Ni-W, and (2) the necessary W concentration to minimize the grain boundary energy is beyond the solid solubility limit of 12 at.% W, meaning that the necessary W concentration may not be possible in real Ni-W alloys. In comparison, Atwater and Darling the minimum grain boundary energy reaches 0 with a Zr concentration of 17.5 at.% in nanocrystalline Fe-Zr [31]. Overall, based on these calculations, Ni-W should not be classified as a thermodynamically stable alloy.

Considering that the tendency for W-segregation in Ni-W is low, and that there is a high solid solubility limit of W in Ni, the excess W that segregates to the grain boundaries may only be a few at.% more than the matrix. In contrast to other highly segregating systems, where the solid solubility limit is low, the amount of solute on the grain boundary

is significantly higher. Hentschel *et al.* have shown that in electrodeposited Ni-P, the grain interior had 1.4 at.% P, but the grain boundaries had 13.5 at.% P [92]. Further complicating W-segregation tendency is that it may be more favorable at lower bulk W concentrations [73]. Detor and Schuh hypothesized that the enthalpy of segregation decreases with increasing W bulk concentrations, and thereby reduces the driving force for segregation. Yet, this notion is contradictory to the thermodynamic theory where the smallest equilibrium grain size requires the highest amount of W. One possible explanation for the appearance of W-segregation is that W atoms accumulate and are trapped on the grain boundaries during grain growth. In this case W does not segregate because of chemical or elastic effects, but because it cannot re-dissolve into the Ni(W) solution as the grain boundary migrates. Ultimately, the true tendency for W-segregation and the mechanism at which is occurs are still unknown.

5.2.2 Detection Limit with Analytical STEM

The concentration of W on the grain boundaries may not be much higher than the concentration of W in the lattice. Thus, experimentally confirming W-segregation with statistical confidence is challenging. The minimum detection limit using analytical STEM was reviewed by Keast and Williams [93]:

$$\Gamma_{min} = \rho \kappa_{sm} \frac{A_m}{A_s} \frac{V}{A} \frac{3\sqrt{2I_s^b}}{I_m} \tag{13}$$

where the minimum detection limit (Γ_{min}) depends on the matrix atomic density (ρ), the Cliff-Lorimer factor (κ_{sm}) of the solute (s) and matrix (m), the ratio of the electron beam interaction volume to the area of the grain boundary within the interaction volume (V/A),

the minimum detectability limit of an X-ray peak ($3\sqrt{2I_s^b}$) where I_s^b is the intensity of the background under the solute X-ray peak, and the intensity of the solute peak for the matrix (I_m). The detection limit is defined as the number of atoms/nm^2 and can be converted into at.% if it is assumed that the average planar density of grain boundary is $\rho^{2/3}$. Most variables in Equation (13 are constants except for the minimum detectability of the solute peak and V/A.

The detection limit described by Equation 13 is the smallest amount of excess W concentration that can be detected with statistical confidence. This estimation is also higher than what is generally defined as the minimum detection limit of a trace element in the matrix. The complex geometry of a grain boundary and beam broadening worsen the detection limit of grain boundary segregation. The minimum detectability of the solute can be improved by collecting more X-ray counts by raising the probe current or increasing the acquisition time. However, the probe current may not be advisable depending on the experimental conditions, and longer acquisition times are toubling because of sample drift, potential beam damage, and hydrocarbon contamination that builds on the sample surface. The other route to maximize detectability is to increase V/A. If EDS line scans are used, it is assumed that the interaction volume of the beam transmitting through the TEM specimen is shaped as a truncated cone:

$$\frac{V}{A} = \frac{\pi}{4}\left(\frac{d^2 + bd + b^2/3}{d + b/2}\right) \tag{14}$$

where d is the electron probe diameter and b is the beam broadening [93]. Using single scattering theory, the beam broadening is defined as:

$$b = 625\frac{Z}{E}\left(\frac{\rho}{A}\right)^{1/2} t^{3/2} \quad (15)$$

where Z is the average atomic number of the matrix, E is the electron beam energy, ρ is the density of the matrix, A is the atomic weight of the matrix, and t is the TEM sample thickness [94]. In this case, the sample thickness is a highly sensitive variable because it greatly effects V/A. For instance, the minimum detectability limit of a 23 at.% W alloy was 0.3 atoms/nm^2 or 1.6 at.% W if the sample thickness was 50 nm, but 0.85 atoms/nm^2 or 4.3 at.% W if the sample thickness was 100 nm [95]. The background intensity for these calculations was ~9000 counts.

Another method to analyze the grain boundaries is to use a raster scan method where V/A is then equal to the width of the rectangular raster box [96]. The raster technique has a poorer minimum detectability limit [93], but it is advantageous over a line scan because it has a larger analytical volume that negates sources of error from beam broadening, sample drift, and geometrical requirements that need the boundary in the edge-on condition. Overall, these calculations have confirmed that W-segregation can be detected with analytical STEM, but it is recommended that thin samples are analyzed for long acquisitions to improve the minimum detectability. More specifically, the advantages of the large analytical volume are (1) beam broadening is less sensitive because the added volume from the truncated cone is much less than the total analytical volume, (2) sample drift is accounted for because if the sample drifts a few nm during the acquisition, the grain boundary is still likely captured (if sample drift is not corrected periodically during a line scan, it is possible that the beam can miss the grain boundary), and (3) if the grain boundary is tilted, the total solute excess is captured (a line scan may not quantify the real excess on

the grain boundary because it cannot differentiate between the matrix and grain boundary if the boundary is not on the edge-on condition.

5.2.3 STEM Analysis of W-segregation

Several grain boundaries in as-deposited and annealed alloys were analyzed to search for W-segregation. Figure 5.10 shows atomic resolution STEM-HAADF images of grain boundaries in the 3 at.% W and 11 at.% W as-deposited alloys, and the 9 at.% W and 21 at.% W alloys that were annealed at 700 °C for 4 hrs. Each image was obtained by tilting one grain that was in contact with the boundary to a low index crystal direction. Grain boundary W-segregation was not apparent in any of the images; there was not a sharp increase of intensity on the grain boundaries compared to the other areas in the images. Grain boundaries that exhibit W-segregation should be brighter relative to the matrix on either side of the boundary when using STEM-HAADF imaging.

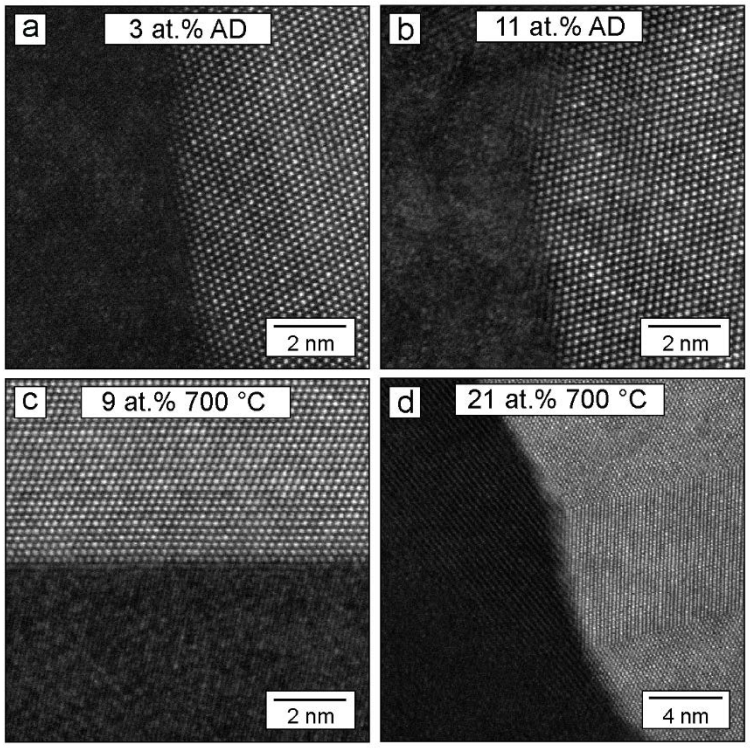

Figure 5.10. STEM-HAADF images showing no evidence of W-segregation in as-deposited (a) 3 at.% W and (b) 11 at.% W, nor annealed (700 °C) (c) 9 at.% W and (d) 21 at.% W alloys.

The raster scan approach discussed in section §5.2.2 was used to detect W-segregation [96]. Figure 5.11 shows the region that was analyzed and two spectra. Each region was 1.05 nm wide. The black line in Figure 5.11b is the average extracted spectrum between the two grain interiors, and the red line was the spectra extracted from the grain boundary. The area density of W atoms on the grain boundary and in the grain interiors were 15.1 ± 1.4 atoms/nm^2 and 11.2 ± 1.1 atoms/nm^2. Therefore, the grain boundary excess W concentration is ~3.9 atoms/nm^2. Thus, this analysis determined that W-segregation did occur on this grain boundary.

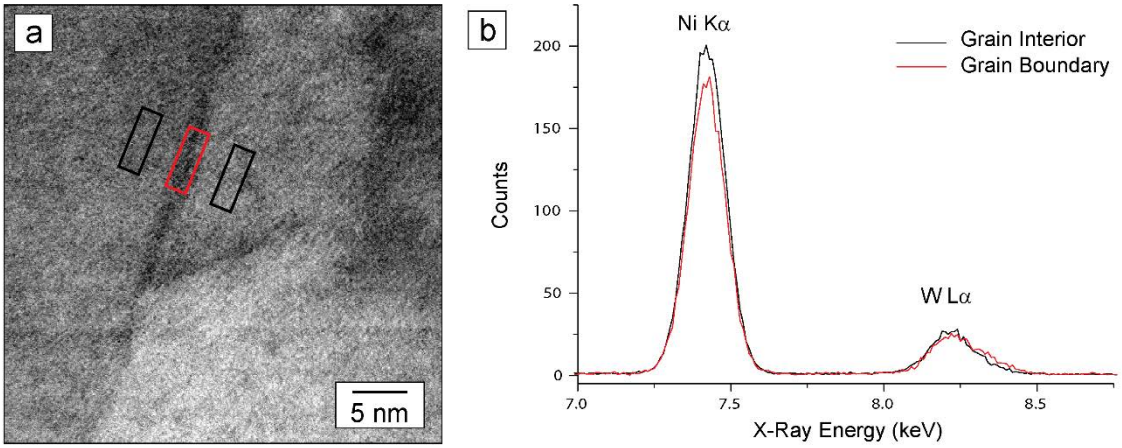

Figure 5.11. (a) STEM-BF and (b) raster scan EDS spectra of a Ni(W) grain boundary that was analyzed in the 3 at% as-deposited alloy. The red box in (a) and red line in (b) represent grain boundary, and the black boxes in (a) and black line in (b) represent the grain interiors, respectively.

The EDS analysis presented above indicated that there was a measurable W excess concentration on the grain boundary. However, the background counts under the W Lα peak used in the analysis were low and there is little statistical confidence in the measurement. If the counts from these spectra are used and assuming the sample thickness was 50 nm, the minimum detectability limit is predicted to be 11.2 atoms/nm^2. Now, since the measured excess on the grain boundary was 3.9 atoms/nm^2, it is not statistically valid to conclude there is a quantifiable excess concentration on the grain boundary. Longer acquisition times should be used to increase the total number of counts and thereby reduce the minimum detectability limit. The total acquisition time used for each region in Figure 5.11a was only 3.5 sec and produced 30 background counts under the W Lα peak, but the recommend acquisition time is at least 5 min per spectrum to produce ~9000 background counts under the W Lα peak, which was used for the minimum detectability calculations in section §5.2.2.

5.2.4 Indirect Evidence of W-segregation Based on Lattice Parameter Measurements

The lattice parameters from the alloys in the single phase Ni(W) region were analyzed more closely to determine if the lattice parameters matched what can be expected. Vegard's law relates the Ni(W) lattice parameter to W concentration [97]:

$$a_{Ni(W)} = 2\sqrt{2}[r_{Ni} + (r_W - r_{Ni}) * X_W] \quad (16)$$

where ($a_{Ni(W)}$) is the Ni(W) lattice parameter, (r_{Ni}) is the atomic radius of Ni, (r_W) is the atomic radius of W, and (X_W) is the atomic W concentration in the lattice. The radii of Ni and W were 0.1246 nm and 0.14116 nm, respectively. Table 5.3 summarizes the lattice parameter measurements of the 5 at.% W, 12 at.% W, 15 at.% W, and 17 at.% W alloys, the expected $a_{Ni(W)}$ based on the bulk composition using Equation 16, and the average grain size of each sample.

Table 5.3 Lattice parameter measurements from electron diffraction patterns of several alloys and compared to predicted values from Vegard's law.

		Measured $a_{Ni(W)}$ (Å)	**Expected $a_{Ni(W)}$ (Å)**	**Grain Size (nm)**
5 at.% W	437 °C	3.520 ± 0.020	3.542	822 ± 194
	728 °C	3.541 ± 0.017		1774 ± 52
12 at.% W	437 °C	3.555 ± 0.008	3.580	42 ± 2
	728 °C	3.570 ± 0.015		552 ± 12
15 at.% W	437 °C	3.549 ± 0.026	3.594	29 ± 2
	728 °C	3.566 ± 0.036		483 ± 9
17 at.% W	437 °C	3.578 ± 0.015	3.604	17 ± 1
	728 °C	3.574 ± 0.030		478 ± 14

Several trends were identified after the Vegard's analysis: (1) the lattice parameter increased with increasing W concentration, (2) the lattice parameter of each alloy increased after annealing at 728 °C, and (3) the expected lattice constant based on Vegard's law was consistently greater than the measured lattice parameters. The lattice increasing with W concentration is expected because more W should be dissolved in the lattice. Likewise, the increase of lattice parameter at higher temperatures was expected because the solid solubility limit scales with temperature. The interesting observation was that the expected lattice parameter of each alloy was higher than what was measured, and when coupled with the fact that secondary phases were not detected, it can be argued that W segregated to the grain boundaries.

Despite Vegard's law, there is also evidence that a reduction in grain size can expand the lattice [98,99], meaning that an underestimated Ni(W) lattice parameter does not indicate that W left the lattice and segregated to the grain boundaries. Figure 5.12 compares both phenomenon. Figure 5.12a is a lattice expansion with increasing W content in electrodeposited alloys, and Figure 5.12b shows lattice contraction and lattice expansion with increasing grain size in sputtered Ni specimens. The latter shows that Ni contracts when the grain size (measured by XRD) is increased from 17 nm to 50 nm, but expands when the grain size is increased from 50 nm to over ~62 nm [98]. X-ray diffraction usually underestimates the grain size at larger grain sizes, so it is possible that the non-monotonic relationship continues to higher grain sizes than what is displayed on Figure 5.12b [38]. Considering Ni-W alloys, it can be argued that the increase in grain sizes for the 12 at.% W, 15 at.% W, and 17 at.% W from <50 nm to ~500 nm led to the lattice expansion. If the

lattice expanded as a result of grain size, it would mean that W-segregation did not occur where the lattice is the same concentration before and after annealing at 728 °C. Although not completed in this research, a method to determine if grain size lattice expansion occurs in Ni-W alloys is to collect electron diffraction patterns and EDS spectra from individual grains to discover if W concentration truly effects the lattice parameter.

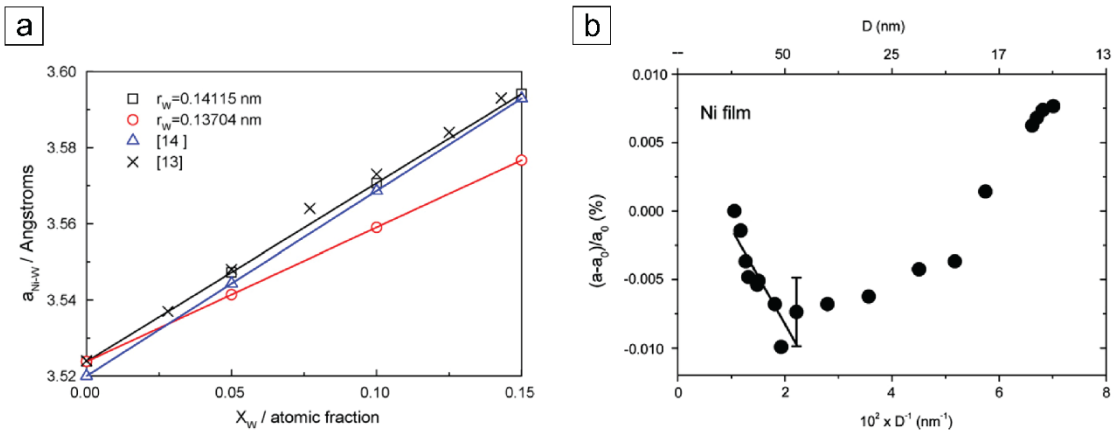

Figure 5.12. Two mechanisms for Ni(W) lattice expansion: (a) lattice expansion with increasing W concentration according to Vegard's Law [97], and (b) lattice expansion with decreasing or increasing grain size [98].

5.2.5 Searching for the Mechanism of Abnormal Grain Growth

As discussed in section §2.2, sulfur segregation instigated abnormal grain growth in nominally pure nanocrystalline Ni. Therefore, the abnormal grain growth in the 12 at.% W, 15 at.% W, and 17 at.% W alloys after annealing at 437 °C and 728 °C for 24 hrs can also potentially be attributed to solute segregation. Again, one mechanism for abnormal grain growth is a complexion transition where the grain boundary structure or chemistry changed relative amount of W segregation has changed. The possibility of a complexion transition was investigated with STEM. The red outline in Figure 5.13a shows the region that was extracted from the 15 at.% W alloy to create a TEM specimen. The FIB-BSE

image in Figure 5.13b labels two abnormal grains that are within the specimen. Overall, there were three types of interfaces captured in this TEM specimen: abnormal-abnormal, small-abnormal, and small-small.

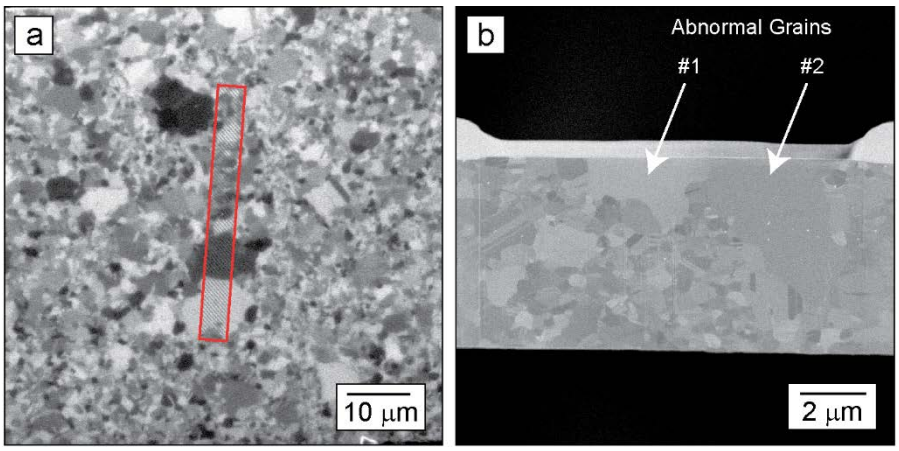

Figure 5.13. (a) iCC image showing the region that was extracted to evaluate the mechanism for abnormal grain growth in the 15 at.% W alloy annealed at 728 °C, and (b) FIB-BSE image labeling two abnormal grains.

If a complexion transition was responsible for abnormal grain growth, there should be a discernable difference between the interfaces in contact with an abnormal grain and those without an abnormal grain. The STEM-BF image in Figure 5.14a outlines the three interface types that were imaged on the atomic scale. The red outline in Figure 5.14a labels the area that was imaged with STEM-HAADF, which is shown in Figure 5.14b. Remarkably, all of the grain boundaries in the STEM-HAADF image were bright, which suggests that there may be W-segregation to all the grain boundaries. To check if W-segregation was widespread, and if complexion transitions occurred on the abnormal grain boundaries, an adjacent grain to each interface was oriented to a low index crystal direction. Figure 5.15b, Figure 5.15c, and Figure 5.15d show the abnormal-abnormal, abnormal-small, and small-small interfaces, respectively. On the atomic scale, there was no evidence

of a complexion transition at any of the grain boundaries. Each boundary appeared to be "clean" of W-segregation regardless of the type of abutting grains. STEM-EDS was not conducted on the grain boundaries to confirm if the increase of intensity in Figure 5.14b proves W-segregation. There may be a chemical difference that is not detectable with STEM imaging, so it would be a valuable experiment. Nonetheless, the cause of abnormal grain growth is still undetermined.

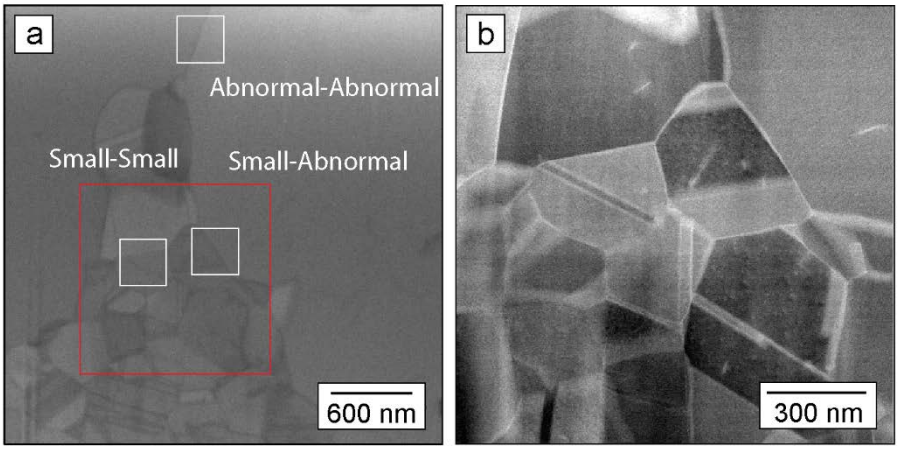

Figure 5.14. STEM images showing the abnormal-abnormal, small-abnormal, and small-small grain boundaries that were analyzed to determine the mechanism of abnormal grain growth: (a) STEM-BF image showing the specific grain boundaries that were analyzed, and (b) STEM-HAADF image showing that the grain boundaries are higher intensity suggesting there may be W-segregation.

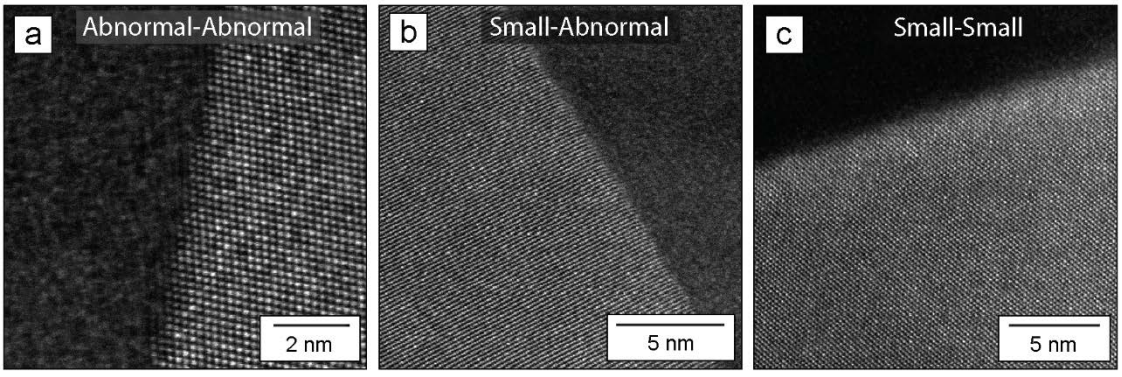

Figure 5.15. STEM-HAADF images that do not show obvious evidence of W-segregation to the (a) abnormal-abnormal, (b) small-abnormal, and (c) small-small grain boundaries.

5.3 Ni_4W Chemical Ordering

This section discusses Ni_4W short-range and long-range chemical ordering in the electrodeposited alloys. Chemical ordering has been previously observed in other studies throughout the literature, but the research in this thesis the first to image Ni-W chemical ordering on the atomic scale with STEM. Detection of Ni_4W will be summarized first and followed by a discussion of Ni_4W nucleation and growth. Next, the mechanisms in which Ni_4W ordering can slow grain growth will be presented, including a particle-like pinning mechanism and reduced diffusivity. Lastly, the Ni_4W disordering transition will be linked to grain growth behavior.

5.3.1 Definition and Detection of Ni_4W Chemical Ordering

Short-range ordering in the Ni-W system is defined as non-random arrangements of W atoms in the Ni(W) solid solution. Warren-Crowley calculations have been conducted by Detor and Engwall to elucidate the propensity of short-range ordering, especially considering the effect of grain size [74,100]. They had three main observations: (1) W atoms prefer unlike first nearest neighbors pairs (i.e. Ni-W bond), but W atoms prefer like second nearest neighbor pairs (i.e. W-W bond), (2) alloys with lower W concentrations have higher tendencies to short range order, and (3) the magnitude of short-range order decreases with decreasing grain size. A decreasing grain size introduces more grain boundaries, and if it is assumed that grain boundaries are analogous to free-surfaces where surfaces induce a disordering transition, the amount of short-range ordering will decrease [101,102].

Long-range ordering in the Ni-W system is the nucleation and growth of Ni_4W. The crystal structure of Ni_4W is classified as a $D1_a$-type ordered phase, and has been investigated with electron diffraction [74,100,103–108] and field-ion microscopy [78,109]. In addition, up to six Ni_4W variants have been observed in the disordered Ni(W) lattice [109]. Throughout this discussion, the term domain is defined as an individual Ni_4W precipitate, and the term variant is defined as a domain that has a specific crystallographic direction (*i.e.* a single Ni_4W domain can adopt different Ni_4W variants).

Ni_4W was detected in the 21 at.% W electrodeposited alloy that was annealed at 700 °C for 4 hrs. The dark Ni(W) grain seen in Figure 5.16a was oriented to the <112> crystal direction, and SAD patterns and STEM-HAADF images were recorded. Figure 5.16b is a SAD pattern and Figure 5.16c is a schematic that labels the reflections [103]. The brightest spots in the SAD pattern correspond to the Ni reflections, and the dim spots correspond to the Ni_4W superlattice reflections. In agreement with the labeled schematic, there were two variants observed in the experimental diffraction pattern. The atomic arrangement of Ni_4W is shown with a STEM-HAADF image and a simulated VESTA crystal structure in Figure 5.17 [110]. The brighter atomic columns in the STEM-HAADF image are W-rich and the darker columns are Ni-rich. Similarly, the white atoms in the VESTA structure are white and the dark grey atoms are Ni.

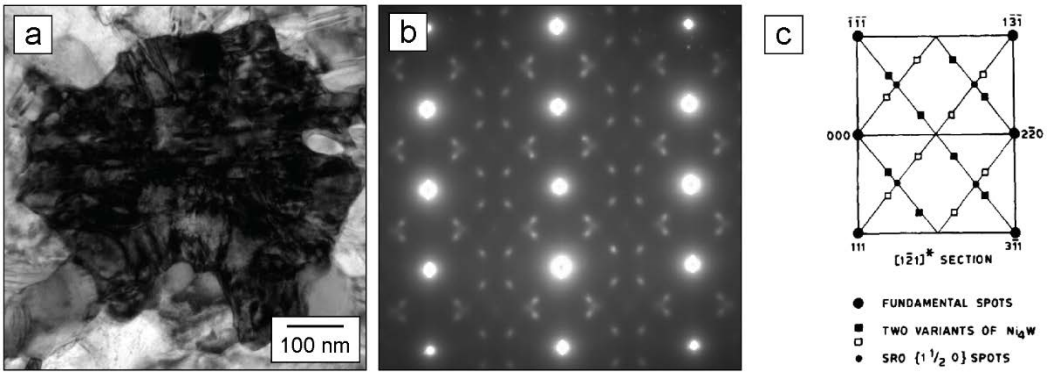

Figure 5.16. Detection of Ni_4W in the electrodeposited 21 at.% W alloy annealed at 700 °C for 4 hrs in N_2-5%H_2. (a) The TEM-BF image shows a Ni(W) grain that was oriented to the [112] crystal direction and (b) shows the resulting SADP. Part (c) labels the Ni reflections and the Ni_4W superlattice reflections [22].

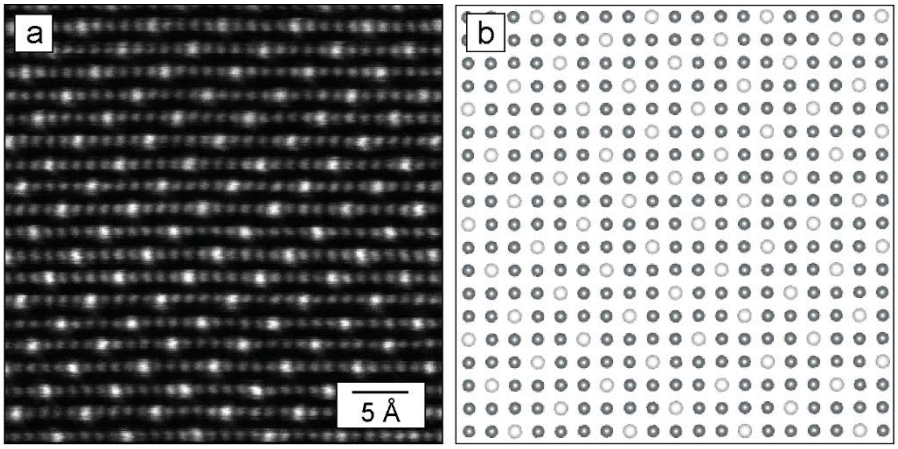

Figure 5.17. (a) Atomic resolution STEM-HAADF image showing the atomic arrangement of Ni and W atoms in the Ni4W crystal, and (b) simulated VESTA crystal structure confirming the atomic positions.

5.3.2 Ni_4W Nucleation and Growth

Ni_4W nuclei are a few nm in diameter and coherent with the parent Ni(W) lattice [111]. Furthermore, Ni_4W nucleation does not homogenously throughout the microstructure, nor within individual grains. In sputtered Ni-W alloys, it has been shown elsewhere with electron diffraction elsewhere that even within a single Ni(W) grain,

convergent beam electron diffraction (CBED) superlattice reflections are visible in some regions of a Ni(W) grain, but not in other regions of the grain [112].

Figure 5.18 shows Ni_4W nucleation that was observed in a single Ni(W) grain of the 21 at.% W alloy after annealing at 728 °C. The STEM-HAADF images in Figure 5.18a and Figure 5.18b are identical, but Figure 5.18b has three white boxes that highlight the local regions utilized to generate the fast Fourier transforms (FFT), which are seen on the right. FFT patterns reveal differences in crystallography and facilitate the identification of the different Ni_4W variants. In each FFT pattern, the Ni {112} reflections are circled in white. If present, the other spots correspond to the Ni_4W precipitates. The comparison of the three FFT patterns indicate that there are some regions where there is not Ni_4W ordering (i.e. the lack of Ni_4W reflections in the FFT), and that there are two Ni_4W variants, at least that are visible in this crystal direction. The difference in angle between the Ni_4W spots and the Ni spots confirm that there are two variant directions.

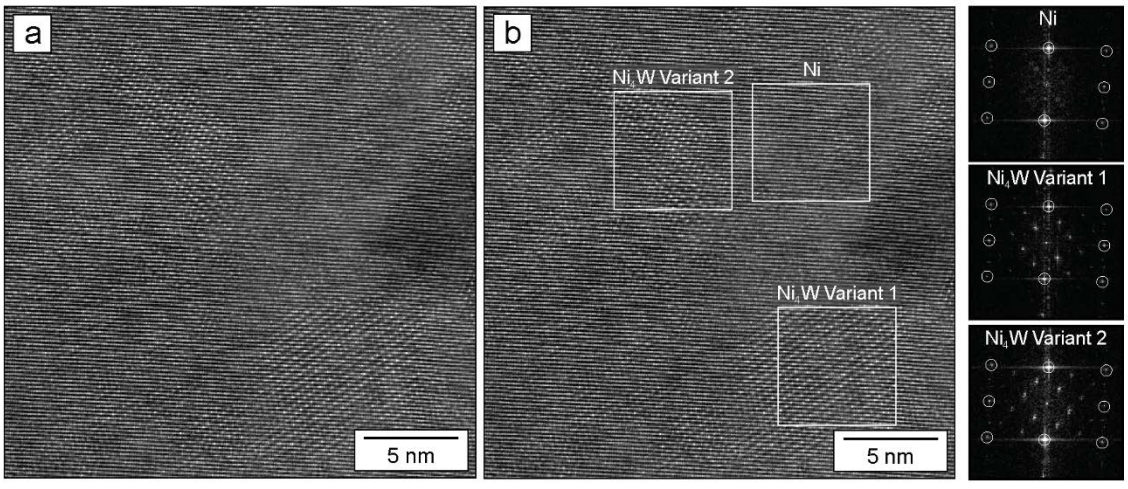

Figure 5.18. STEM-HAADF images showing two variants of Ni_4W precipitates identified in the electrodeposited 21 at.% W alloy annealed at 700 °C for 4 hrs in N_2-5%H_2. Part (b) labels the regions that were used to generate the FFTs shown to the right. The FFTs represent a region without Ni4W and the two Ni_4W variants.

The partitioning of Ni_4W within a single grain can be classified as phase separation. The thermodynamic system is an entire Ni(W) grain, and hereafter it will be assumed that the grain is a closed system, meaning W atoms do not enter the lattice nor segregate to the grain boundaries. Ni_4W is a stoichiometric compound, so phase separation will produce Ni_4W domains that have exactly 20 at.% W and create Ni(W) regions that have less than 20 at.% W. The Ni(W) regions with less than 20 at.% W will be nomenclated as $Ni(W)^{def}$ throughout this discussion. The difference in W concentration is necessary to maintain the chemical balance. The uniqueness of this phase separation process is that the entire grain will still be composed of a single, continuous parent Ni lattice.

The relative volume fractions of Ni_4W and $Ni(W)^{def}$ is important because higher amounts of Ni_4W improve the thermal stability (see section §5.3.3). To predict the relative volume fractions, tie-lines can be drawn on the phase diagram. However, the composition and volume fraction of the $Ni(W)^{def}$ depends on the solid solubility limit, which unfortunately is not confidently known (see Chapter 6). What is most important is the degree of Ni_4W ordering, as in are there only a few Ni_4W precipitates in the entire grain, or do they amount to most of the grain. Nonetheless, it is still useful to understand and predict Ni_4W partitioning to improve Ni-W thermal stability.

The large Ni(W) grain that was previously was imaged at lower magnifications to determine the Ni_4W and $Ni(W)^{def}$ volume fractions. Figure 5.19 shows a filtered STEM-HAADF image that highlights the two Ni_4W variants. The STEM-HAADF was filtered by generating a FFT of the entire image, selecting the reflections of each Ni_4W variant and the Ni(W) matrix, masking those reflections to isolate them, and then generating an

inverse-FFT image. The domains were colored in blue and orange to easily distinguish the two variants and the Ni(W) matrix. A more detailed discussion of this filtering procedure is outlined elsewhere [113]. The image processing clearly revealed the Ni_4W domains are spherical, roughly 5 nm in diameter, and amount to roughly half of the microstructure within the grain.

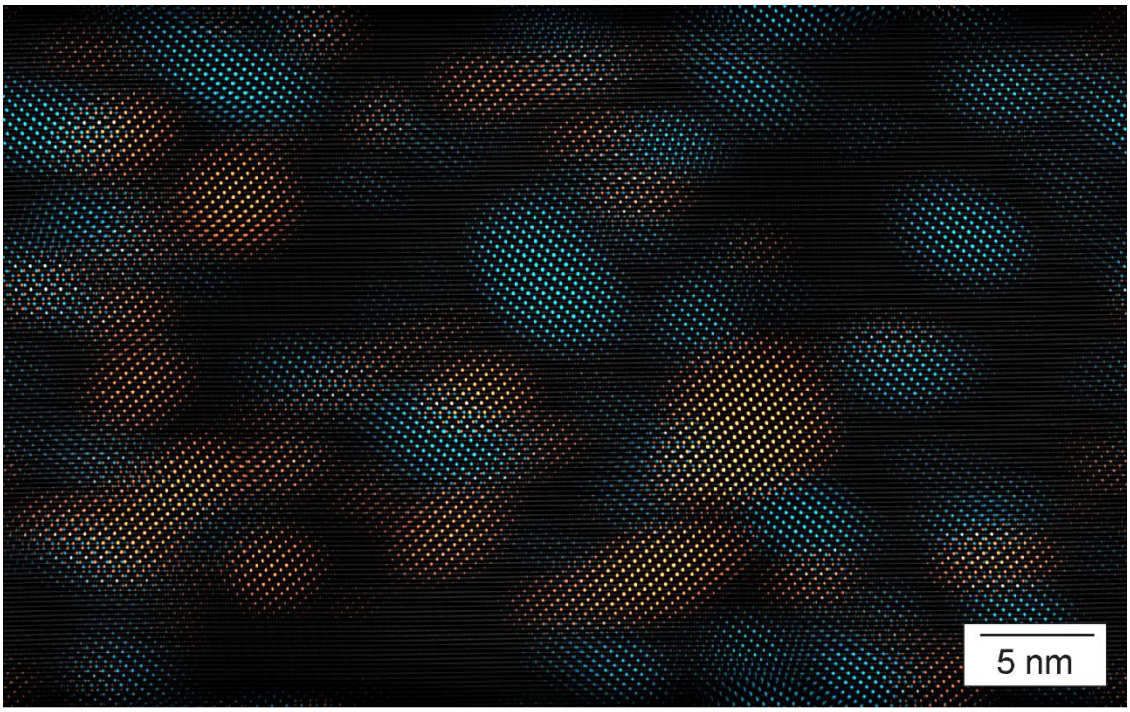

Figure 5.19. A filtered STEM-HAADF image showing the size and distribution of Ni_4W domains. Each variant is colored in blue or orange.

5.3.3 Particle-like Ni_4W Grain Boundary Pinning

Chemical ordering limits grain growth by reducing grain boundary mobility, and therefore the maximum stability is achieved when the Ni_4W domains are in close proximity to the grain boundaries. Several studies have shown that coherent precipitates that are attached to grain boundaries greatly impede grain boundary motion in a Zener-like fashion

[114–116]. Furthermore, grain boundaries with lower misorientations are more effectively pinned by coherent particles [114]. In some cases, the pinning force was so strong that instead of the grain boundary moving, the grain rotated to lower the free energy of the system to reduce the misorientation of the grain boundary [114].

The large grain discussed in sections section §5.3.1 and section §5.3.2 was analyzed again, but this time images were taken near the grain boundaries. Figure 5.20 compares two cases that were commonly observed. First, Figure 5.20a shows three grain boundaries that do not have large Ni_4W domains in close proximity. In this scenario, it is not expected that the grain boundary is pinned by the particles. In contrast, Figure 5.20b shows a large Ni_4W domain on a grain boundary. Here, the entire boundary is likely pinned because the grain boundary cannot easily migrate in either direction. If the grain boundary was not effectively pinned by the particle, the coherent Ni_4W domain will likely have to disorder, although this would raise the free energy of the system, or reorient itself with respect to the new grain [116]. More grain boundaries need to be characterized to understand the overall probability that Ni_4W domains are on the grain boundaries, and especially comparing the Ni_4W domain distribution after grain growth. Nevertheless, Ni_4W particle-like pinning is another strong mechanism to limit nanocrystalline grain growth.

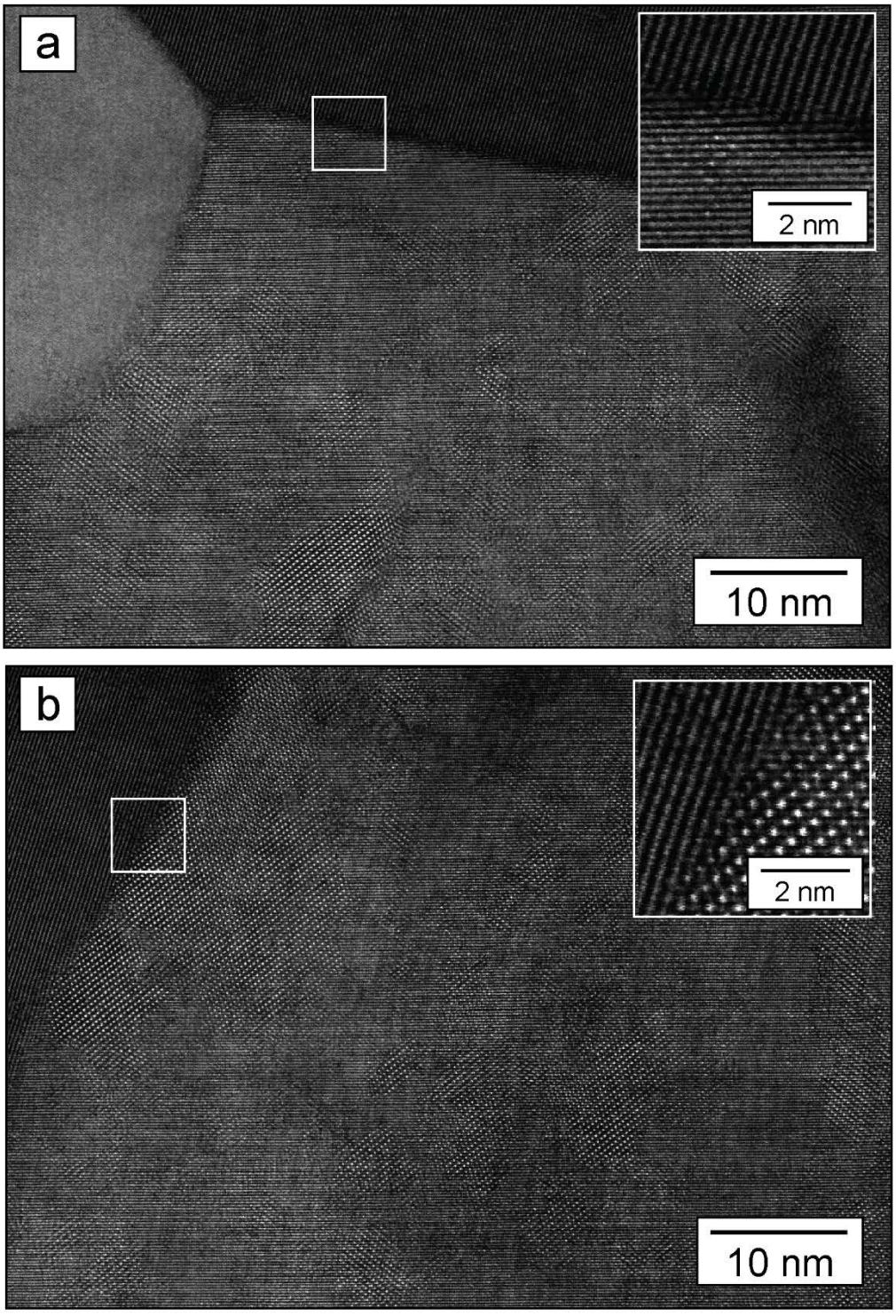

Figure 5.20. STEM-HAADF images showing the distribution of Ni_4W domains near Ni(W) grain boundaries. The image in part (a) shows a grain boundary without Ni_4W, but part (b) shows a large Ni_4W domain on the grain boundary. The white outlines show the areas of the enlarged insets.

5.3.4 Ni_4W Disordering Transition

The previous sections have described long-range chemical ordering as an effective thermal stability mechanism. However, the Ni-W phase diagram shows that Ni_4W undergoes a disordering transition ~970 °C. If Ni_4W disorders, its mechanistic benefits are lost and grain growth should accelerate. The potential of Ni_4W disordering induced grain growth was investigated by annealing the 21 at.% W alloy at 1019 °C for 24 hrs. Figure 5.21 compares microstructures before and after the disordering transition. Figure 5.21a shows a large Ni_4W domain that was stable after 728 °C. This domain is larger than those in section § §5.3.3 because the annealing time was 24 hrs instead of 4 hrs. Furthermore, Figure 5.21b shows a disordered Ni(W) lattice that was stable above 1019 °C. Both images were taken in the <112> crystal direction, and the insets show the FFT where the Ni reflections are circled in white. Clearly, the long-range order was lost after annealing above 1019 °C, but there is still evidence of short-range order from the diffuse spots near the center of the FFT pattern.

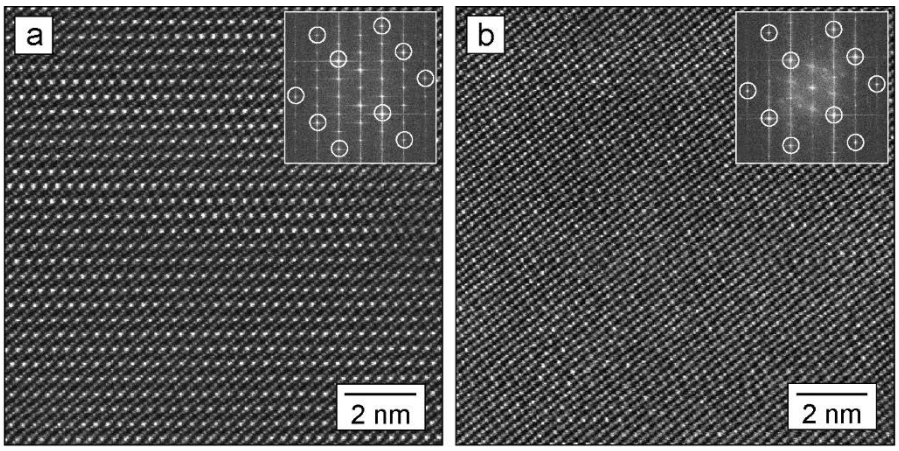

Figure 5.21. STEM-HAADF images showing the Ni_4W disordering transition in the 21at% electrodeposited alloy annealed at (a) 728 °C and (b) 1019 °C for 24 hrs in N_2-5%H_2. The insets are FFTs taken from each image and the white circles highlight the Ni [112] reflections.

The average grain size of the 21 at.% W alloy before and after the disordering transition was 386 ± 52 nm and 2481 ± 120 nm, respectively. This grain size difference is significant, but considering that the temperature range was so large, it is unclear if Ni_4W disordering was responsible for the increased grain growth. Another explanation is that diffusivity was much higher at 1019 °C, considering that diffusivity exponentially depends on temperature, caused the grain growth. Diffusivity and its relation to grain growth will be discussed in section § §5.4. One experiment than can elucidate the influence of Ni_4W disordering is to determine the precise disordering temperature and then anneal samples ~10 °C lower and ~10 °C higher than the transition temperature. Now, if there is a large jump in grain growth between ± 20 °C, it will be clear that the disordering is very detrimental to nanocrystalline grain growth. Otherwise, if the grains narrowly grow, the enhanced diffusivity is more likely since the small increase in temperature will not produce dramatically different grain sizes. Future detailed experiments are proposed in Chapter 9.

5.4 Reduced Atomic Diffusivity

The fundamental grain growth equations that were defined in section §2.2 indicate that grain growth scales linearly with diffusivity. Thus, a reduction in diffusivity should reduce the grain growth rate. Reduced diffusivity can be accomplished in the Ni-W system by alloying with higher concentrations of W. As more W is added to the system, the Ni and W interdiffusivity ($\widetilde{D}$) should decrease because of an increased diffusion activation energy, likely from high atomic size mismatch. If we assume that Ni and W interdiffusivity in the Ni(W) lattice is proportional to the interdiffusivity on grain boundary, it is possible to model the influence of W-content on the grain growth rate in the single phase Ni(W) region

of the phase diagram. In fact, it is widely accepted that the activation energy for grain boundary diffusion in Ni is half of the activation energy of lattice diffusion in Ni [117]. **DI**ffusion **C**ontrolled phase **TRA**nsformations (DICTRA) was used to simulate $\widetilde{D}$ through the disordered FCC lattice as a function of temperature and W-content [118]. The results are shown in Table 5.4. Alloy compositions ranging from pure Ni to 15 at.% W with increments of 0.1 at.% W were calculated, but Table 5.4 summarizes four alloy compositions.

Table 5.4. Calculated atomic interdiffusivity coefficients of Ni and W atoms in the FCC lattice at several temperatures and compositions.

	Pure Ni (m^2/sec)	**5 at.% W** (m^2/sec)	**10 at.% W** (m^2/sec)	**15 at.% W** (m^2/sec)	**Pure Ni : 15 at.% W Ratio**
25 °C	9.9E-55	9.4E-56	1.1E-56	4.0 E-57	***245***
437 °C	5.2E-26	2.1E-26	9.0E-27	4.5E-27	***12***
728 °C	5.3E-20	2.8E-20	1.6E-20	9.6E-21	***6***
1019 °C	1.1E-16	6.9E-17	4.5E-17	3.1E-17	***4***
Q_m (kJ/mol)	-282	-288	-294	-296	***95%***

The primary observations after completing the DICTRA analysis are that $\widetilde{D}$ increased with increasing temperature but decreased with increasing W-content, and the activation energy for lattice diffusion increased with increasing W-content. The interdiffusivity expectedly increased with temperature considering diffusion is an Arrhenius behavior, but the moderately strong dependence of interdiffusivity on W concentration was surprising. The $\widetilde{D}$ ratio between pure Ni and 15 at.% W is ~245 at 25 °C and ~4 at 1019 °C (*i.e.* diffusion is 245 or 4 times faster in pure Ni than Ni-15 at.% W). Furthermore, the lattice diffusion activation energy of pure Ni is 95% of the lattice

diffusion activation energy in a 15 at.% W alloy. Increasing Mo concentration has been observed to similarly decrease interdiffusivity in a Ni-based solid solution [119]. The Ni-W and Ni-Mo systems are similar because Mo is in the same elemental group as W in the periodic table. Although, the Ni-W diffusion calculations of this thesis show that W has a stronger influence on interdiffusivity than Mo, most likely because W is a heavier atomic species and it should more induce higher strains in the lattice per atom.

Determining that interdiffusivity in the Ni(W) decreases with increasing W concentration is important, but the grain growth rate depends on the atomic diffusivity across the grain boundary. Therefore, it will be assumed that the activation energy for grain boundary diffusion is ½ the activation energy for lattice diffusion [120]. Because the activation energy relates to the slope of diffusivity in a log plot, the same trend of reduced grain boundary diffusivity should occur. The only difference between grain boundary diffusion and lattice diffusion is that temperature is not as sensitive when comparing the grain boundary interdiffusivity between different alloy compositions.

There are many assumptions included in this interdiffusivity analysis and they should be outlined to keep everything in perspective. First, nanocrystalline materials have large amounts of triple lines and their contribution to bulk diffusivity and grain growth were not considered. Nanoscale grain sizes create higher grain boundary volume fractions in the bulk, and more atoms may migrate in the grain boundary compared to larger grained materials. It was also assumed that solute segregation (from intentional solutes or impurities) does not slow grain boundary diffusion. Solute segregation would alter the chemistry of the grain boundaries and could also change the local strain on the boundary.

The influence of impurity segregation has been tested in nominally pure Ni nanocrystalline alloys that have slightly different purity levels [121]. In 99.99 wt.% pure materials, Prokoshkina *et al.* determined that grain boundary self-diffusion does not depend on grain size, but if the purity is reduced to 99.6 wt.%, the grain boundary self-diffusion is roughly 1000 times slower if the grain size is above 100 nm. They explained the difference to fact that larger grain materials have higher impurity because there is less grain boundary volume for the impurities to occupy, thereby increasing the number of diffusion obstacles [121]. Lastly, it was assumed that nanocrystalline grain growth occurs by the atom hopping mechanism. If grain rotation was the real mechanism, diffusion across the grain boundary is not as important. Despite the many assumptions used for this analysis, the DICTRA calculations are preliminary and are designed to serve as proof-of-concept calculations.

Ni and W diffusivity coefficients have also been experimentally determined elsewhere [122–124]. Walsh and Donachie derived an equation for Ni and W interdiffusivity [122]:

$$\widetilde{\mathrm{D}} = 1.19 \exp(-0.0469 C_w) \exp\left(\frac{-3.69x10^4}{T}\right) \quad (17)$$

where C_w is the concentration of W (at.%) and T is the temperature (°C). As seen in Equation 17, $\widetilde{\mathrm{D}}$ has an exponential dependence of temperature and W concentration. To compare these experimental results to the computational interdiffusivity results presented above, $\widetilde{\mathrm{D}}$ coefficients were calculated using Equation 17. The values computed from Equation 17 predicted a significantly smaller W concentration dependence on interdiffusivity. In addition, Equation 17 predicts that $\widetilde{\mathrm{D}}$ of pure Ni is only twice the $\widetilde{\mathrm{D}}$ of Ni-15 at.% W regardless of temperature. Another similar experimental study conducted by

Karunaratne *et al.* also predicted that the W content does not heavily influence $\widetilde{D}$ [123]. The large divide between theoretical and experimental $\widetilde{D}$ measurements is troubling. However, the experimental conditions in both experiments do not match the conditions calculated with DICTRA. The temperatures tested by Walsh and Donachie were between 1000 °C and 1316 °C, and the composition range of Karunaratne *et al.* was between 0 at.% W and 3.5 at.% W. Karunaratne also tested temperatures in-between 900 °C and 1300 °C. Therefore, it may not be reasonable to extrapolate the equations to fit the theoretical results because the experimental conditions did not match the simulated DICTRA conditions.

The simulated grain growth rates because of reduced lattice interdiffusivity can be compared to the experimental grain growth results of electrodeposited alloys that were within the Ni(W) single phase regime. Figure 5.22 shows ion-channeling contrast images of 5 and 15 at.%W alloys annealed at 728 °C for 24 hrs. The average grain diameters of each alloy were 2100 nm and 550 nm, respectively (i.e. the grains in the 5 at% W alloy are 4× larger). Using the data summarized in Table 5.4, and assuming differences in grain growth are only because of differences in diffusivity, the ratio of grain size should have been roughly 3. Thus, reduced grain growth due to reduced atomic diffusivity is reasonable. Furthermore, this result closely matches the experimental diffusivity measurements of Walsh and Donachie who predicted that the ratio of measured grain sizes should be a factor of 2.

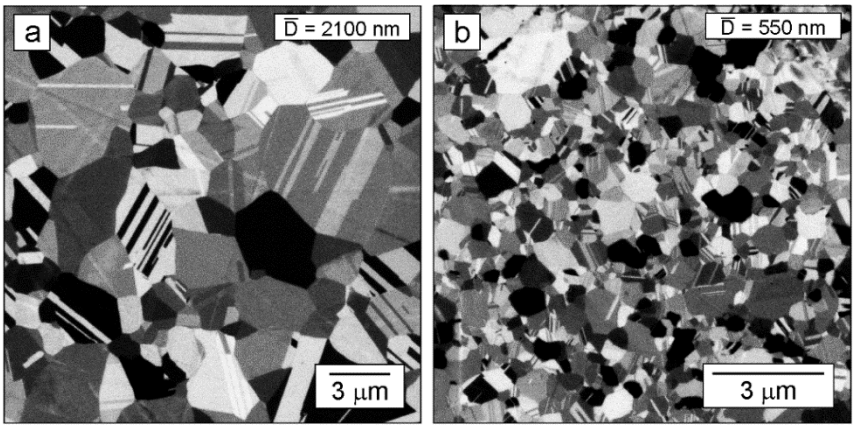

Figure 5.22. Ion-channeling contrast images of 5 and 15 at.%W alloys annealed at 728 °C for 24 hrs showing the difference in grain growth rate as a function of W-content.

Reduced lattice diffusivity has been already been suggested as a Ni-W thermal stability mechanism [78]. Atom probe tomography experiments of a Ni-18 at.% alloy were conducted and it was concluded that reduced W mobility was the cause for stagnated grain growth. The experiments observed an excess of W on the grain boundaries in the as-deposited state and at 400 °C amounting to roughly 26 and 32 at.% W, respectively. After annealing at 700 °C, the W dissolved into the Ni(W) grains and produced a supersaturated solution. Interestingly, carbon segregation was also observed to the grain boundaries at 700 °C. Despite the W-enriched grain boundaries, the authors concluded the thermal stability below 700 °C was due to low W mobility in the disordered FCC lattice. Grain growth was not observed until 700 °C, where the W diffusivity through the Ni(W) lattice increased roughly 7 orders of magnitude.

5.5 Influence of Impurity Oxides on Grain Growth

These alloys discussed in this section contained more impurities than the alloys electrodeposited by Lehigh. As a result, the thermal stability mechanisms were different than the alloys with less contamination. The influence of oxide impurities on the thermal stability mechanisms will be discussed.

5.5.1 Nanoscale Oxide Particle Drag

The oxide particle size and volume fraction of the 700 °C – 4 hr alloy were quantified to assess if the particles could stagnate grain growth. However, the Zener assumptions introduced in section §2.3.2 were not valid in this experiment: the oxide particles were not inert since they precipitated, they coarsened, and they were preferentially located on the grain boundaries. Nonetheless, a particle drag equation developed by Doherty was used [125]. Doherty modified the classic Zener equation to more realistically describe an evolving microstructure. His primary modifications were to correct for the assumption that the particles are randomly distributed in the microstructure, to more accurately describe grain boundary curvature mathematically, and to reduce the theoretical maximum force exerted by the particles since the particle centers are not always located on the interfaces. The equation is given below:

$$\bar{R} = \frac{0.2r}{f} \tag{18}$$

where $\bar{R}$ is the average Ni(W) grain radius, r is the average particle radius, and f is the particle volume fraction. If 12.5 nm and 2.2 nm that represent the average grain radius and particle radius, respectively, are inputted into the equation, the estimated critical particle

volume fraction to inhibit grain growth is roughly 3.5% (i.e. grain growth is stagnated with a particle volume fraction above 3.5%).

A particle volume fraction of 3.5% is qualitatively reasonable considering the large number of particles seen in Figure 5.7, but experimentally determining the total particle volume fraction using (S)TEM is not trivial. Assuming that the oxide particles are smaller than the sample thickness, direct 2-D measurements that analyze projected images are not accurate because it is unknown how much material is above or below the particles. To properly estimate the particle volume fraction, the measured particle areas are converted to equivalent spherical volumes, summed within a single image, and divided by the image volume (*i.e.* width × height × sample thickness). The most unknown variable here is the TEM sample thickness. Electron energy loss spectroscopy is the most common technique to measure sample thickness [126], but this technique was not available at Lehigh. Therefore, a technique that utilizes backscattered electron images was utilized to determine the sample thickness. The methodology is discussed in detail in Appendix B. The BSE thickness determination technique determined that the sample thickness of the images was 15 nm. Subsequently, the total particle volume fraction was calculated to be 2.7 ± 0.7%. The 0.7% error was calculated according to the student's t-test. The total particle volume fraction is less than the required 3.5%, but considering the assumptions and the high experimental error involved in the volume fraction measurement, the experimental value is within reason of the theoretical volume fraction. Thus, there is substantial evidence that the nanoscale oxide particles limited grain growth.

To confirm that the particles limited grain growth, small coupons of the as-deposited alloys provided by UCSD were annealed at Lehigh in a N_2-5% H_2 atmosphere at 700 °C for 4 hrs. This annealing treatment produced microstructures that contained significantly less oxide particles. When oxide particles were observed in the N_2-5%H_2 alloys, they were organized in clusters that than ran perpendicular to the substrate, as seen in the STEM-HAADF image of Figure 5.23a. Figure 5.23b and Figure 5.23c compare TEM-BF images of the LU and UCSD alloys, respectively, to show differences in Ni(W) grain size. The grains in the LU alloy that did not have oxide particles were on average 10x larger than the UCSD annealed specimen with the oxide particles. The LU sample was at least 300 nm, and the average grain size in the UCSD sample was 25 nm. Once again, after comparing microstructures with and without nanoscale oxide particles, there is strong evidence supporting particle drag as a dominant thermal stability mechanism.

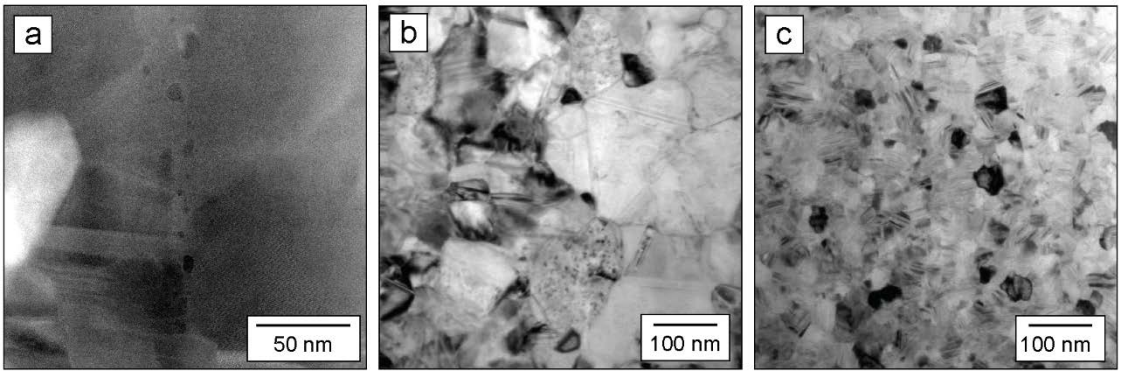

Figure 5.23. Comparison between Ni-23 at.% W alloys with and without oxide particles: (a) STEM-HAADF image showing a cluster of oxide particles found in the Lehigh annealed specimen, (b) TEM-BF image of the LU sample that exhibited 300 nm grains, and (c) TEM-BF image of the UCSD sample that exhibited 25 nm grains.

5.5.2 W-segregation to Oxide Phase Boundaries

Another phenomenon that is related to the impurity oxide particles was W-segregation to Ni(W)-oxide and Ni_4W-oxide phase boundaries. Figure 5.24a shows W-segregation to an oxide-Ni(W) interface and Figure 5.24c shows W-segregation to an oxide-Ni_4W interface. Figure 5.24b and Figure 5.24d are magnified regions from the white outlines. The high intensities in the four STEM-HAADF images suggest that the phase boundaries are rich in a heavy element (*e.g.* W). The oxide particle that was in contact with Ni_4W was much larger because it was observed in the LU Ni-21at.%W alloy that was annealed for 24 hrs in a reducing N2-5% H2 atmosphere.

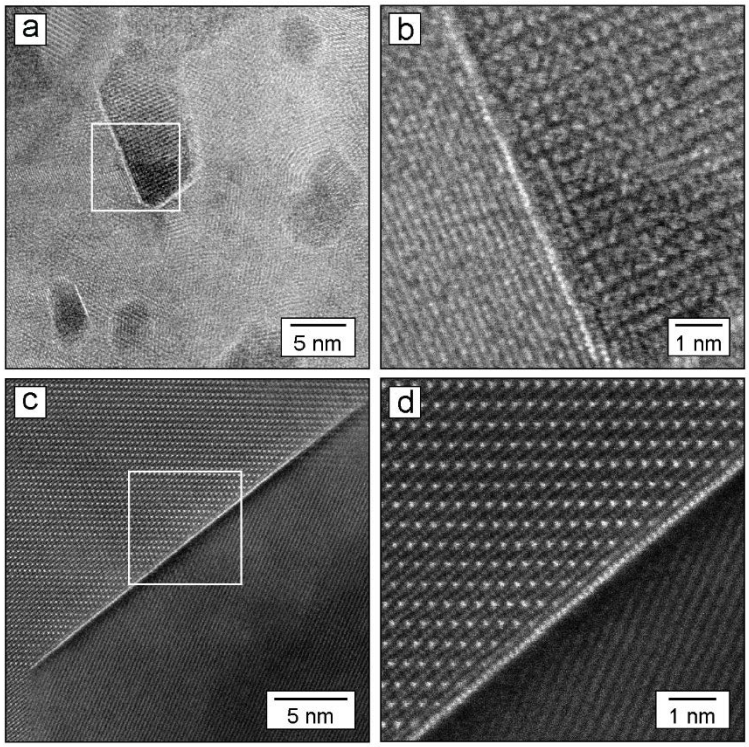

Figure 5.24. STEM-HAADF images of W-segregation to the oxide phase boundaries in contact with (a,b) Ni(W) grain and (c,d) Ni4W grain. The white boxes denote the magnified region in parts (b,d). Parts (a,b) were modified from Ref. [95].

W-segregation to the oxide phase boundaries was confirmed with STEM-EDS and results from an EDS line profile are shown in Figure 5.25. The increase of Ni-Kα intensity over W-Lα intensity confirms an excess of W on the phase boundary. The Ni-Kα and W-Lα peaks were quantified because they are not as readily adsorbed as the softer Ni-Lα and W-Mα X-rays. However, the W-Lα peak overlaps with the Ni-Kβ peak. To overcome the peak overlapping, the DeskTop Spectrum Analyzer II (DTSA-II) was used to simulate the ratio between Ni-Kα and Ni-Kβ to subtract the Ni-Kβ counts from the integrated W-Lα + Ni-Kβ peak. The ratio was 0.0879. W-segregation to the oxide phase boundaries is important because it may theoretically suppress oxide particle coarsening; W-segregation may reduce the phase boundary energy analogous to the thermodynamic mechanism. Particles that do not grow will more effectively anchor the matrix grains.

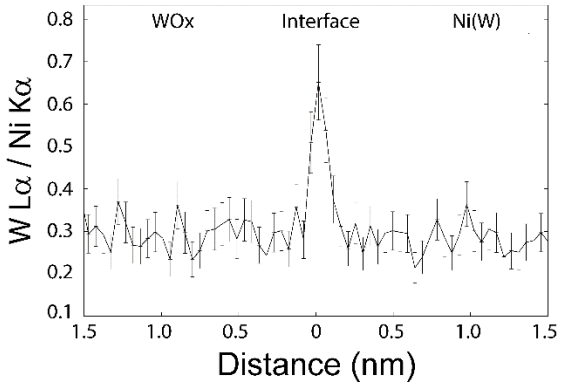

Figure 5.25. STEM-EDS line scan quantifying W-segregation on a Ni(W)-oxide phase boundary.

5.6 Dominant Thermal Stability Mechanisms?

Multiple thermal stability mechanisms were observed in the electrodeposited alloys, including W-segregation, short- and long-range chemical ordering, reduced atomic diffusivity, and nanoscale particle drag. Unfortunately, the stability mechanisms were not

isolate in the “clean” alloys and it is not possible to identify the dominant mechanism. Similarly to Cu-Ta and Ni-P, it is possible that W-segregation slowed grain growth at low temperatures via reduced grain boundary energy and/or solute drag, even though there was not strong evidence of W-segregation to all the Ni(W) grain boundaries. However, it is also possible that reduced diffusivity is responsible for reduced grain growth at low temperatures. On the other hand, grain growth of the highly contaminated alloys was clearly suppressed by nanoscale particle drag. The particle sizes and volume fractions were close to the required dimensions according to the Zener particle pinning theory. W-segregation and reduced diffusivity could also be limiting grain growth of these alloys, but the particle drag is highly likely the dominant thermal stability mechanism. Overall, the thermal stability of Ni-W is due to several mechanisms, and the relative importance of the individual contribution of each mechanism is influence most strongly by the phases that exist within the microstructure.

5.7 Chapter Summary

The promising thermal stability of nanocrystalline Ni-W is attributed to several stability mechanisms. In addition, the alloy purity is critical. The significant findings are listed below:

1. Alloys with bulk W concentrations greater than 5 at.% W were stable up to 437 °C, but all alloys exhibited grains larger than 100 nm and were unstable above 728 °C.
2. The 12 at.% W, 15 at.% W, and 17 at.% W alloys exhibited abnormal grain growth at 437 °C and 728 °C. The cause of abnormal grain growth was not determined as differences in long-range Ni_4W ordering or W-segregation were not detected.

3. W-segregation to Ni(W)-Ni(W) grain boundaries was not observed with atomic-resolution images in as-deposited or annealed alloys. W-segregation was detected and quantified with STEM-EDS, but the results were not definitive based on statistical requirements. Further research is needed to confirm these observations.
4. Lattice contraction after annealing at 437 °C, without secondary phase precipitation, is potentially indirect evidence of W-segregation. Again, more STEM analysis is required to confirm the possibility of W-segregation.
5. Long-range Ni_4W chemical ordering was observed in the 21 at.% W alloy after annealing at 700 °C for 4 hrs. The Ni_4W domains were discontinuous, 5 nm in diameter, and a small fraction were located on the grain boundaries. The 21 at.% W after annealing at 728 °C for 24 hrs exhibited a large and continuous single domain.
6. DICTRA simulations determined that reduced diffusivity with increasing bulk W-concentration is a potential thermal stability mechanism at low temperatures. The ratios of diffusivity and grain growth between the 5 at% W and 15 at% W alloys at 728 °C were close in comparison.
7. Particle drag reduced grain growth in alloys that have high oxygen impurity concentrations. Nanoscale oxide particles were of sufficient size (4.5 nm) and volume fraction (2.7%) to stagnate grain growth of 25 nm Ni(W) grains at 700 °C.
8. W-segregation was identified on WOx phase boundaries and potentially improved the coarsening resistance of the particles. Thus, the stable particles more effectively anchored the Ni(W) grains.

Chapter 6 Re-evaluating Ni-W Phase Stability

Chapter 5 outlined the thermal stability mechanisms of nanocrystalline Ni-W. This chapter will investigate Ni-W phase stability to strengthen the fundamental thermodynamic understanding of this system. Nanocrystalline alloy design strongly consider phase diagrams and the characteristics that define them (*e.g.* solid solubility, heat of segregation, second phase precipitation, etc.). Therefore, it is imperative that the accuracy of these phase diagrams be validated. Interestingly, the results of this research indicates that the previous Ni-W phase diagrams are not completely accurate and that the role of critical impurities, such as carbon and oxygen, are often overlooked. Most of the results discussed in Chapter 6 are from Density Functional Theory calculations, and when possible, DFT results are compared to experimental results from the electrodeposited alloys. At the conclusion of this chapter, it will be clear how Ni-W phase stability relates to grain growth and why it is important to control phase stability

6.1 Ni-W Binary Phase Diagram

There are at least 15 different Ni-W binary phase diagrams found in the literature. Interestingly, there is a divide in which half of the phase diagrams do not contain the NiW and NiW_2 intermetallics, while the other half of the diagrams do contain them. Figure 6.1 shows examples of each case (note: the Ni-rich portion of Figure 6.1b is on the right). Considering that phase stability is important to properly design nanocrystalline Ni-W alloys, more comprehensive studies on phase stability are needed to clarify which set of phase diagrams are more reliable.

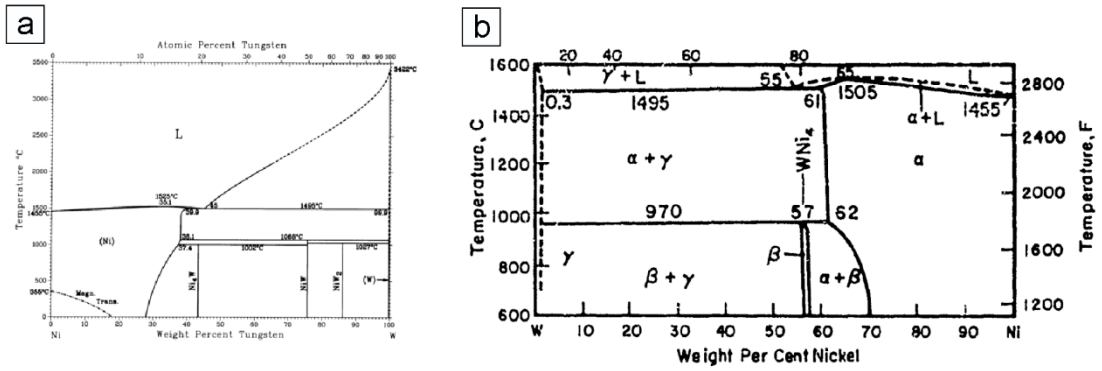

Figure 6.1. Ni-W binary phase that diagrams that (a) include NiW and NiW2 [71], and (b) do not include NiW and NiW2 [149].

Density Functional Theory (DFT) calculations were used to determine if Ni_4W, NiW, and NiW_2 are thermodynamically stable. A ground-state binary phase diagram is shown in Figure 6.2a, and Figure 6.2b is an enlarged view of the Ni-rich portion. The x-axis of each diagram is the mole fraction of W, and the y-axis is the heat of formation. Red squares or black circles represent ordered solid solutions, and the green diamonds are not ordered solid solutions. Furthermore, if a phase is below the horizontal line (*i.e.* $\Delta H(x)=0$), the phase is considered to be thermodynamically stable at 0 K, and if a phase is above the horizontal line, the phase is thermodynamically unstable at 0 K. Lastly, for any given concentration, the phase with the lowest heat of formation is the most stable. Therefore, the DFT calculations have determined that intermetallic Ni_4W is stable, and that intermetallics NiW and NiW_2 are unstable. In addition, the intermetallic Ni_8W, which is not found on any ASM phase diagram, was determined to be thermodynamically stable.

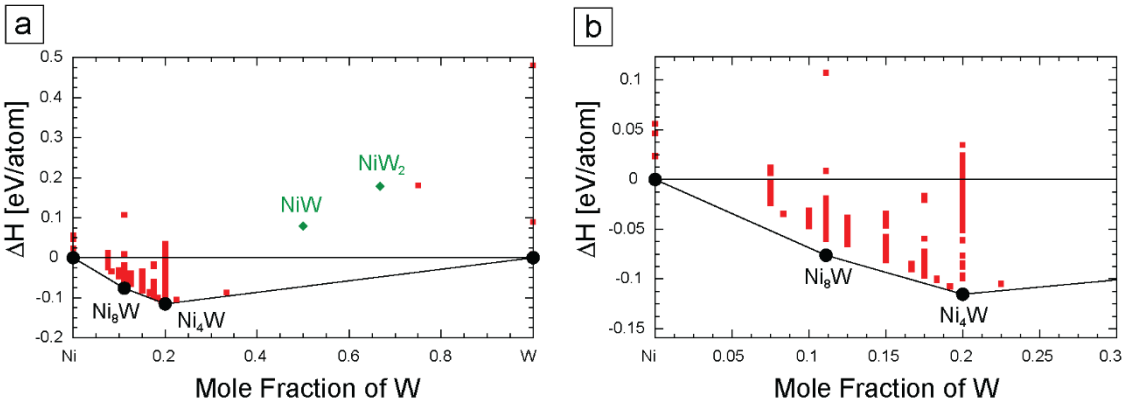

Figure 6.2. Ground-state binary Ni-W phase diagrams derived with Density Functional Theory that indicate the intermetallics NiW and NiW_2 are thermodynamically unstable.

Other reports in the literature have identified Ni_8W and Ni_4W using ground-state first principles calculations [127,128]. Schindzielorz *et al.* showed that Ni_8W undergoes an ordering transition at 800 K and a disordering transition above 1300 K [127]. Although Ni_8W is stable in the ground-state, the ordering kinetics are not sufficient at low temperatures because long-range diffusion is necessary. As discussed in section §5.5, diffusivity is relatively low at temperatures less than 700 K. Limited kinetics may be responsible for the lack of experimental evidence of Ni_8W and its representation on any ASM phase diagram.

Analysis of equilibrium phase diagrams for Ni-W intermetallics is critical to accurately identify the region of phase separation, which is often avoided when designing nanocrystalline alloys [33]. Phase separation threatens the thermodynamic mechanism of solute segregation because the solute that is segregated to the grain boundaries might preferentially migrate to newly formed secondary phases. Furthermore, if phases on a diagram are incorrectly represented, the thermal stability is less predictable because different phases could precipitate. As a result, the unexpected secondary phases will

presumably undermine the proposed thermodynamic. Considering that the results discussed above indicate that NiW and NiW_2 are not stable, the Ni-W system likely behaves differently than what most have expected above 20 at.% W. A two-phase equilibrium between Ni(W) and pure W will exist at all compositions beyond 20 at.% W, and not a two-phase equilibrium between Ni(W) and NiW. Again, this is important because if W-segregation were to occur, the pure W grains would attract the segregated W from the boundaries. However, pure W will likely attract excess W atoms more quickly than NiW since pure W requires more W atoms to grow.

6.2 Grain Boundary Ni_4W Nucleation

The precipitation of pure W understandably alters Ni-W thermal stability, yet an open question that remains is whether Ni_4W has the same effects. On the one hand chemical ordering can slow grain growth by particle-like drag or reduced diffusivity. However, the long-range ordering of Ni_4W may also eliminate the beneficial effects of W-segregation on the grain boundaries. As a result, the overall thermal stability may worsen. Kingsetsu *et al.* have shown that Ni_4W preferentially nucleates on free surfaces at elevated temperatures between 860-950 °C in a Ni-16.6 at.% W alloy with field ion microscopy [109]. Similarly, other ordered phases have been shown to precipitate on grain boundaries and grow towards the center of the grain. For instance, Irani and Cahn observed CuPt ordering more frequently on grain boundaries than grain interiors, and that the largest and fast-moving domains that nucleated on the grain boundaries consumed the smaller nuclei that were located in the center of the grains [129]. Assuming that grain boundaries are internal surfaces, these results would indicate that Ni_4W nucleation preferentially occurs on grain

boundaries. If this is the case, Ni_4W precipitation could pull W atoms from the grain boundaries similarly to pure W precipitation.

DFT was used to investigate the energetics of Ni_4W nucleation on a grain boundary. A Σ5 boundary was chosen, and it was determined that there was a relative energy of -0.16 eV / W atom if Ni_4W nucleates in the bulk, and a relative energy of -0.42 eV / W atom if Ni_4W nucleates on the grain boundary. Both energies are relative to random W impurities in the Ni(W) lattice. Thus, DFT shows that Ni_4W nucleation is more energetically favorable on a grain boundary (although this analysis only considers one special grain boundary). Assuming Ni_4W is attached to a grain boundary, DFT was used to further evaluate the possibility of reducing the grain boundary energy. Remarkably, a Ni_4W bi-layer reduced the energy of a Σ5 (001) grain boundary by 30%, and a Ni_4W quad-layer reduced the grain boundary energy by 55%. Thus, Ni_4W nucleation on the grain boundary provides an energetic benefit analogous to the thermodynamic stability mechanism. Now, if the kinetic effects of Ni_4W (*e.g.* chemical ordering or solute drag) are combined with the thermodynamic effects, it can be argued that Ni_4W precipitation is a very promising mechanism to limit grain growth.

6.3 Ni_6W_6C Identification

Referring to section §5.1, the ternary carbide Ni_6W_6C was identified in the electrodeposited 21 at.% W and 23 at.% W alloys. However, according to the binary phase diagrams found in the literature, the W-rich phase should have been the intermetallic NiW because the alloy compositions are located in the Ni_4W-NiW two-phase regions. To prove that the W-rich phase was Ni_6W_6C and not NiW, electron diffraction, STEM-EDS, and

atomic-resolution imaging were conducted [130]. Figure 6.3 shows electron diffraction and STEM-EDS results from a Ni_6W_6C grain in the 23 at.% W alloy. The diffraction spots inside the Ni(W) (111) ring correspond to Ni_6W_6C. Furthermore, the nearly equivalent Ni Kα and W Lα intensities in Figure 6.3b suggest that Ni and W are in equal proportions, but the key was that the C Kα peak was much larger in the carbide phase than the Ni(W) matrix [130]. The atomic-resolution HAADF images in Figure 6.4 were identical to the VESTA structures on the [100], [110], and [111] crystal directions. Here, the dark grey, light grey, and red atomic columns in the VESTA structures represent Ni, W, and C atomic columns, respectively. The Ni and C columns in the HAADF images are not easily observed because less signal was produced on those atomic columns.

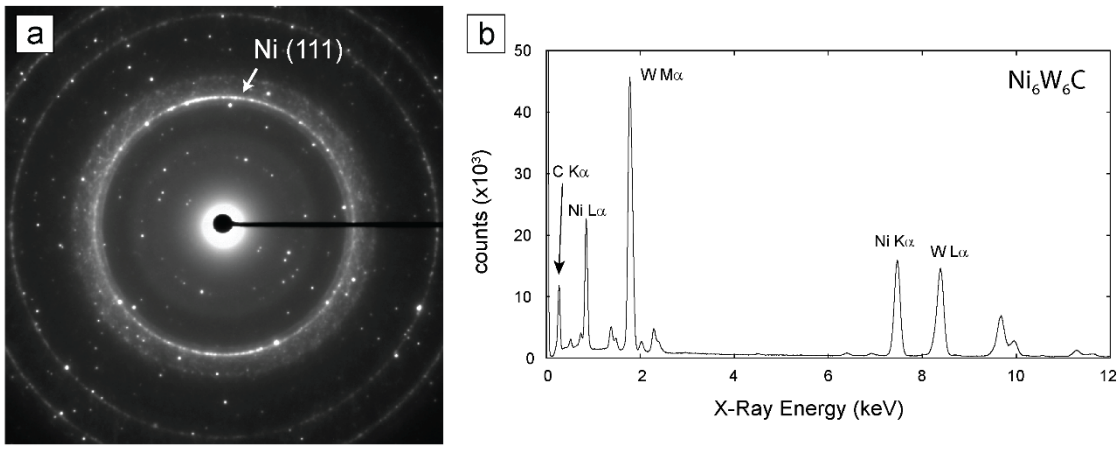

Figure 6.3. (a) SADP and (b) STEM-EDS of the Ni_6W_6C phase identified in the electrodeposited alloys.

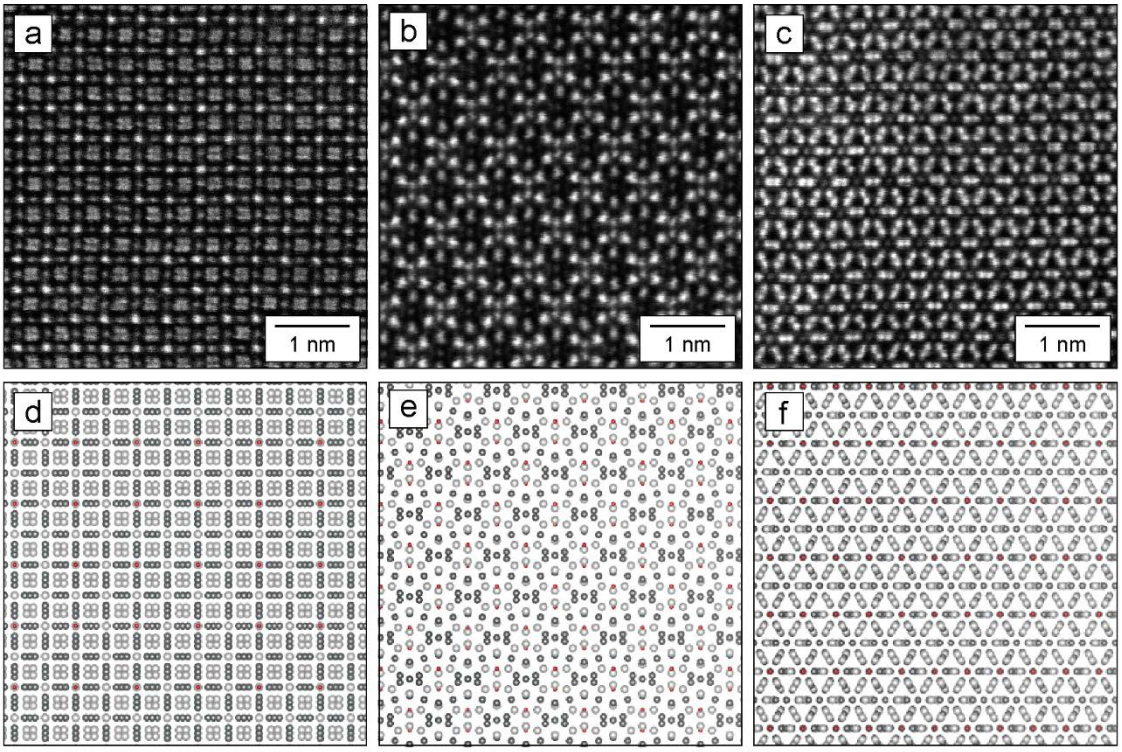

Figure 6.4. STEM-HAADF images of Ni_6W_6C on the (a) [100], (b) [110], and (c) [111] zone axes and matching projected atomic positions simulated with VESTA of the (d) [100], (e) [110], and (f) [111] directions. Note: The dark atoms in the VESTA structures are Ni, the light grey are W, and the red are C. All parts are modified from Ref. [130].

Ni_6W_6C precipitation in Ni-W alloys has been observed by several authors [97,131,132]. Cury *et al.* argued that the intermetallic phases NiW and NiW_2 are in reality the ternary Ni_6W_6C and Ni_2W_4C carbides [131]. Cury also claimed the experiments that originally identified NiW and NiW_2 were prone to carbon contamination, and since the atomic ratios of Ni and W are 1:1 in both NiW and Ni_6W_6C, the initial investigators misidentified the crystal structures. Overall, these arguments agree with the DFT studies of this thesis in that NiW and NiW_2 are thermodynamically unstable.

In a different study, Borgia *et al.* detected Ni_6W_6C in sputtered alloys, but did not correctly identify the phase as Ni_6W_6C [112]. Throughout their discussion, they named the

unknown phase “X”, and used CBED to determine that the crystal structure was Fd3m (Ni_6W_6C). The misidentification of Ni_6W_6C, or the lack thereof, potentially leads to incorrect conclusions regarding microstructure or mechanical properties of Ni-W alloys. For instance, one study investigated the carburization potential of Ni-W to produce cemented carbides [133]. The authors electrodeposited Ni-W alloys with W contents up to 20 at.% W, annealed them in inert (pure Ar) or carburizing (mixture of Ar and ethanol) atmospheres at 800 °C, and analyzed the microstructures with XRD to determine which phases were present. Interestingly, the authors identified “NiW” in the inert alloy. Upon annealing a different section in the carburizing atmosphere, they did not observe WC as they expected, but still detected “NiW”. Thus, it can be inferred that Ni_6W_6C was present in their samples after annealing in the carburizing *and* the inert atmosphere.

6.4 Ni-W-C Ternary Phase Diagrams

The previous section clearly identified that carbon contamination is more prevalent than currently realized, to such a degree that half of the binary phase diagrams in the literature have unknowingly detected it. Therefore, if carbon contamination is inevitable, it is beneficial to design nanocrystalline Ni-W alloys using the ternary Ni-W-C phase diagram instead of the binary Ni-W phase diagram.

There are a few published Ni-W-C isothermal phase diagrams, but the temperatures do not match the experimental conditions of this thesis [134–136]. Therefore, first principles calculations were used to calculate Ni-W-C ternary phase diagrams at temperatures of interest. Figure 6.5a shows a 927 °C isothermal section of a Ni-W-C ternary phase diagram. 927 °C was chosen because it is slightly below the Ni_4W

disordering transformation temperature. The Ni-rich region of the diagram was enlarged in Figure 6.5b.

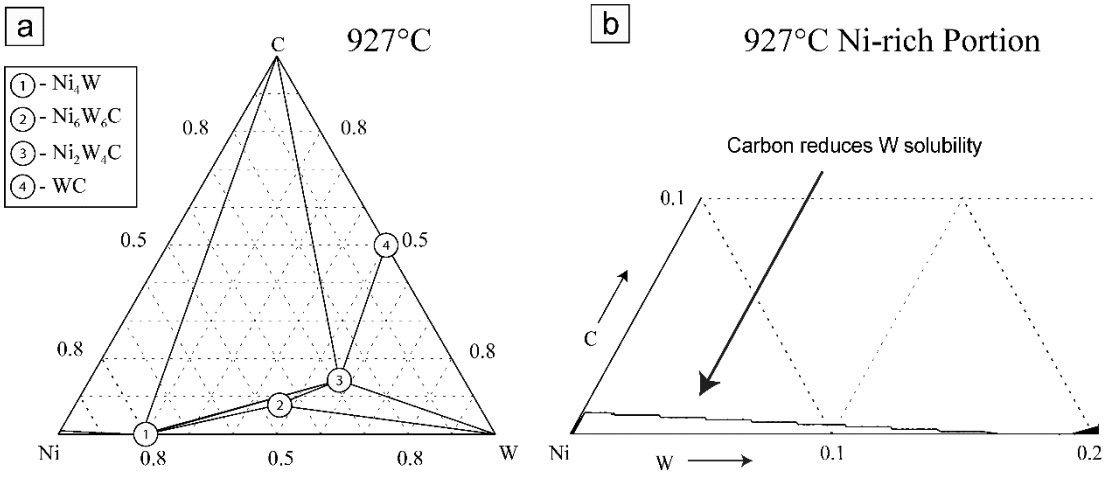

Figure 6.5. Ni-W-C ternary phase diagrams at 900 °C showing the (a) full composition range and (b) an enlarged view of the Ni-rich portion.

The 927 °C ternary phase diagram matches well with the experimental results of the 21 at.% W alloy annealed at 700 °C. At this alloy composition and temperature, the ternary diagram indicates the alloy exists in a three-phase region consisting of Ni_4W, Ni_6W_6C, and pure W. Likewise, the STEM-HAADF image in Figure 6.6 shows the Ni(W), Ni_6W_6C, and pure W phases in the annealed alloy, including the STEM-EDS spectra that confirmed their composition. The only difference between the experimental and computational results is that Ni(W) was found in the annealed alloy but not in the calculated ternary diagram. It is possible that after longer annealing times the Ni(W) grains will transform into Ni_4W. Nonetheless, the calculated ternary phase diagrams are validated with the experimental results.

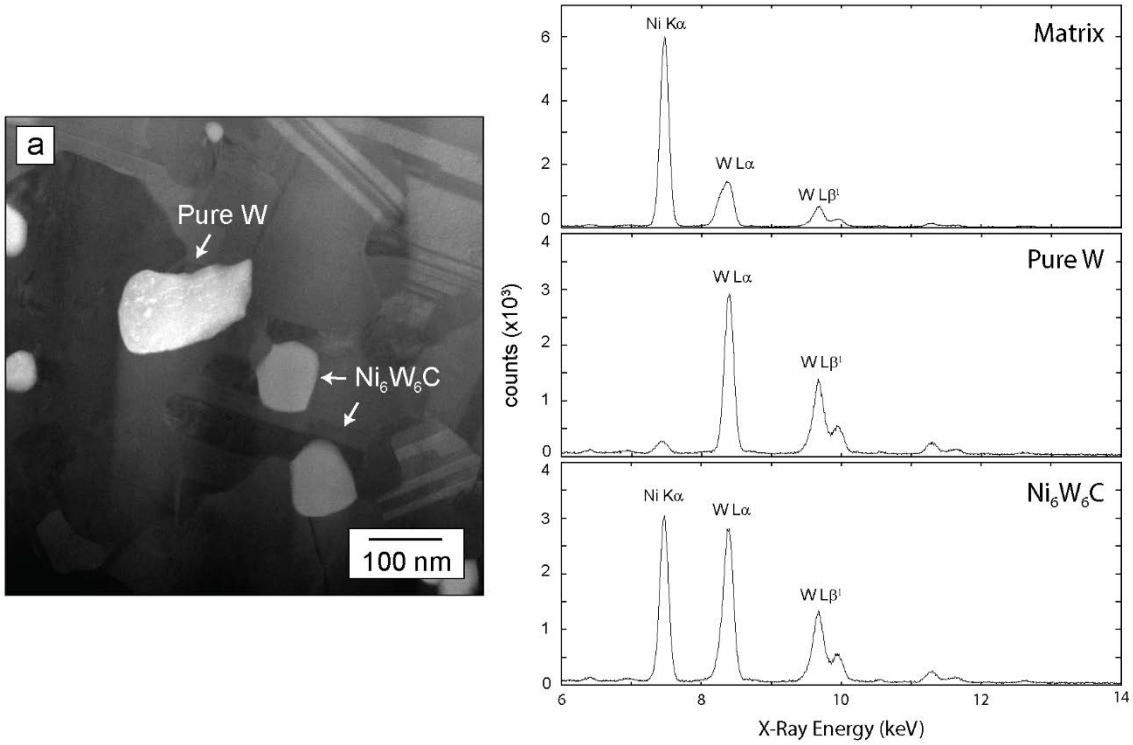

Figure 6.6. (a) STEM-HAADF image of the electrodeposited 21 at.% alloy annealed in a N_2-5% H_2 atmosphere showing the matrix, pure W, and Ni_6W_6C, and STEM-EDS spectra confirming the composition of the matrix, W, and Ni_6W_6C phases.

Another consequence of impurity carbon is the reduction of W solubility in the Ni(W) lattice. As seen in Figure 6.5b, the W solubility inversely scales with the carbon content. The trend of reduced solubility was more severe at the lower temperatures where smaller C concentrations limited the maximum solubility even further. The C concentration needed to inhibit any W solubility in Ni was ~900 at. ppm C and ~460 at. ppm C at 900 °C and 25 °C, respectively. The DFT simulations indicated that it is unfavorable for C and W to be first nearest neighbors, and with increases in W concentration, there are less atomic potential sites for C to occupy. Now, the open question is what happens to the W-segregation tendency if the W solubility in the Ni(W) lattice decreases? Referencing the notion that segregation tendency scales inversely with solid solubility, it can be argued that

the W rejected from the lattice segregates to the grain boundaries. In this sense, the thermodynamic stabilization mechanism would be stronger. However, it is also possible that Ni_6W_6C precipitates, or C atoms segregate to the grain boundaries. The likelihood that C segregates to the grain boundaries is high considering that C solubility in Ni is low [ref], and if W is added to the solution, the C solubility should be even lower. Thus, W solubility will increase as C leaves the solution and the segregation tendency would correspondingly decrease. Ultimately, the interplay between C and W solubility in the Ni(W) lattice is complicated.

6.4 Impact of Oxygen on Phase Equilibria

The strong influence of oxygen impurities on the thermal stability by nanoscale particle drag was clearly defined in section §5.5. In this section, it will be shown that the oxygen impurities also influenced the phase stability. First and foremost, nanoscale oxides were present if there were high levels of oxygen contamination, as shown in the UCSD alloys that were annealed in Ar-5% H_2. The less obvious finding was there was an absence of Ni_4W and pure W in those same alloys. In contrast, when the as-deposited UCSD alloys were annealed in N_2-5%H_2 at Lehigh, the oxygen impurities were lower, which led to a lack of oxide particles but the precipitation of Ni_4W and pure W.

Figure 6.7 compares SADPs between the highly contaminated Ar-5% H_2 alloys (Figure 6.7a) and the relatively pure N_2-5%H_2 alloys (Figure 6.7b). The two inside rings of Figure 6.7b correspond to the Ni_4W (110) crystal plane, and the ring just inside of the Ni (111) is the W (110) plane. Additionally, the areas where the Ni_4W rings would be

present, like in Figure 6.7b, are diffuse, which indicates that there could be some short-range ordering. The spots inside of Figure 6.7a correspond to Ni_6W_6C

There may be differences in thermal stability mechanisms because of the difference in phase stability. Besides the particle drag, the oxide particles drive the excess W to migrate to the oxide particles and the oxide phase boundaries, instead of dissolving into the Ni(W) lattice, which would decrease lattice diffusivity, or segregating to the Ni(W) grain boundaries to reduce the grain boundary energy. To evaluate if the oxygen impurities altered the W solubility in the Ni(W) lattice, the lattice parameters between the Ar-5%H_2 and the N_2-5%H_2 alloys were measured and determined to be 3.584 ± 0.02 Å and 3.599 ± 0.01 Å, respectively. Thus, less W dissolves in the Ni(W) lattice in the presence of oxygen impurities. Furthermore, if Ni_4W does not precipitate in the presence of oxygen, short- or long-range ordering will not occur, which in turn removes a kinetic barrier for grain growth. Likewise, the energetic benefits of Ni_4W bi- and quad-layers on the grain boundaries is also lost.

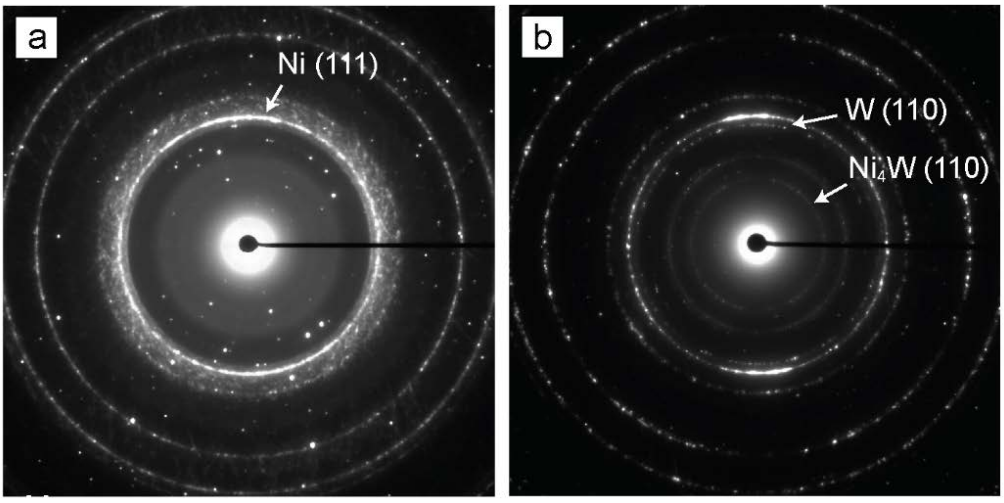

Figure 6.7. Selected area diffraction patterns of (a) Ar-5% H_2 and (b) N_2-5%H_2 showing the differences in phase stability with different annealing atmospheres.

Particle drag was identified as one of the most potent mechanism to limit grain growth in alloys with high oxygen impurities, and even produced microstructures with smaller grain sizes after annealing under the same conditions. Thus, it is important to control oxygen impurities to minimize the final grain size. Unfortunately, the source of the oxide particles in the UCSD samples was unknown. One possible explanation is that the annealing atmosphere used by UCSD (Ar-5% H_2) was not as reducing as the atmosphere used at Lehigh (N_2-5% H_2). Therefore, other annealing atmospheres were investigated to control the oxide impurities and take advantage of the nanoscale oxide particle drag. Sectioned coupons of the UCSD as-deposited alloy were annealed at 700 °C for 4 hrs in flowing N_2 or N_2-1000 ppm O_2 to compare these microstructures to the Ar-5% H2 and N_2-5% H_2 microstructures. Furthermore, one annealing treatment was conducted with a closed N_2 atmosphere to trap the oxygen in the furnace. The N_2 gas had an oxygen content of 15 ppm, and estimating that the impurity oxygen content in the UCSD alloys was >1000 wt. ppm, a 15 ppm oxygen concentration would neither drive the system to precipitate macroscopic oxide phases, or reduce the oxygen already within the alloy.

The closed N_2 alloy exhibited a similar microstructure to the N_2-5% H_2 alloy that was discussed in section §5.4.2. There was roughly 300 nm Ni(W) grains and large W and Ni_6W_6C grains. Slightly more oxide impurities were observed than in flowing N_2-5%H_2, but not nearly as many as in the UCSD Ar-5% H_2 alloys. Interestingly, the oxide particles still exhibited W-segregation to the phase boundaries. In contrast, the flowing N_2-1000 ppm O_2 atmosphere produced a significantly different microstructure. The FIB-BSE image

in Figure 6.8a shows a TEM specimen which exhibited three surface oxide layers and two regions beneath the oxide layers that did or did not contain W and Ni_6W_6C. Furthermore, the STEM-HAADF images in Figure 6.8b shows that the oxide layers ranged between ~100-500 nm in width. The STEM-EDS spectra in Figure 6.9 determined that the top oxide layer as NiOx, the middle layer as NiWOx, and the third layer as WOx. The exact stoichiometry of each oxide layer was not determined because reliable EDS standards were not readily available.

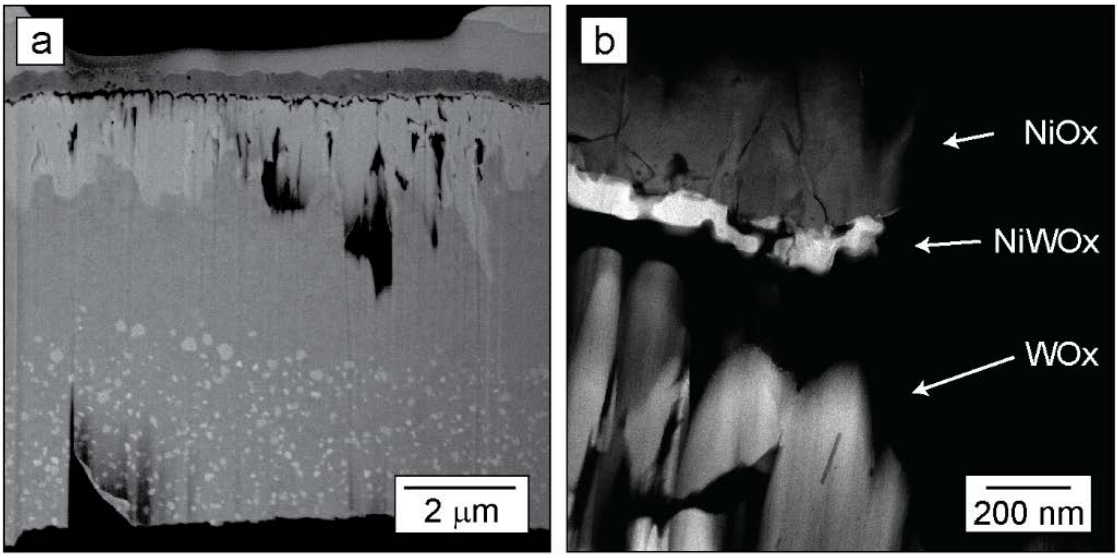

Figure 6.8. (a) SEM-BSE micrograph showing the N2-1000 ppm O_2 microstructure, and (b) STEM-HAADF image showing the three surface oxide layers.

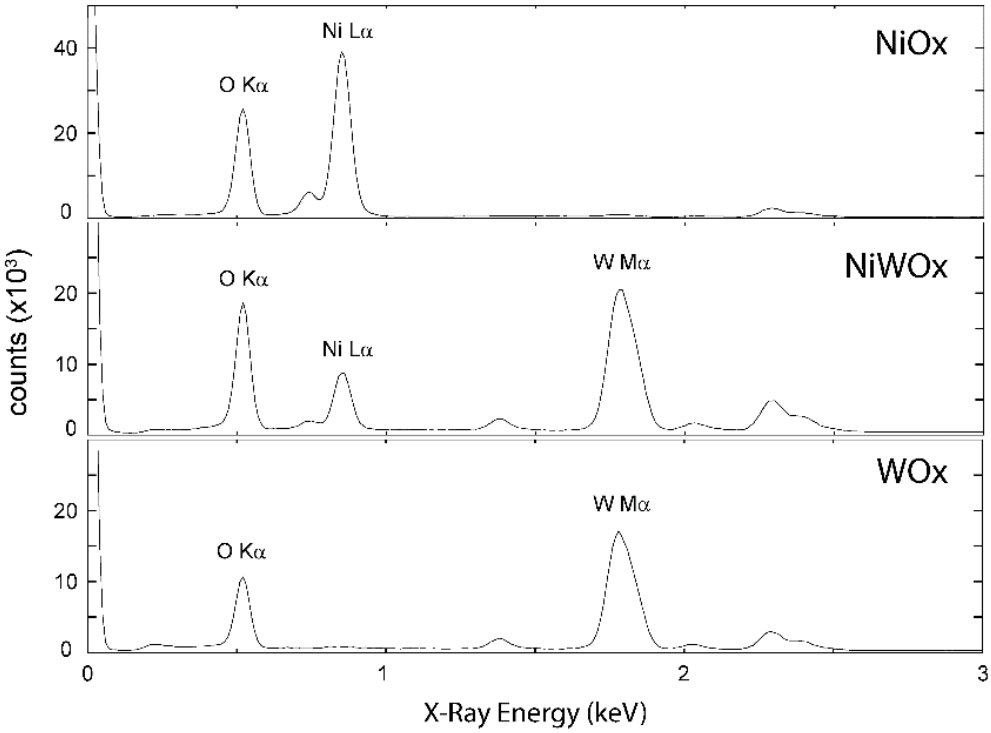

Figure 6.9. STEM-EDS spectra of the NiOx, NiWOx, and WOx surface oxide layers.

The order of the oxide layers suggest that Ni macroscopically segregated to the surface of the film and W macroscopically segregated downwards. Evidence of macrosegregation was also seen in the large regions beneath the surface oxide layers. As previously mentioned, there was a 2-3 μm wide region that did not contain pure W or Ni_6W_6C followed by a section that did have the W-rich phases. STEM-EDS spectra were collected to determine if the two regions consisted of different compositions, and the results are shown in Figure 6.10. The dashed white box in Figure 6.10a outlines the region that did not have W nor Ni_6W_6C, and the solid white box outlines the region that did have W and Ni_6W_6C. The EDS results clearly indicated that the upper region was Ni-rich, or also as W-deficient. Interestingly, the W-rich and W-deficient regions exhibited the same grain size, which suggests that grain growth stopped before the macro-segregation took place.

Unfortunately, nanoscale oxides similar to those in the UCSD Ar-5% H_2 alloy were not observed. The lack of oxide particles in the W-rich or W-deficient regions was unexpected considering the high oxygen concentrations in the system. The system was likely overdriven with oxygen from the atmosphere and the oxide layers formed instead of the nanoscale oxides. While these attempts did not productively control nanoscale oxide precipitation, a good topic for future research is to study the best methods to intentionally dope nanocrystalline Ni-W with oxygen to form beneficial oxide particles.

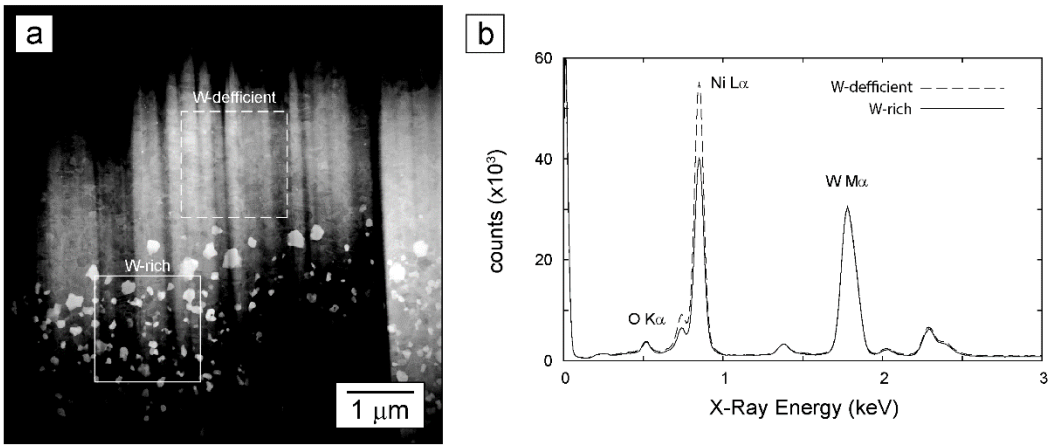

Figure 6.10. (a) STEM-HAADF image showing the W-deficient and W-rich regions of the N2-1000 ppm O2 sample, and (b) STEM-EDS of the two regions showing the difference in W content

6.5 Chapter Summary

This chapter highlighted many aspects of Ni-W phase stability in the presence of oxygen and carbon impurities with first principles calculations and STEM characterization. The significant findings are listed below:

1. The intermetallics NiW and NiW_2 were determined to be thermodynamically *unstable,* while the ternary carbides Ni_6W_6C and Ni_2W_4C were determined to be thermodynamically *stable*. If NiW and NiW_2 do not exist, and assuming the system

is free of carbon impurities, a correct phase diagram predicts that pure W will precipitate at lower W concentrations and increasingly threaten thermal stability.

2. Ni_4W precipitation is energetically more favorable on a Σ5 grain boundary than in the bulk. Furthermore, Ni_4W bi- and quad-layers reduce the Σ5 (001) grain boundary by 30% and 55%, respectively. Therefore, Ni_4W precipitation has energetic benefits akin to the thermodynamic mechanism, in addition to the kinetically beneficial chemical ordering.
3. Trace carbon reduces W solubility in the Ni(W) lattice, but the real consequence of carbon reducing W solubility in Ni(W) remains unclear. If W atoms are rejected from Ni(W) because of trace C, the W atoms are possibly more likely to segregate to the grain boundaries and thereby limit grain growth via the thermodynamic mechanism. However, it is unknown if C is stable in the Ni(W,C) solution and the effects presented above would not matter. Nonetheless, it is recommended to use Ni-W-C ternary phase diagrams to design nanocrystalline Ni-W alloys.
4. The extent of oxygen contamination controls the precipitation of oxide layers, nanoscale particles (which strongly improve thermal stability), Ni_4W, and pure W. Efforts were undertaken to control the oxygen impurities to maximize thermal stability via particle drag, but the attempts were unsuccessful.

Chapter 7 Influence of Processing on Grain Growth

Chapter 5 identified several Ni-W thermal stability mechanisms in “pure” and contaminated electrodeposited alloys, and Chapter 6 re-evaluated Ni-W and Ni-W-C phase stability. Chapter 7 will discuss the influence of other bulk processing methods on the residual stress and purity of Ni-W alloys, including any differences in levels or types of impurities, and in turn reveal any differences in the phase and thermal stabilities of each process. The other bulk processing methods that were studies include DC magnetron sputtering and mechanical alloying. As concluded in Chapters 5 and 6, the understanding and control and of alloy purity is critical, but there have not been many direct comparisons between electrodeposition, sputtering, and mechanical alloying using the same processing conditions and characterization techniques. Thus, at the conclusion of this chapter, it will be clear how different bulk fabrication processes influence Ni-W thermal stability.

7.1 DC Magnetron Sputtered Ni-W

Two sputtered alloy compositions were studied: 7 at.% W and 24 at.% W. All the films were between 1-2 µm thick and annealed at 700 °C for 4 hrs in N_2-5%H_2. There were two main objectives regarding the sputtered alloys: (1) compare and contrast the thermal and phase stability of the sputtered alloys to the electrodeposited alloys, and (2) determine if different sputtering parameters change the grain growth behavior of the 7 at.% W alloy after annealing at 700 °C.

7.1.1 Overview of Sputtered Alloys

The as-sputtered and annealed microstructures are shown in Figure 7.1. The as-sputtered 7 at.% W and 24 at.% W alloys exhibited roughly 50 nm and 15 nm columnar widths, respectively. In addition, Figure 7.1a and Figure 7.1b show that each alloy was only composed of Ni(W) grains. Upon annealing at 700 °C, the grain in the 7 at.% W alloy coarsened to 180 nm in diameter, but the grain in the 24 at.% W alloy narrowly coarsened to 35 nm in diameter. Furthermore, the 24 at.% W alloy precipitated Ni_6W_6C and WOx particles after annealing at 700 °C, similarly to the highly contaminated UCSD electroplated alloys. The bright phases in Figure 7.1d are Ni_6W_6C and a minority of the dark phases are WOx. The majority of dark phases in both the 7 at.% W and the 24 at.% W alloys were identified as trapped Ar bubbles. The Ar pores are more readily visible in the 7 at.% W annealed alloy, as seen in Figure 7.1c. All the phases were confirmed with STEM-EDS.

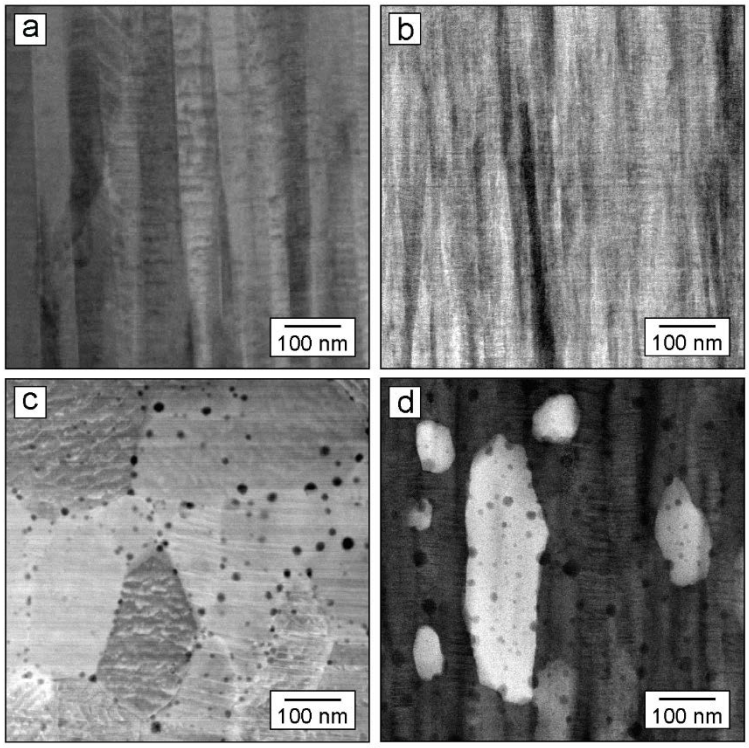

Figure 7.1. STEM-BF images of as-deposited (a) 7 at.% W and (b) 24 at.% W alloys, and STEM-HAADF images of annealed (c) 7 at.% W and (d) 24 at.% W alloys.

The Ar pores are potentially obstacles to grain growth by particle-like drag analogous to the WOx particles or Ni_4W precipitates. This notion is strengthened by the fact that Ar pores are predominantly found on the grain boundaries. The 7 at.% W alloy exhibited pores on triple points that were ~10 nm in diameter, and the 24 at.% W alloy exhibited both large Ar pores and nanoscale 2-3 nm wide Ar pores on the columnar boundaries. Figure 7.2 shows the large and nanoscale Ar pores and WOx particles in the annealed 24 at.% W alloy at higher magnifications. Remarkably the nanoscale Ar bubbles decorate the grain boundary. Lastly, the strongest evidence of particle pinning in the 24 at.% W alloy was that the grain boundary in Figure 7.2b has a distinct curvature around the WOx particle, which is a classic indication of particle drag.

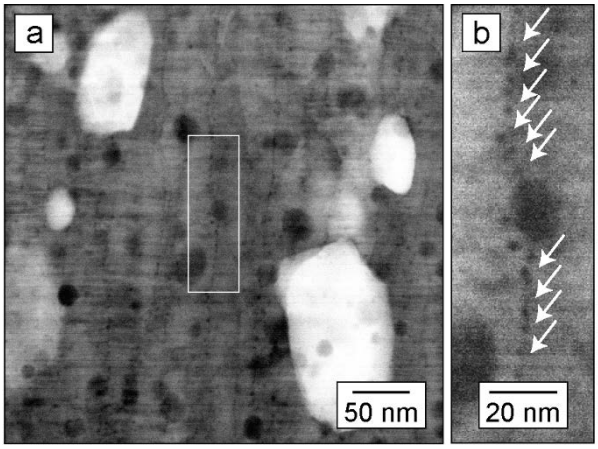

Figure 7.2. STEM-HAADF images of the sputtered 24at% highlighting the 3 nm Ar pores found on the grain boundaries. Part (b) is the region enclosed by the white outline in part (a).

The microstructures of sputtered Ni-W films was previously reported by Borgia et al. [112]. They characterized as-sputtered and annealed films that spanned across the entire phase diagram. The alloys that were between 25-75 at.% W and annealed at 527 °C for 1 hr exhibited high thermal stability; they coarsened from 5-10 nm in diameter to 15-25 nm in diameter after annealing. Several phases were also identified, including Ni(W), Ni_4W, Ni_6W_6C, and pure W. The author's identification and labeling of Ni_6W_6C was discussed in section §6.3. However, the authors noted the larger Ni_6W_6C grains often had a "freckled" appearance. The work of this thesis strongly suggests that the freckles are WOx particles, considering the WOx particles were found in the Ni_6W_6C grains in the sputtered, electrodeposited, and mechanically alloyed samples (see section §7.2). Therefore, both carbon-and oxygen-rich impurity phases in sputtered Ni-W films have been identified elsewhere, and it is likely that these impurity phases are more common than currently realized. Furthermore, the thermal stability mechanisms that are truly limiting grain growth may also be different than currently acknowledged.

7.1.2 Influence of Sputtering Conditions on Grain Growth Behavior

As discussed in section §2.5, sputtered alloys can have a wide range of residual stress depending on the deposition parameters. Therefore, several 7 at.% W films were sputtered using different deposition parameters to gauge difference in grain growth behavior. All deposition parameters were kept constant according to

Table 4.3 unless stated otherwise. The most dramatic differences in microstructure are shown in Figure 7.3 and the corresponding SAD patterns are shown in the insets. Figure 7.3a shows a -50 V bias as-deposited film that was dense with high texture and large ~50 nm grains. Next, Figure 7.3b shows a 50 W and -150 V bias as-deposited film that did not exhibit high texture but did exhibit moderate porosity and ~25 nm grains. Lastly, Figure 7.3c shows a 30 mTorr and -150 V bias as-deposited film exhibited high porosity, no texture, and small ~10 nm grains. All of these different as-deposited microstructure may influence the material behavior, especially grain growth.

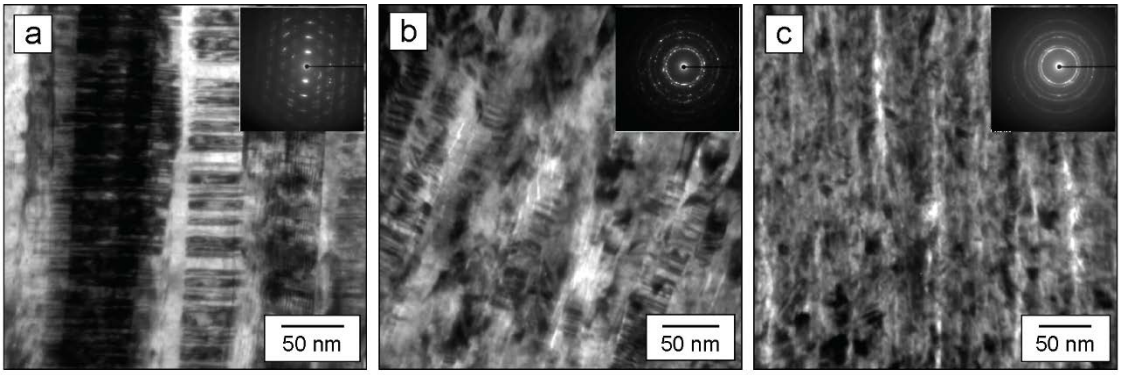

Figure 7.3. As-deposited sputtered alloys and electron diffraction patterns with slight differences in sputtering parameters: (a) -50 V bias, (b) 50 W and -150 V bias, and (c) 30 mTorr and -150 V bias films.

The influence of sputtering parameters on grain growth was investigated. Figure 7.4 shows three alloys of different sputtering parameters before and after annealing at 700 °C for 4 hrs in N_2-5%H_2. Most importantly, the as-deposited alloys were similar; all three exhibited ~50 nm columnar grains and strong texture. However, after annealing, the film that was deposited with -150 V substrate bias and 2 mTorr exhibited significantly more grain growth. The entire TEM sample was composed of a single grain, evidenced by the whole sample being highlighted in the DF condition, whereas the other two alloys had at least 100 grains. Again, all three films are the same composition and annealed simultaneously in the furnace. Therefore, the differences in grain size are due to the differences in deposition parameters.

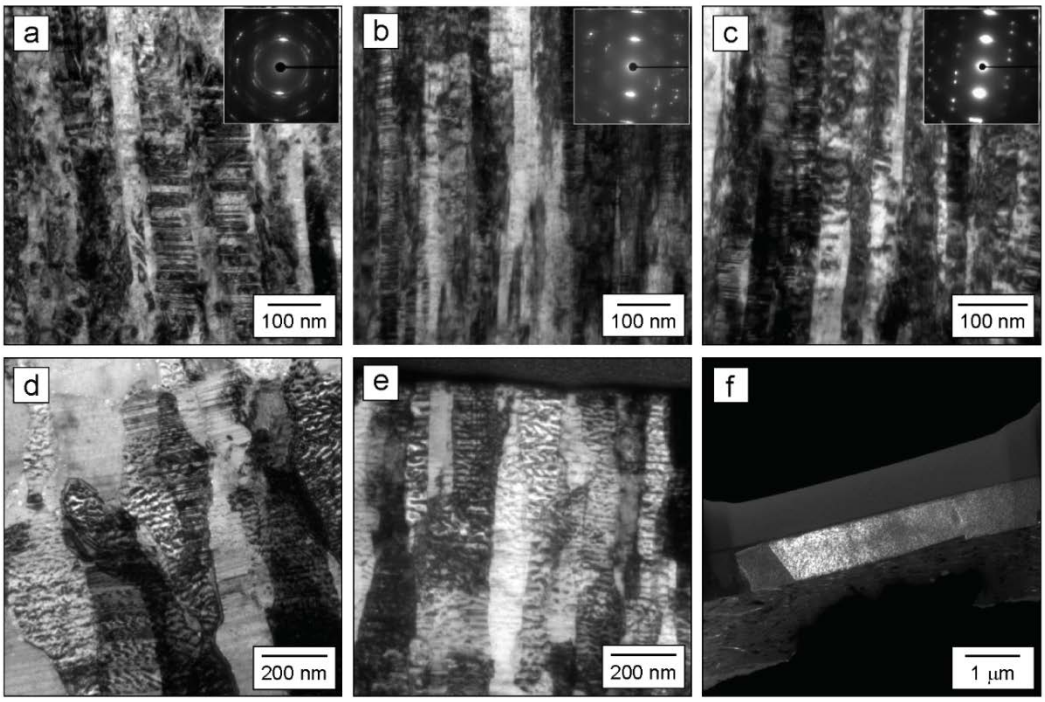

Figure 7.4. TEM images comparing the as-deposited and annealed microstructures of three Ni-7 at.% W films that were sputtered with different conditions: (a,d) No substrate bias and 5 mTorr; (b,e) -50 V substrate bias and 5 mTorr; and (c,f) -150V substrate bias and 2 mTorr. Images (a,b,c,d,e) are TEM-BF images and part (f) is a TEM-DF image.

It is hypothesized that the large difference in grain size between the alloys of Figure 7.4e and Figure 7.4f is due to differences in residual stress. Considering that lower sputtering pressures and stronger substrate bias both induce compressive stresses, the combination of the lowest pressure and most negative bias voltages will likely induce the highest level of stress, and therefore the highest amount of grain growth [60,61]. This scenario was confirmed as the 2 mTorr (lowest pressure) and -150 V bias (strongest bias) alloy did in fact exhibit the largest amount of grain growth. Again, the difference in grain growth is likely from differences in residual stress because the composition was the same and all other sputtering parameters were constant. Future experiments to confirm the hypothesis that residual stress is critical to nanocrystalline grain growth are strongly recommended. Overall, when considering nanocrystalline thermal stability, it is also important to consider residual stress from processing in addition to the alloy composition and purity.

7.2 Mechanically Alloyed Ni-W

Mechanically alloyed samples were fabricated by Kris Darling and Chad Hornbuckle from the Army Research Laboratory. They provided 1 at.% W, 5 at.% W, 15 at.% W, and 28 at.% W alloys that were annealed at 437 °C, 728 °C, and 1019 °C for 24 hrs in N_2-5%H_2. There were two main objectives regarding the mechanically alloyed samples: (1) compare microstructural evolution and impurity levels of mechanically alloyed samples to the Lehigh electrodeposited and sputtered alloys, and (2) investigate any potential differences in thermal stability mechanisms.

7.2.1 Overview of Mechanically Alloyed Alloys

Figure 7.5 compares each alloy after annealing at 728 °C. The grain size decreased with increasing W-concentration, and the 1 at.% W and 5 at.% W alloys were entirely comprised of Ni(W). The 15 at.% W and 28 at.% W alloys still had some undissolved W particles. The undissolved W particles exhibited a lamellar morphology that is consistent with ball milled alloys that are not sufficiently mixed [137]. The 15 at.% W and 28 at.% W alloys also exhibited Ni_6W_6C and Ni_4W. The presence of Ni_6W_6C and Ni_4W in the 15 at.% W is inconsistent with the electrodeposited alloys that did not exhibit the W-rich phases. Lastly, Table 7.1 summarizes the lattice parameters of each alloy after annealing at 728 °C. The lattice parameter increased between the 1 at.% W, 5 at.% W, and 15 at.% W alloys, but the 15 and 28 at.% W alloys were very similar. Thus, the maximum solute concentration in the Ni(W) grains was reached in the 15 at.% W alloy. The remaining W concentration was found in relatively higher volume fractions of pure W and Ni_6W_6C.

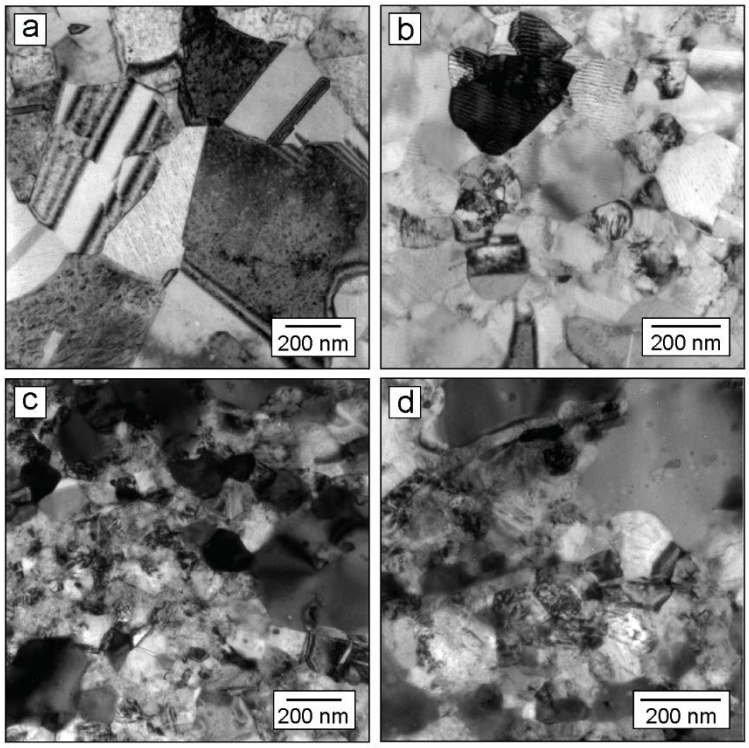

Figure 7.5. TEM-BF images of the mechanically alloyed samples after annealing at 728 C for 24 hrs: (a) 1 at.% W, (b) 5 at.% W, (c) 15 at.% W, and (d) 28 at.% W.

Table 7.1. Lattice parameter measurements of the four mechanically alloyed samples after annealing at 728 °C.

Alloy Composition	**Lattice Parameter**
1 at.% W	3.530 ± 0.020 Å
5 at.% W	3.561 ± 0.024 Å
15 at.% W	3.609 ± 0.028 Å
28 at.% W	3.612 ± 0.037 Å

The mechanically alloyed samples contained more contamination than the sputtered and "clean" electrodeposited alloys. All four of the 728 °C alloys exhibited Cr-rich oxide particles. The oxide compositions were again confirmed with STEM-EDS. The source of Cr is from the stainless steel milling container and milling balls, and the oxygen is from surface oxide layers that are present on the metallic powders during the start of milling. Contamination from milling media is common with mechanical alloying, and it

has been shown that up to 25 at.% W Fe can be incorporated into an initial Ni-33 at.% W alloy after milling for 20 hrs [68]. Figure 7.6a shows the oxide particle distribution in the 728 °C alloy where the oxide particles were observed in the Ni(W) matrix and within the Ni_6W_6C grains. Contrary to the UCSD alloys, the oxide particles are not predominantly located on the grain boundaries and triple points, and therefore are unlikely to be limiting grain growth. Despite the difference in oxide composition, the oxide particles still exhibited W-segregation to the phase boundaries between the oxides and Ni(W) matrix. Interestingly, W-segregation surrounds both large Cr-rich particles (Figure 7.6b), and small, faceted oxide particles which are embedded the center of the Ni(W) grains (Figure 7.6c).

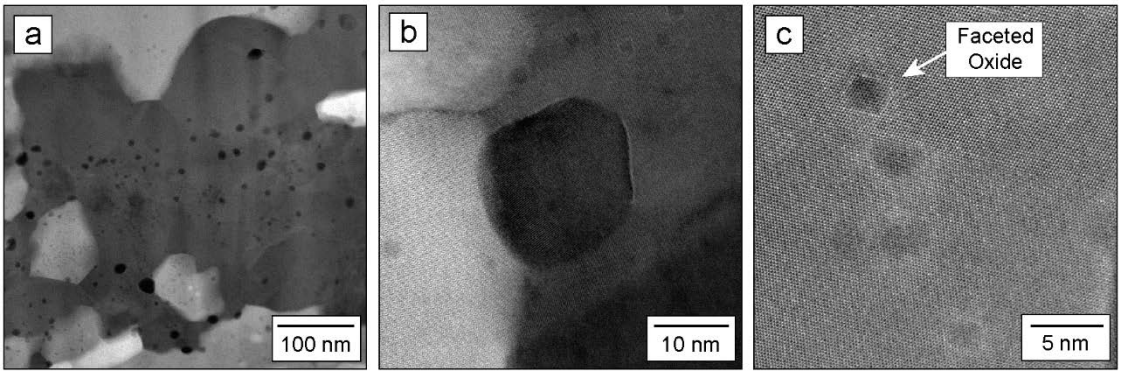

Figure 7.6. STEM-HAADF images of (a) the Cr-rich oxide distribution in the 728 °C alloy, and W-segregation observed at (a) large and (b) small, faceted Cr-rich oxide particles

The 28 at.% W alloy was also characterized at 437 °C and 1019 °C to track the microstructural evolution at different temperatures. The 28 at.% W alloy was chosen because of the complexity in phase stability and thermal stability mechanisms. Low magnification STEM-HAADF images in Figure 7.7 compare the microstructures. Interestingly, the only temperature that contained Ni_6W_6C was 728 °C. It is possible that either there was not enough thermal energy to precipitate Ni_6W_6C or it is

thermodynamically unstable at 437 °C. The lack of Ni_6W_6C at 1019 °C is consistent with the electrodeposited alloys produced at Lehigh that were also annealed for 24 hrs in N_2-5%H_2. Furthermore, at 437 °C and 728 °C, the W particles exhibited a lamellar morphology. It is possible that more milling time would have more effectively dissolved the W particles into the Ni(W) grain, but contamination would increase [68]. Rane *et al.* investigated the effect of milling time on mechanically alloyed Ni-W using planetary and shaker mills [67]. They showed that 20 hrs of shaker milling, similar to the milling apparatus employed for this thesis, did not completely dissolve W in a 15 at.% W alloy. However, a total time of 30 hrs more effectively dissolved the W. Since there is roughly twice as much W in the alloys studied here, it is further evidence that 4 hrs may not be enough milling time.

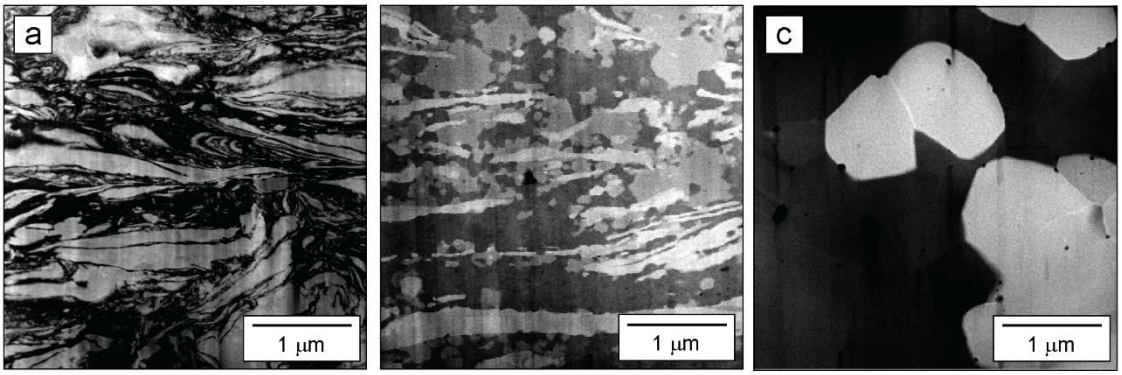

Figure 7.7. STEM-HAADF images of the mechanically alloyed 28at% alloy annealed at (a) 437 °C, (b) 728 °C, and (c) 1019 °C for 24 hrs in N2-5%H2

7.2.2 Evidence of W-segregation

The 437 °C alloy exhibited a higher amorphous content than the higher annealing temperatures. Amorphization with increasing milling energy or time is common in mechanically alloyed samples [138], and annealing at 437 °C did not fully crystallize the

microstructure. The amorphous regions were mostly located in-between Ni(W) grains. The intergranular width in this alloy is roughly 1-2 nm wide, but more conventional grain boundaries are typically ~0.5 nm. Thus, the interfaces between the Ni(W) grains will not be called grain boundaries, but intergranular regions.

The amorphous regions were determined to be W-rich. Figure 7.8a shows a STEM-HAADF image where the perimeter of several Ni(W) grains are higher intensity than the grain interiors, which again suggests that the amorphous region has a higher average atomic number than the matrix (*i.e.* there is more W). The STEM-BF image in Figure 7.8b more easily shows the Ni(W) grains to locate the grain boundaries. Figure 7.9 confirms the W-rich composition with a STEM-EDS map of the ratio of W to Ni X-rays counts. The ratio of W to Ni is used to account for any differences is thickness on grain boundaries that may occur during the thinning process. The W concentration on the grain boundaries and Ni(W) lattice were quantified using the Cliff-Lorimer equation [96], and it was determined that the boundaries and lattice were 12.2 ± 0.8 at.% W and 7.4 ± 0.6 at.% W, respectively. Both margins of error represent 95% certainty. Thus, there was an excess of ~4.8 at.% W on the grain boundaries. The average W concentration in the Ni(W) lattice is below the bulk concentration because W was also located in the Ni_6W_6C and pure W phases.

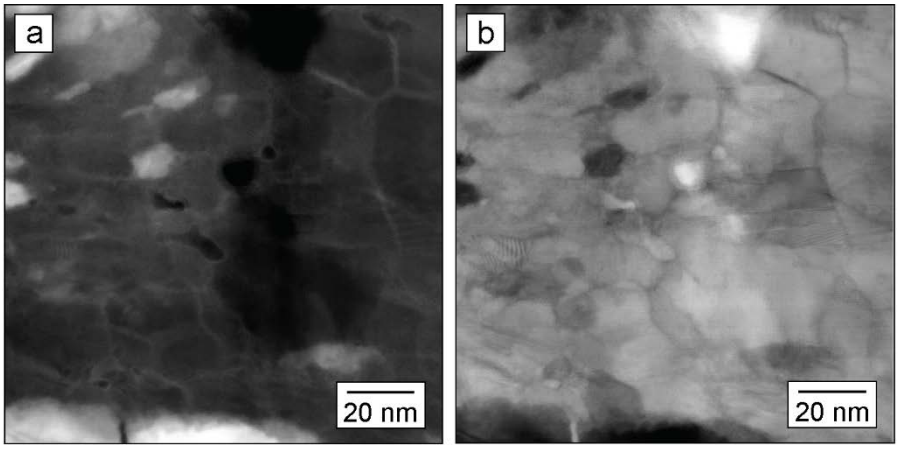

Figure 7.8. (a) STEM-HAADF and (b) STEM-BF images showing W-segregation in the 28 at.% W mechanically alloyed sample annealed at 437 °C.

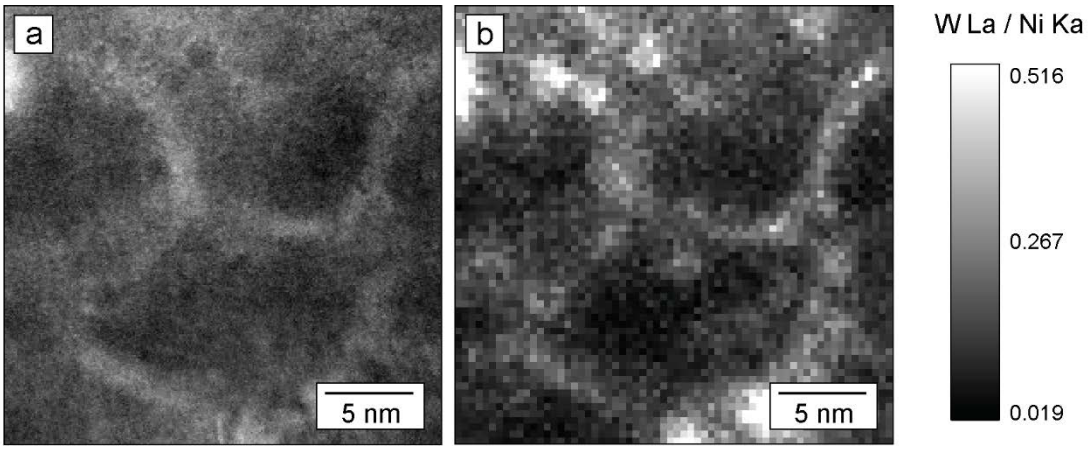

Figure 7.9. (a) STEM-HAADF image and (b) W Lα / Ni Kα STEM-EDS map validating W-segregation to mechanically alloyed 28 at.% W sample after annealing at 437 °C.

There are two explanations for the W-enrichment on the intergranular regions: (1) the Ni(W) grain nuclei are Ni-rich during crystallization and W is rejected from the grain, or (2) the W segregates to the boundaries according to the thermodynamic stabilization mechanism. Based on the microstructural evolution, it is more likely that scenario (1) occurred. Crystallization can be defined as phase separation, and when the two phases consist of different compositions, there will be a difference in compositions between the

two phases. Also, considering that the intergranular regions are not typical grain boundaries, the reduction of grain boundary energy via solute segregation may not be valid in these amorphous alloys.

The existence of crystalline and amorphous regions in Ni-W alloys has been reported elsewhere [78,139]. Kimoto *et al.* electrodeposited 17 at.% W alloys and characterized the as-deposited films using atom probe tomography [139]. Most importantly, they observed that the 37% of the film was crystalline and had a W concentration of 11 at.% W, and the amorphous phase was 63% of the film and had a W concentration of 18 at.% W. The authors used a combination of nano beam diffraction to determine the local structure of the crystalline and amorphous regions, and spot EDS analysis to determine the local composition. Two different nano-phases was also reported by Choi *et al.*, but in an annealed mechanically alloyed Ni-W sample [78]. Their atom probe tomography studies further confirmed that Ni-W alloys with nanoscale grain sizes should be considered duplex alloys that have both amorphous and crystalline regions. Again, if this is true, the thermodynamic mechanism of W-segregation to Ni(W) grain boundaries may not be valid considering the intergranular regions are amorphous and not structural grain boundaries that are assumed in those calculations.

If W is incorporated into the Ni(W) grains at higher temperatures, meaning the intergranular regions are no longer W-enriched, the lattice parameter should increase. Table 7.2 summarizes the lattice parameters of each alloy determined from the SAD patterns. The lattice expanded 0.068 Å between annealing at 437 °C and 728 °C. Thus, it is confirmed that the lattice contained less W in the Ni(W) solid solution at 437 °C, but

more W at 728 °C. The lattice slightly contracted after 1019 °C which suggests that the solubility limit was reached after annealing at 728 °C.

Table 7.2. Lattice parameter measurements of 28at% mechanically alloyed samples after annealing at 437 °C, 728 °C, and 1019 °C.

Annealing Temperature	**Lattice Parameter**
437 °C	3.544 ± 0.017 Å
728 °C	3.612 ± 0.037 Å
1019 °C	3.600 ± 0.045 Å

7.2.3 Ni_4W Long-range Ordering

Long-range Ni_4W ordering was observed in the 28 at.% W alloy at 728 °C, as well as the disordering transition above 1019 °C. Micrographs showing the ordered and disordered lattices on the Ni(W) [100] crystal direction are shown in Figure 7.10. The FFTs shown in the insets of Figure 7.10 confirm that the lattice disordered. The FFT of the ordered Ni_4W seen at 728 °C shows well defined superlattice reflections inside of the Ni reflections that match diffraction patterns found in the literature [103], and while the FFT of the 1019 °C alloy still shows short-range ordering via the blurred superlattice reflections, the reflections are much less defined and thereby indicate long range order was lost.

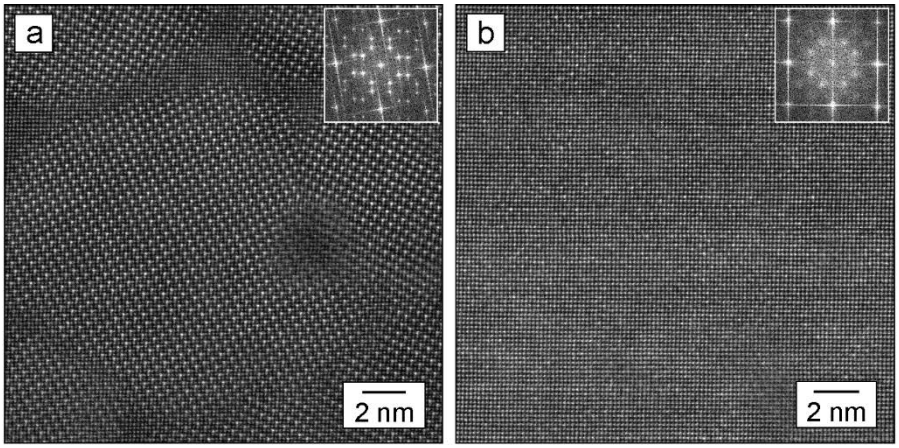

Figure 7.10. STEM-HAADF images and FFT insets showing the Ni_4W disordering transition between (a) 728 °C and (c) 1019 °C of the mechanically alloyed samples. Note: Part (a) was rotated and produced a different angle of the streaks in the FFT.

There are key differences between the Ni_4W domains in the mechanically alloyed specimen and the Ni_4W domains in the electrodeposited specimen. The mechanically alloyed Ni_4W still exhibited multiple domains within a single Ni(W) grain, but the Ni_4W found in the electrodeposited alloys, shown in Figure 5.21, exhibited a higher degree of long range order where the entire grain was Ni_4W. Furthermore, the mechanically alloyed Ni_4W exhibited 1-2 nm wide crystalline regions between the Ni_4W domains. Figure 7.11 shows the crystalline films at higher magnifications, and Figure 7.11b is a further enlargement of Figure 7.11a. The darker average intensity of the STEM-HAADF images within the 1-2 nm regions between the domains suggest that they are deficient in W. The regions are also the same intensity of the Ni atomic columns within the domains. X-ray EDS maps would determine if the inter-domain regions are Ni-rich.

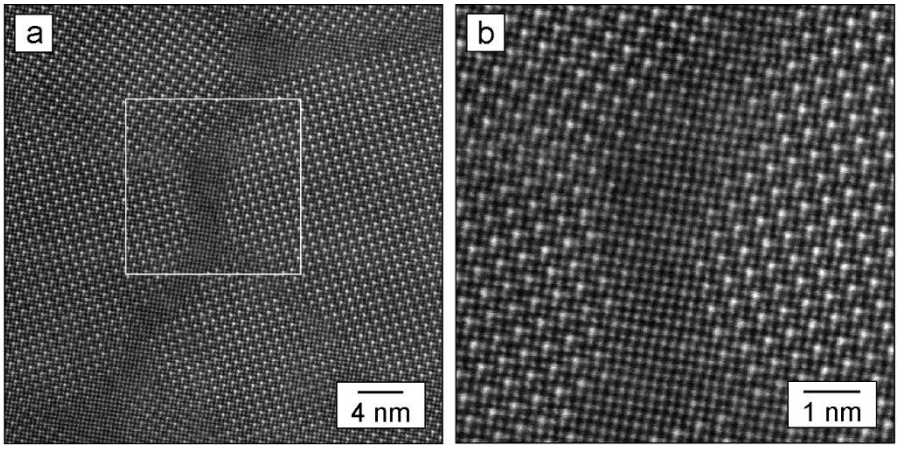

Figure 7.11. STEM-HAADF images showing the crystalline intergranular regions found in the 728 mechanically alloyed specimen. Part (b) is a magnified view of the white outline seen in part (a).

As previously mentioned, the electrodeposited specimen did exhibited a large and continuous domain after annealing for 24 hrs contrary to the nanoscale domains of the mechanically alloyed specimen. Therefore, the domain growth of the mechanically alloyed specimens was clearly different. It is possible that the mechanically alloyed sample underwent more crystallization or recovery because of the highly destructive ball milling and there was less time for the domains to coarsen. Consequently, it also possible to speculate that the Ni(W) grain growth behavior is different between the electrodeposited and mechanically alloyed samples. If the mechanically alloyed domains were smaller throughout the same time scale as the electrodeposited alloys, the domains could have been more effective pinning agents during Ni(W) grain growth, similar to the Ni_4W domains found in the 4 hr electrodeposited samples. If this is true, it is possible that Ni_4W ordering may not be as large of a hindrance when compared to Ni_4W domains that span the entire grain. On the other hand, the lattice and grain boundary mobilities may be lower if the entire grain was a single Ni_4W domain, which would similarly decrease the grain growth

rate. More detailed temperature – time studies are needed to track the domain growth in both alloys to estimate their true effect on grain growth behavior.

7.3 Direct Processing Comparison

The bulk fabrication process has been shown to influence the microstructural evolution and thermal stability mechanisms of various Ni-W alloys. When comparing alloys of the same composition, the mechanically alloyed specimens exhibited smaller average grain sizes than the sputtered and electrodeposited alloys at the same temperatures. The highly destructive ball milling process possibly required additional thermal energy to recover the microstructure, and therefore led to less time for grain growth. The amount of residual stress within each sample was also shown to be important. Sputtered alloys with the same composition but different sputtering parameters exhibited dramatically different grain growth rates, all because of difference in residual stress. The residual stress was not measured in the electrodeposited and mechanically alloyed samples, but it does not appear to be as influential as the sputtered alloys. In addition, the relative extent of contamination was different, where the mechanically alloyed samples exhibited high amounts of carbon and oxygen impurities. Similarly, the contaminated electrodeposited alloys similarly showed large volumes of nanoscale oxide particles. The difference here is that the W-rich oxide particles in the electrodeposited alloy limited grain growth but the Cr-rich oxides in the mechanically alloyed specimen did not limit grain growth. Overall, it is clear that there are other characteristics of nanocrystalline materials that must be considered when determining the most prominent thermal stability mechanisms, not just the composition.

7.4 Chapter Summary

This chapter identified differences of thermal stability mechanisms and phase stability between Ni-W alloys produced by electrodeposition, DC magnetron sputtering, and mechanical alloying. Overall, this new understanding will aide in controlling the microstructures of Ni-W to design the most thermally resistant materials. The significant findings are listed below:

1. The sputtering parameters greatly influenced as-deposited films that have the same composition. High working gas pressures (30 mTorr) produced small grains, no texture, and high porosity. Low gun powers similarly produce small grains and no texture, but with less porosity. Lastly, stronger substrate biases produced dense films with high texture.
2. Three 7 at.% W alloys with similar as-deposited microstructures exhibited dramatically different grain growth behaviors. The large difference was attributed to differences in residual stress.
3. The 24 at.% W sputtered alloys exhibited large (~10 nm) and nanoscale (~2 nm) Ar pores, and WOx and Ni_6W_6C similar to the electrodeposited and mechanically alloyed samples.
4. The average grain size of the mechanically alloyed samples decreased with increasing W concentration up to 15 at.% W. Furthermore, the 1 and 5 at.% W alloys exhibited a single phase Ni(W) microstructure (with a few Cr-rich oxide particles), and the 15 and 28 at.% W alloys exhibited Ni(W), pure W, Ni_4W, Ni_6W_6C, and Cr-rich oxide particles.

5. The Cr-rich oxide particles did not limit grain growth, contrary to the W-rich oxide particles found in the highly contaminated electrodeposited alloys.
6. Ni_4W long-range ordering was observed in the 28 at.% W alloy after annealing at 728 °C, but the average domain size was significantly less than the average domain size of the 21 at.% W electrodeposited alloy after annealing at 728 °C. Furthermore, crystalline regions ranging 1-2 nm in width were observed between the Ni_4W domains.
7. W-enrichment of 4.5 at.% W was quantified in the intergranular regions in the 28 at.% W alloy that was annealed at 437 °C. This enrichment was not grain boundary segregation in the classical sense, but a result of phase separation during crystallization.

Chapter 8 Conclusions

The main objectives of this thesis were to identify potential thermal stability mechanisms of Ni-W, re-evaluate Ni-W and Ni-W-C phase stability, and link differences in processing of electrodeposited, sputtered, and mechanically alloyed samples to nanocrystalline grain growth behavior. To accomplish these goals, aberration-corrected STEM was applied to study the physical nature of grain growth on the atomic-scale. Overall, this thesis has identified several potential thermal stability mechanisms and exposed the strong influence of oxygen and carbon contamination on the stability of Ni-W alloys. The most substantial findings are listed below:

1. Increasing W concentration decreased the grain size across all electrodeposited, sputtered, and mechanically alloyed sample sets. Most alloys were unstable after annealing and did not exhibit grains less than 100 nm above 728 °C. The only exceptions were 28 at.% W mechanically alloyed samples, and 23 at.% W electrodeposited alloys that had contained high oxygen contamination, and the 24 at.% W sputtered alloys.
2. Several thermal stability mechanisms were identified, including W-segregation, long-range Ni_4W chemical ordering, reduced atomic diffusivity, and nanoscale particle drag. However, the dominant thermal stability mechanisms were not identified. Individual stability mechanisms were not isolated in the annealing experiments and it was not possible to separate the individual contributions of each mechanism.

3. Strong evidence was presented that indicate nanoscale oxide particle drag was the dominant stability mechanism in the heavily contaminated electrodeposited alloys. Furthermore, W-segregation to the phase boundaries theoretically improved the coarsening resistance of the particles.
4. Long-range Ni_4W chemical ordering was imaged on the atomic scale for the first time to the author's knowledge. Furthermore, it was shown that some Ni_4W domains are located on the grain boundaries to reduce grain boundary diffusivity and enhance thermal stability. Furthermore, DFT results indicated that Ni_4W nucleation on a $\Sigma 5$ grain boundary is more energetically favorable than the bulk. DFT further determined that Ni_4W bi- and quad-layers reduce the Ni(W)-Ni_4W grain boundary energy, thereby augmenting the thermal stability.
5. Carbon and oxygen heavily influence the phase stability and thermal stability mechanisms of nanocrystalline Ni-W. DFT results have shown the intermetallics NiW and NiW_2 are thermodynamically stable in the ground-state. Furthermore, DFT has shown that the ternary carbides Ni_6W_6C and Ni_2W_4C are stable. Thus, new Ni-W-C ternary phase diagrams were constructed to more accurately portray this material system. The DFT ternary phase diagrams matched experimental results that observed Ni_4W, pure W, and Ni_6W_6C at 700 °C in >20 at.% W alloys.
6. The DC magnetron sputtering parameters influenced the grain growth behavior of 7 at.% W alloys. Three alloys exhibited similar as-deposited microstructures, but after annealing at 700 °C, dramatically different grain sizes were produced. The microstructure with the largest grain size likely had the largest residual stresses.

These results suggest that residual stress from processing is just as important as the alloy composition.

7. The mechanically alloyed specimens exhibited W-enrichment to the amorphous Ni(W) intergranular regions at 437 °C. The W-enrichment was caused by phase separation during crystallization and not solute segregation to crystalline grain boundaries in the classical sense.
8. The “clean” electrodeposited alloys have been shown to have the least amount of impurity phases compared to sputtering and mechanical alloying. The only identified impurity phase in the electrodeposited alloys was Ni_6W_6C, whereas the sputtered alloys exhibited W-rich oxides, Ar pores, and Ni_6W_6C, and the mechanically alloyed samples exhibited Cr-rich oxides and Ni_6W_6C.

Chapter 9 Future Work

The preceding chapters did not unequivocally determine which stability mechanisms are active at any given temperature or time, nor if the dominant stability mechanism changed at discrete temperatures. Samples were analyzed after annealing at only three temperatures, and there are gaps that span hundreds of degrees where the grain growth behavior is unknown. For example, the large jump in grain size between 437 °C and 728 °C in the electrodeposited alloys could have abruptly taken place (i.e. the grains coarsened very fast up to or at a specific temperature) or the grain size could have continuously increased at a constant rate. Considering the high W alloys that had Ni_4W ordering, it is possible that there was significant grain growth until Ni_4W precipitated, or it is also possible the grains coarsened at a constant rate regardless of Ni_4W precipitation. The methods used in this thesis were not able to determine the temporal effect of Ni_4W ordering. Overall, a continuous method that tracks microstructural evolution is needed.

One promising method to track microstructural evolution is differential scanning calorimetry (DSC). DSC measures differences in heat output between a sample and a reference gas, and can detect exothermic or endothermic processes at elevated temperatures. DSC can also be operated under isothermal or isochronal conditions to evaluate the change in microstructure as a function of time or temperature, respectively. With regard to nanocrystalline materials, DSC can detect the onset temperature or time in which grain growth or secondary phase precipitation begins. Both grain growth and phase precipitation are exothermic, so there should be a change in heat output at the start of each process. DSC has been successfully utilized with nanocrystalline Cu-Ta and the analysis

provided a wealth of information [47]. If DSC was applied to the Ni_4W example presented above, it could identify the onset of Ni_4W disordering. Once this temperature or time was known, samples could be annealed surrounding the Ni_4W disordering transition and analyzed with STEM to confidently determine if Ni_4W disordering changed the grain growth rate. DSC can similarly be applied to the precipitation of other secondary phases, including WOx, pure W, or Ni_6W_6C, to elucidate their role on thermal stability. Lastly, DSC also has the capability determine the crystallization temperature of amorphous alloys, which would be useful to track the grain growth behavior of the electrodeposited and mechanically alloyed samples that have a W concentration above ~20 at.% W.

Isothermal heat treatments should also be conducted to acquire grain growth rates over time. The isochronal heat treatments used in this thesis were valuable to find the maximum stable temperature, but they did not deliver grain growth rate constants. It would be favorable to compare rate constants derived from isothermal experiments of nanocrystalline Ni-W to rate constants of pure materials, or other material systems where the thermal stability mechanism and corresponding rate constants are known. Theoretically, activation energies of different stability mechanisms could also be derived, and this knowledge would greatly improve our understanding of nanocrystalline grain growth.

Solute segregation has been discussed several times throughout this work, but there are still many unanswered questions. First and foremost, more grain boundaries must be analyzed to gather more statistically grounded conclusions. Analyzing grain boundaries on the atomic scale is a time intensive process and few grain boundaries were analyzed

throughout this research. Furthermore, STEM was not able to quantify impurity carbon or oxygen segregation. To better analyze the segregation tendency of light elements, atom probe tomography is a promising technique. Choi *et al.* used atom probe to detect carbon segregation in Ni-W [78]. If carbon or oxygen segregation was quantified, we could have made conclusions regarding the thermodynamics and kinetics of Ni-W. For example, it was stated in section §2.3.1 that segregated impurity elements can affect the segregation tendency of W to the Ni grain boundaries. APT would also be able to reconstruct the three-dimensional volumes of the WOx particles to more accurately determine their volume fraction for particle drag calculations. The sample thickness determination technique used in section §5.4.2 to get the particle volume fraction required several simplifying assumptions, and it is desirable to obtain more realistic measurements.

References

[1] H. Gleiter, Nanocrystalline Materials, Prog. Mater. Sci. 33 (1990) 223–315.

[2] M.A. Meyers, A. Mishra, D.J. Benson, Mechanical Properties of Nanocrystalline Materials, Prog. Mater. Sci. 51 (2006) 427–556. doi:10.1016/j.pmatsci.2005.08.003.

[3] C. Suryanarayana, Nanocrystalline Materials, Int. Mater. Rev. 40 (1995) 41–64. doi:10.1179/095066095790151106.

[4] C.C. Koch, R.O. Scattergood, M. Saber, H. Kotan, High temperature stabilization of nanocrystalline grain size: Thermodynamic versus kinetic strategies, J. Mater. Res. 28 (2013) 1785–1791. doi:10.1557/jmr.2012.429.

[5] C.C. Koch, R.O. Scattergood, K.A. Darling, J.E. Semones, Stabilization of nanocrystalline grain sizes by solute additions, J. Mater. Sci. 43 (2008) 7264–7272. doi:10.1007/s10853-008-2870-0.

[6] R.A. Andrievski, Review of thermal stability of nanomaterials, J. Mater. Sci. 49 (2014) 1449–1460. doi:10.1007/s10853-013-7836-1.

[7] M. Saber, C.. Koch, R.. Scattergood, Thermodynamic Grain Size Stabilization Models : An Overview, Mater. Res. Lett. 3 (2015) 37–41. doi:10.1080/21663831.2014.997894.

[8] H. Gleiter, Materials with Ultrafine Microstructures: Retrospectives and Perspectives, Nanostructured Mater. 1 (1992) 1–19. doi:10.1016/0965-9773(92)90045-Y.

[9] C. Suryanarayana, C.C. Koch, Nanocrystalline Materials – Current Research and Future Directions, Hyperfine Interact. 130 (2000) 5–44.

[10] C.A. Schuh, T.G. Nieh, H. Iwasaki, The effect of solid solution W additions on the mechanical properties of nanocrystalline Ni, Acta Mater. 51 (2003) 431–443. doi:10.1016/S1359-6454(02)00427-5.

[11] S. Schumacher, R. Birringer, R. Straub, H. Gleiter, Diffusion of Silver in Nanocrystalline Copper Between 303 and 373K, Acta Metall. 37 (1989) 2485–2488.

[12] K. Tai, S.J. Dillon, Scaling effects on grain boundary diffusivity; Au in Cu, Acta Mater. 61 (2013) 1851–1861. doi:10.1016/j.actamat.2012.12.006.

[13] Y. Chen, C.A. Schuh, Contribution of triple junctions to the diffusion anomaly in nanocrystalline materials, Scr. Mater. 57 (2007) 253–256. doi:10.1016/j.scriptamat.2007.03.057.

[14] T. Rupert, W. Cai, C. Schuh, Abrasive wear response of nanocrystalline Ni–W alloys across the Hall–Petchbreakdown, Wear. 298-299 (2013) 120–126. doi:10.1016/j.wear.2013.01.021.

[15] T.J. Rupert, C.A. Schuh, Sliding wear of nanocrystalline Ni–W: Structural evolution and the apparent breakdown of Archard scaling, Acta Mater. 58 (2010) 4137–4148. doi:10.1016/j.actamat.2010.04.005.

[16] M. Pal, D. Chakravorty, Nanocrystalline magnetic alloys and ceramics, Sadhana. 28 (2003) 283–297. doi:10.1007/BF02717138.

[17] R. Mishra, R. Balasubramaniam, Effect of nanocrystalline grain size on the electrochemical and corrosion behavior of nickel, Corros. Sci. 46 (2004) 3019–3029. doi:10.1016/j.corsci.2004.04.007.

[18] M. Ames, J. Markmann, R. Karos, A. Michels, A. Tschöpe, R. Birringer, Unraveling the nature of room temperature grain growth in nanocrystalline materials, Acta Mater. 56 (2008) 4255–4266. doi:10.1016/j.actamat.2008.04.051.

[19] J.E. Burke, D. Turnbull, Recrystallization and grain growth, Prog. Met. Phys. 3 (1952) 220–292. doi:10.1016/0502-8205(52)90009-9.

[20] M. Hillert, On the theory of normal and abnormal grain growth, Acta Metall. 13 (1965) 227–238. doi:10.1017/CBO9781107415324.004.

[21] S.-J.L. Kang, Sintering: Densification, Grain Growth and Microstructure, Butterworth-Heinemann, 2004. https://books.google.com/books?hl=en&lr=&id=uPWbuZohRmoC&pgis=1 (accessed March 8, 2016).

[22] A.J. Haslam, S.R. Phillpot, D. Wolf, D. Moldovan, H. Gleiter, Mechanisms of grain growth in nanocrystalline fcc metals by molecular-dynamics simulation, 318 (2001) 293–312.

[23] D. Moldovan, V. Yamakov, D. Wolf, S.R. Phillpot, Scaling behavior of grain-rotation-induced grain growth., Phys. Rev. Lett. 89 (2002) 206101. doi:10.1103/PhysRevLett.89.206101.

[24] C.E. Krill, L. Helfen, D. Michels, H. Natter, A. Fitch, O. Masson, et al., Size-dependent grain-growth kinetics observed in nanocrystalline Fe, Phys. Rev. Lett. 86 (2001) 842–845. doi:10.1103/PhysRevLett.86.842.

[25] G.D. Hibbard, J.L. McCrea, G. Palumbo, K.T. Aust, U. Erb, An initial analysis of mechanisms leading to late stage abnormal grain growth in nanocrystalline Ni, Scr. Mater. 47 (2002) 83–87. doi:10.1016/S1359-6462(02)00098-2.

[26] S.J. Dillon, M. Tang, W.C. Carter, M.P. Harmer, Complexion: A New Concept for Kinetic Engineering in Materials Science, Acta Mater. 55 (2007) 6208–6218. doi:10.1016/j.actamat.2007.07.029.

[27] J. Weissmuller, Alloy Effects in Nanostructures, NanoStructured Mater. 3 (1993) 261.

[28] J. Weissmuller, Alloy Thermodynamics in Nanostructures, J. Mater. Res. 9 (1994) 4.

[29] F. Liu, R. Kirchheim, Grain boundary saturation and grain growth, Scr. Mater. 51 (2004) 521–525. doi:10.1016/j.scriptamat.2004.05.042.

[30] P. Wynblatt, R.C. Ku, Surface energy and solute strain energy effects in surface segregation, Surf. Sci. 65 (1977) 511–531. doi:10.1016/0039-6028(77)90462-9.

[31] M.A. Atwater, K.A. Darling, A Visual Library of Stability in Binary Metallic Systems : The Stabilization of Nanocrystalline Grain Size by Solute Addition : Part 1, 2012.

[32] J. Trelewicz, C.A. Schuh, Grain boundary segregation and thermodynamically stable binary nanocrystalline alloys, Phys. Rev. B. 79 (2009) 094112. doi:10.1103/PhysRevB.79.094112.

[33] H.A. Murdoch, C.A. Schuh, Stability of binary nanocrystalline alloys against grain growth and phase separation, Acta Mater. 61 (2013) 2121–2132. doi:10.1016/j.actamat.2012.12.033.

[34] H.A. Murdoch, C.A. Schuh, Estimation of grain boundary segregation enthalpy and its role in stable nanocrystalline alloy design, J. Mater. Res. 28 (2013) 2154–2163. doi:10.1557/jmr.2013.211.

[35] M. Saber, H. Kotan, C.C. Koch, R.O. Scattergood, Thermodynamic stabilization of nanocrystalline binary alloys, J. Appl. Phys. 113 (2013) 063515. doi:10.1063/1.4791704.

[36] M. Saber, H. Kotan, C.C. Koch, R.O. Scattergood, A predictive model for thermodynamic stability of grain size in nanocrystalline ternary alloys, J. Appl. Phys. 114 (2013). doi:10.1063/1.4821040.

[37] C.E. Krill, H. Ehrhardt, R. Birringer, Thermodynamic Stabilization of Nanocrystallinity, Z. Met. 96 (2005) 1134.

[38] B.K. VanLeeuwen, K.A. Darling, C.C. Koch, R.O. Scattergood, B.G. Butler, Thermal stability of nanocrystalline Pd81Zr19, Acta Mater. 58 (2010) 4292–4297. doi:10.1016/j.actamat.2010.04.023.

[39] K.A. Darling, B.K. VanLeeuwen, C.C. Koch, R.O. Scattergood, Thermal stability of nanocrystalline Fe–Zr alloys, Mater. Sci. Eng. A. 527 (2010) 3572–3580. doi:10.1016/j.msea.2010.02.043.

[40] J.W. Cahn, The impurity-drag effect in grain boundary motion, Acta Metall. 10 (1962) 789–798.

[41] M.A. Atwater, R.O. Scattergood, C.C. Koch, The stabilization of nanocrystalline copper by zirconium, Mater. Sci. Eng. A. 559 (2013) 250–256. doi:10.1016/j.msea.2012.08.092.

[42] C. Bansal, Z.Q. Gao, B. Fultz, Grain growth and chemical ordering in (Fe,Mn)3Si, Nanostructured Mater. 5 (1995) 327–336. doi:10.1016/0965-9773(95)00236-8.

[43] Z.Q. Gao, B. Fultz, The thermal stability of nanocrystalline Fe-Si-Nb prepared by

mechanical alloying, NanoStructured Mater. 2 (1993) 231–240. doi:10.1017/CBO9781107415324.004.

[44] Z.Q. Gao, B. Fultz, Inter-dependence of grain growth, Nb segregation, and chemical ordering in FeSiNb nanocrystals, Nanostructured Mater. 4 (1994) 939–947. doi:10.1016/0965-9773(94)90100-7.

[45] K. Boylan, D. Ostrander, U. Erb, G. Palumbo, K.T. Aust, An in-situ tem study of the thermal stability of nanocrystalline NiP, Scr. Metall. Mater. 25 (1991) 2711–2716. doi:10.1016/0956-716X(91)90144-P.

[46] B. Färber, E. Cadel, a. Menand, G. Schmitz, R. Kirchheim, Phosphorus segregation in nanocrystalline Ni-3.6 at.% P alloy investigated with the tomographic atom probe (TAP), Acta Mater. 48 (2000) 789–796. doi:10.1016/S1359-6454(99)00397-3.

[47] K.A. Darling, A.J. Roberts, Y. Mishin, S.N. Mathaudhu, L.J. Kecskes, Grain size stabilization of nanocrystalline copper at high temperatures by alloying with tantalum, J. Alloys Compd. 573 (2013) 142–150. doi:10.1016/j.jallcom.2013.03.177.

[48] T. Frolov, K.A. Darling, L.J. Kecskes, Y. Mishin, Stabilization and strengthening of nanocrystalline copper by alloying with tantalum, Acta Mater. 60 (2012) 2158–2168. doi:10.1016/j.actamat.2012.01.011.

[49] H. Natter, R. Hempelmann, Tailor-made nanomaterials designed by electrochemical methods, Electrochim. Acta. 49 (2003) 51–61. doi:10.1016/j.electacta.2003.04.004.

[50] C. Savall, a. Godon, J. Creus, X. Feaugas, Influence of deposition parameters on microstructure and contamination of electrodeposited nickel coatings from additive-free sulphamate bath, Surf. Coatings Technol. 206 (2012) 4394–4402. doi:10.1016/j.surfcoat.2012.04.068.

[51] N. Eliaz, T.M. Sridhar, E. Gileadi, Synthesis and characterization of nickel tungsten alloys by electrodeposition, Electrochim. Acta. 50 (2005) 2893–2904. doi:10.1016/j.electacta.2004.11.038.

[52] A. Godon, J. Creus, X. Feaugas, E. Conforto, L. Pichon, C. Armand, et al., Characterization of electrodeposited nickel coatings from sulphamate electrolyte without additive, Mater. Charact. 62 (2011) 164–173. doi:10.1016/j.matchar.2010.11.011.

[53] I. Matsui, T. Uesugi, Y. Takigawa, K. Higashi, Effect of interstitial carbon on the mechanical properties of electrodeposited bulk nanocrystalline Ni, Acta Mater. 61 (2013) 3360–3369. doi:10.1016/j.actamat.2013.02.025.

[54] M.D. Obradović, R.M. Stevanović, a. R. Despić, Electrochemical deposition of Ni–W alloys from ammonia–citrate electrolyte, J. Electroanal. Chem. 552 (2003) 185–196. doi:10.1016/S0022-0728(03)00151-7.

[55] N. Shakibi Nia, J. Creus, X. Feaugas, C. Savall, The effect of tungsten addition on metallurgical state and solute content in nanocrystalline electrodeposited nickel, J. Alloys Compd. 609 (2014) 296–301. doi:10.1016/j.jallcom.2014.04.192.

[56] O. Younes, E. Gileadi, Electroplating of Ni/W Alloys, J. Electrochem. Soc. 149 (2002) C100. doi:10.1149/1.1433750.

[57] A.J. Detor, C.A. Schuh, Tailoring and Patterning the Grain Size of Nanocrystalline Alloys, Acta Mater. 55 (2007) 371–379. doi:10.1016/j.actamat.2006.08.032.

[58] K.P. Almtoft, Structural Characterization of Nanocrystalline Thin Films Grown by Magnetron Sputtering, University of Aarhus, 2006.

[59] N. Radic, P. Dubcek, S. Bernstorff, I. Djerdj, a. M. Tonejc, Structural study of nanocrystalline nickel thin films, J. Appl. Crystallogr. 40 (2007) s377–s382. doi:10.1107/S0021889807004682.

[60] Y.G. Shen, Y.W. Mai, Q.C. Zhang, D.R. McKenzie, W.D. McFall, W.E. McBride, Residual stress, microstructure, and structure of tungsten thin films deposited by magnetron sputtering, J. Appl. Phys. 87 (2000) 177. doi:10.1063/1.371841.

[61] A.J. Detor, A.M. Hodge, E. Chason, Y. Wang, H. Xu, M. Conyers, et al., Stress and microstructure evolution in thick sputtered films, Acta Mater. 57 (2009) 2055–2065. doi:10.1016/j.actamat.2008.12.042.

[62] C. Suryanarayana, Mechanical Alloying and Milling, Prog. Mater. Sci. 46 (2001) 1–184. doi:10.1016/S0079-6425(99)00010-9.

[63] C.C. Koch, Materials Synthesis by Mechanical Alloying, Annu. Rev. Mater. Sci. 19 (1989) 121–143. doi:10.1146/annurev.ms.19.080189.001005.

[64] C. Suryanarayana, E. Ivanov, V.. Boldyrev, The Science and Technology of Mechanical Alloying, Mater. Sci. Eng. A. 304-306 (2001) 151–158. doi:10.1016/S0921-5093(00)01465-9.

[65] C. Suryanarayana, Recent Developments in Mechanical Alloying, Rev. Adv. Mater. Sci. 18 (2008) 203–211. http://www-proxy.ipme.ru/e-journals/RAMS/no_31808/suryanarayana.pdf.

[66] M. Tschopp, H. Murdoch, L. Kecskes, K. Darling, “Bulk” Nanocrystalline Metals: Review of the Current State of the Art and Future Opportunities for Copper and Copper Alloys, J. Mater. Sci. 66 (2014) 1000–1019. doi:10.1007/s11837-014-0978-z.

[67] G. Rane, D. Apel, U. Welzel, E. Mittemeijer, The microstructural evolution and thermal stability of nanocrystalline ball-milled Ni–15 at.% W powder, J. Mater. Res. 28 (2013) 873–886. doi:10.1557/jmr.2012.442.

[68] T. Courtney, Z. Wang, Grinding media wear during mechanical alloying of Ni-W alloys in a SPEX mill, Scr. Metall. Mater. 27 (1992) 777–782. doi:10.1016/0956-716X(92)90505-9.

[69] J. Eckert, J.C. Holzer, M. Li, W.L. Johnson, Effects of chemistry on the grain size refinement in nanocrystalline Ru and RuC powders prepared by mechanical attrition, Nanostructured Mater. 2 (1993) 433–439. doi:10.1016/0965-9773(93)90186-F.

[70] S. Saji, H. Yasuda, T. Yamane, Effects of the atmosphere on the mechanical alloying process of Al25at.%Ti mixed powder, Mater. Sci. Eng. A. 179-180 (1994) 676–680. doi:10.1016/0921-5093(94)90291-7.

[71] H. Okamoto, Ni-W (nickel-tungsten), J. Phase Equilibria. 12 (1991) 706. doi:10.1007/BF02645185.

[72] A. Detor, C. Schuh, Microstructural evolution during the heat treatment of nanocrystalline alloys, J. Mater. Res. 22 (2007) 3233–3248. doi:10.1557/JMR.2007.0403.

[73] A. Detor, M. Miller, C. Schuh, Solute distribution in nanocrystalline Ni–W alloys examined through atom probe tomography, Philos. Mag. 86 (2006) 4459–4475. doi:10.1080/14786430600726749.

[74] A.J. Detor, C.A. Schuh, Grain boundary segregation, chemical ordering and stability of nanocrystalline alloys: Atomistic computer simulations in the Ni–W system, Acta Mater. 55 (2007) 4221–4232. doi:10.1016/j.actamat.2007.03.024.

[75] A.J. Detor, M.K. Miller, C.A. Schuh, Measuring grain-boundary segregation in nanocrystalline alloys: direct validation of statistical techniques using atom probe tomography, Philos. Mag. Lett. 87 (2007) 581–587. doi:10.1080/09500830701400125.

[76] F. Liu, R. Kirchheim, Nano-scale grain growth inhibited by reducing grain boundary energy through solute segregation, J. Cryst. Growth. 264 (2004) 385–391. doi:10.1016/j.jcrysgro.2003.12.021.

[77] J. Weissmuller, W. Krauss, T. Haubold, R. Birringer, H. Gleiter, Atomic structure and thermal stability of nanostructured Y-Fe alloys, Nanostructured Mater. 1 (1992) 439–447. doi:10.1016/0965-9773(92)90076-A.

[78] P. Choi, F. Ga, H. Kreye, R. Kirchheim, Thermal Stability of Nanocrystalline Nickel-18at% Tungsten Alloy Investigated with the Tomographic Atom Probe, Mater. Sci. Eng. 353 (2003) 74–79.

[79] T. Yamasaki, R. Tomohira, Y. Ogino, P. SchloBmacher, K. Ehrlich, Formation of Ductile Amorphous and Nanocrystalline Ni-W Alloys by Electrodeposition, Plat. Surf. Finish. 87 (2000) 148–152.

[80] D. Tomus, H.P. Ng, In situ lift-out dedicated techniques using FIB-SEM system for TEM specimen preparation., Micron. 44 (2013) 115–9. doi:10.1016/j.micron.2012.05.006.

[81] M. Schaffer, B. Schaffer, Q. Ramasse, Sample preparation for atomic-resolution STEM at low voltages by FIB, Ultramicroscopy. 114 (2012) 62–71.

doi:10.1016/j.ultramic.2012.01.005.

[82] R.R. Cerchiara, P.E. Fischione, J. Liu, J.M. Matesa, a. C. Robins, H.L. Fraser, et al., Raising the Standard of Specimen Preparation for Aberration-Corrected TEM and STEM, Micros. Today. 19 (2011) 16–19. doi:10.1017/S1551929510001197.

[83] L.A. Giannuzzi, J.R. Michael, Comparison of Channeling Contrast between Ion and Electron Images, Microsc. Microanal. 19 (2013) 344–349. doi:10.1017/S1431927602010346.

[84] C.A. Volkert, A.M. Minor, Focused Ion Beam Microscopy and Micromachining, MRS Bull. 32 (2007) 389–399. doi:10.1557/mrs2007.62.

[85] D.R.G. Mitchell, DiffTools: Electron diffraction software tools for DigitalMicrograph???, Microsc. Res. Tech. 71 (2008) 588–593. doi:10.1002/jemt.20591.

[86] C.A. Schneider, W.S. Rasband, K.W. Eliceiri, NIH Image to ImageJ: 25 years of image analysis, Nat. Methods. 9 (2012) 671–675. doi:10.1038/nmeth.2089.

[87] W. Cao, C. Marvel, D. Yin, Y. Zhang, P. Cantwell, M.P. Harmer, et al., Correlations between microstructure, fracture morphology, and fracture toughness of nanocrystalline Ni–W alloys, Scr. Mater. 113 (2016) 84–88. doi:10.1016/j.scriptamat.2015.09.030.

[88] S. Ruan, C.A. Schuh, Mesoscale structure and segregation in electrodeposited nanocrystalline alloys, Scr. Mater. 59 (2008) 1218–1221. doi:10.1016/j.scriptamat.2008.08.010.

[89] K.T. Jacob, Phase relationships in the system Ni-W-O and thermodynamic properties of NiWO4, J. Mater. Sci. 12 (1977) 1647–1652. doi:10.1007/BF00542815.

[90] M.P. Seah, Grain boundary segregation, Met. Phys. 10 (1980) 1043–1064.

[91] Y.Y. Chuang, Y.A. Chang, R. Schmid, J.C. Lin, Magnetic contributions to the thermodynamic functions of alloys and the phase equilibria of Fe-Ni system below 1200 K, Metall. Trans. A. 17 (1986) 1361–1372. doi:10.1007/BF02650117.

[92] T. Hentschel, D. Isheim, R. Kirchheim, F. Muller, H. Kreye, Nanocrystalline Ni-3.6 at.% P and its Transformation Sequence Studied by Atom-Probe Field-Ion Microscopy, Acta Mater. 48 (2000) 933–941.

[93] V.J. Keast, D.B. Williams, Quantification of boundary segregation in the analytical electron microscope, J. Microsc. 199 (2000) 45–55.

[94] J.R. Michael, D.B. Williams, An Analytical Electron Microscope Study of the Kinetics of the Equilibrium Segregation of Bismuth in Copper, Metall. Trans. A. 15 (1984) 99–105.

[95] C.J. Marvel, D. Yin, P.R. Cantwell, M.P. Harmer, The influence of oxygen contamination on the thermal stability and hardness of nanocrystalline Ni–W

alloys, Mater. Sci. Eng. A. 664 (2016) 49–57. doi:10.1016/j.msea.2016.03.129.

[96] U. Alber, H. Mullejans, M. Ruhle, Improved quantification of grain boundary segregation by EDS in a dedicated STEM, Ultramicroscopy. 69 (1997) 105–116.

[97] R. Juškėnas, I. Valsiūnas, V. Pakštas, R. Giraitis, On the state of W in electrodeposited Ni–W alloys, Electrochim. Acta. 54 (2009) 2616–2620. doi:10.1016/j.electacta.2008.10.060.

[98] J. Sheng, G. Rane, U. Welzel, E.J. Mittemeijer, The lattice parameter of nanocrystalline Ni as function of crystallite size, Phys. E Low-Dimensional Syst. Nanostructures. 43 (2011) 1155–1161. doi:10.1016/j.physe.2011.01.029.

[99] G.K. Rane, U. Welzel, S.R. Meka, E.J. Mittemeijer, Non-monotonic lattice parameter variation with crystallite size in nanocrystalline solids, Acta Mater. 61 (2013) 4524–4533. doi:10.1016/j.actamat.2013.04.021.

[100] A.M. Engwall, Atomistic Computer Simulation Analysis of Nanocrystalline NiW Alloys, MIT, 2009.

[101] V.S. Sundaram, R.S. Alben, W.D. Robertson, THE ORDER-DISORDER TRANSFORMATION AT A (100) SURFACE OF Cu3Au Theory and Experiment, Surf. Sci. 46 (1974) 653–671.

[102] H. Dosch, H. Reichert, Ordering, disordering and segregation at binary interfaces: Model system Cu3Au(001), Acta Mater. 48 (2000) 4387–4393. doi:10.1016/S1359-6454(00)00225-1.

[103] N.S. Mishra, S. Ranganathan, Electron microscopy and diffraction of ordering in Ni4W alloys, Acta Metall. Mater. 43 (1995) 2287–2302. doi:10.1016/0956-7151(94)00417-X.

[104] N.S. Mishra, R. S., Electron Microscopy and Diffraction of Ordering in an Off-Stoichiometric Ni-W Alloy, Scr. Metall. 27 (1992) 1337–1342.

[105] K. Wakashima, K. Ishige, S. Umekawa, Mosaic structure formation due to oriented precipitation of Ni4W around W fibers in a Ni-W directionally solidified eutectic alloy, Acta Metall. 30 (1982) 1515–1522. doi:10.1016/0001-6160(82)90172-9.

[106] J. Williams, G. Garmong, Microstructural Studies of a Ni-W Directionally Solidified Eutectic Composite, Metall. Trans. A. 6 (1975) 1699.

[107] H. Zhao, G.C. Weatherly, THE FORMATION OF MULTI-DOMAIN IN A Ni-W ALLOY PRECIPITATES, Acta Metall. Mater. 38 (1990) 2253–2260.

[108] H. Zhaot, K.T. Aust, G.C. Weatherly, Morphological Development During Ageing of Ni-W Alloys, Acta Metall. Mater. 40 (1992) 1961–1968.

[109] T. Kingetsu, M. Yamamoto, S. Nenno, Ordering and Disordering Phenomena At/Near the Surface of D1a Type Ordering Alloys, J. Phys. Colloq. 48 (1987) 373/378.

[110] K. Momma, F. Izumi, VESTA 3 for three-dimensional visualization of crystal, volumetric and morphology data, J. Appl. Crystallogr. 44 (2011) 1272–1276. doi:10.1107/S0021889811038970.

[111] H.I. Aaronson, Mechanisms of the massive transformation, Metall. Mater. Trans. A. 33 (2002) 2285–2297. doi:10.1007/s11661-002-0352-6.

[112] C. Borgia, T. Scharowsky, A. Furrer, C. Solenthaler, R. Spolenak, A combinatorial study on the influence of elemental composition and heat treatment on the phase composition, microstructure and mechanical properties of Ni–W alloy thin films, Acta Mater. 59 (2011) 386–399. doi:10.1016/j.actamat.2010.09.045.

[113] J.C. Sabol, C.J. Marvel, M. Watanabe, T. Pasang, W.Z. Misiolek, Confirmation of the ω-phase in electron beam welded Ti–5Al–5V–5Mo–3Cr by high-resolution scanning transmission electron microscopy: An initial investigation into its effects on embrittlement, Scr. Mater. 92 (2014) 15–18. doi:10.1016/j.scriptamat.2014.08.003.

[114] V. Randle, B. Ralph, The influence of strong grain boundary pinning by particle upon boundary structure during post-recrystallisation anneals, J. Mater. Sci. 22 (1987) 2535–2541.

[115] S.P. Ringer, W.B. Li, K.E. Easterling, On the interaction and pinning of grain boundaries by cubic shaped precipitate particles, Acta Metall. 37 (1989) 831–841. doi:10.1016/0001-6160(89)90010-2.

[116] J. Zhou, S. Zhang, X. Wang, B. Zhao, X. Dong, L. Zhang, Interaction between coherent second-phase particles and migrating boundaries: Boundary effect and particle reorientation, Scr. Mater. 116 (2016) 100–103. doi:http://dx.doi.org/10.1016/j.scriptamat.2016.02.010.

[117] A.R. Wazzan, Lattice and grain boundary self-diffusion in nickel, J. Appl. Phys. 36 (1965) 3596–3599. doi:10.1063/1.1703047.

[118] J.O. Andersson, T. Helander, L. Hoglund, P. Shi, B. Sundman, THERMO-CALC & DICTRA, Computational Tools For Materials Science, Calphad. 26 (2002) 273–312. www.thermocalc.com.

[119] V.D. Divya, S.S.K. Balam, U. Ramamurty, A. Paul, Interdiffusion in the Ni-Mo system, Scr. Mater. 62 (2010) 621–624. doi:10.1016/j.scriptamat.2010.01.008.

[120] A.M. Brown, M.F. Ashby, Correlations for Diffusion Constants., Acta Metall. 28 (1980) 1085–1101. doi:10.1016/0001-6160(80)90092-9.

[121] D. Prokoshkina, V.A. Esin, G. Wilde, S.V. Divinski, Grain boundary width, energy and self-diffusion in nickel: Effect of material purity, Acta Mater. 61 (2013) 5188–5197. doi:10.1016/j.actamat.2013.05.010.

[122] J.M. Walsh, M.J. Donachie, Interdiffusion in the Nickel-Tungsten and Thoria-Dispersed Nickel-Tungsten Systems, Met. Sci. J. 3 (1969) 68–74.

[123] M.S.. Karunaratne, P. Carter, R.C. Reed, Interdiffusion in the face-centred cubic

phase of the Ni–Re, Ni–Ta and Ni–W systems between 900 and 1300°C, Mater. Sci. Eng. A. 281 (2000) 229–233. doi:10.1016/S0921-5093(99)00705-4.

[124] C. Chen, L. Zhang, J. Xin, Y. Wang, Y. Du, F. Luo, et al., Diffusivities and atomic mobilities in disordered fcc and ordered L1<inf>2</inf> Ni-Al-W alloys, J. Alloys Compd. 645 (2015) 259–268. doi:10.1016/j.jallcom.2015.04.154.

[125] R.D. Doherty, Grain Coarsening – Insights from Curvature Modeling Cyril Stanley Smith Lecture, Mater. Sci. Forum. 715 (2012) 1–12. doi:10.4028/www.scientific.net/MSF.715-716.1.

[126] C. Williams, Low-Loss and No-Loss Spectra and Images, Transm. Electron Microsc. (2009) 699–713.

[127] N. Schindzielorz, K. Nowak, S.B. Maisel, S. Mu, Phase behavior and mechanical properties of Ni – W studied by first-principles calculations and ab initio based thermodynamics, Acta Mater. 75 (2014) 307–315. doi:10.1016/j.actamat.2014.04.029.

[128] S.B. Maisel, N. Schindzielorz, S. Muller, H. Reichert, A. Bosak, An accidental visualization of the Brillouin zone in an Ni-W alloy via diffuse scattering, J. Appl. Crystallogr. 46 (2013) 1211–1215. doi:10.1107/S0021889813016270.

[129] R.S. Irani, R.W. Cahn, Order-Hardening of CuPt, Acta Metall. 21 (1973) 575–584.

[130] C.J. Marvel, P.R. Cantwell, M.P. Harmer, The critical influence of carbon on the thermal stability of nanocrystalline Ni–W alloys, Scr. Mater. 96 (2015) 45–48. doi:10.1016/j.scriptamat.2014.10.022.

[131] R. Cury, J.M. Joubert, S. Tusseau-Nenez, E. Leroy, A. Allavena-Valette, On the existence and the crystal structure of Ni4W, NiW, and NiW2 compounds, Intermetallics. 17 (2009) 174–178.

[132] J. Lee, C.R. Lear, X. Zhang, P. Bellon, R.S. Averback, Irradiation-Induced Nanoprecipitation in Ni-W Alloys, Metall. Mater. Trans. A. (2014). doi:10.1007/s11661-014-2704-4.

[133] S. Latif, M. Mehmood, J. Ahmad, M. Aslam, M. Ahmed, Z. Zhang, Ni–WC composite coatings by carburizing electrodeposited amorphous and nanocrystalline Ni–W alloys, Appl. Surf. Sci. 256 (2010) 3098–3106. http://www.sciencedirect.com/science/article/pii/S0169433209016936 (accessed August 1, 2013).

[134] M. Fielder, H.H. Stadelmaier, The Ternary System Nickel-Tungsten-Carbon, Zeitschrift Für Met. 402-404 (1975) 66.

[135] C.M. Fernandes, A.M.R. Senos, Cemented Carbide Phase Diagrams: A Review, Int. J. Refract. Hard Met. 29 (2011) 405–418.

[136] Y. Wang, C. Chen, Z. Zhang, J. Long, T. Xu, X. Liu, et al., Phase equilibria in the Al–C–Ni–W quaternary system, Int. J. Refract. Met. Hard Mater. 46 (2014) 43–51. doi:10.1016/j.ijrmhm.2014.05.002.

[137] A.O. Aning, Z. Wang, T.H. Courtney, Tungsten Solution Kinetics and Amorphization of Nickel in Mechanically Alloyed Ni-W Alloys, Acta Metall. Mater. 41 (1993) 165–174.

[138] A.W. Weeber, H. Bakker, Amorphization by ball milling. A review, Phys. B Condens. Matter. 153 (1988) 93–135. doi:10.1016/0921-4526(88)90038-5.

[139] Y. Kimoto, A. Giga, T. Ohkubo, Y. Takigawa, K. Hono, K. Higashi, Ni-W Amorphous/Nanocrystalline Duplex Composite Produced by Electrodeposition, Mater. Trans. 48 (2007) 996–1000. doi:10.2320/matertrans.48.996.

[140] R. Salzer, L. Lechner, K. Tysrulin, Reliable Solution for ultra-thin HRTEM Lamella Fabrication by means of BSE Thickness Mapping in Combination with the novel “X2” Preparation Method, Microsc. Microanal. 18 (2012) 654–655. doi:10.1017/S1431927612005120.

[141] R. Salzer, A. Graff, M. Simon, F. Altmann, Standard Free Thickness Determination of Thin TEM Samples via Backscatter Electron Image Correlation, Microsc. Microanal. 15 (2009) 340–341. doi:10.1017/S1431927609096457.

[142] J. Haimovich, K. Leibold, G. Staudt, Estimating and Measuring Thickness of Thin Layers by Monte Carlo Simulation and Backscattered Electron Image Analysis, AMP J. Technol. 5 (1996) 65–78.

[143] P. Hovington, D. Drouin, R. Gauvin, CASINO: A new Monte Carlo code in C language for electron beam interaction - Part I: Description of the program, Scanning. 19 (1997) 1–14. doi:10.1002/sca.4950190101.

[144] T. Malis, S.C. Cheng, R.F. Egerton, EELS log-ratio technique for specimen-thickness measurement in the TEM, J. Electron Microsc. Tech. 8 (1988) 193–200. doi:10.1002/jemt.1060080206.

[145] D.C. Joy, J.R. Michael, Modeling ion-solid interactions for imaging applications, MRS Bull. 39 (2014) 342–346. doi:10.1557/mrs.2014.57.

[146] J.R. Michael, Focused Ion Beam Induced Microstructural Alterations: Texture Development, Grain Growth, and Intermetallic Formation, Microsc. Microanal. 17 (2011) 386–397.

[147] J.R. Michael, Understanding Microstructural Changes in Metals Induced by Gallium Ion Beam Irradiation, Microsc. Microanal. 19 (2013) 884–885. doi:10.1017/S1431927613006417.

[148] A.J. Detor, Grain Size Control and Microstructural Evolution in Nanocrystalline Ni-W Alloys, MIT, 2007.

[149] J.J. English, Binary and ternary phase diagrams of columbium, molybdenum, tantalum, and tungsten, 1961.

Appendix A: TEM Sample Preparation

(S)TEM analysis of nanocrystalline materials requires samples that have the same thickness as the average grain diameter. Thin samples are necessary improve grain size measurements and EDS analysis of nanoscale phases. The procedural steps to make high quality TEM samples are listed below. The dimensions are x × y × z and the beam conditions are shown in parentheses.

1. A 15 µm × 2 µm × 50 nm Pt bar is deposited with the E-beam to minimize ion beam damage that may result with I-beam deposition (2 kV, 6 nA)
2. A 15 µm × 2 µm × 2 µm protective Pt was deposited with I-beam deposition to protect the sample from future milling and redeposition (30 kV, 300 pA)
3. Two 25 µm × 8 µm × 8 µm trenches were milled with a regular cross section milling pattern on each side of the Pt bar. Approximately 2 µm of space was left in-between the edge of the Pt bar and the edge of the milling pattern to avoid milling the Pt bar (30 kV, 30 nA)
4. The trench faces next to the Pt were polished with cleaning cross sections. The stage was tilted ± 3° to account for re-deposition at the bottom of the trench, and the final Pt bar width was reduced to 1-2 µm (30 kV, 7 nA)
5. The stage was tilted to 0° and the "u-cut" was milled (30 kV, 3 nA)
6. The 1 µm thick section was welded to the lift-out needle (30 kV, 50 pA)
7. The connecting bridge was removed and the sample was extracted (30 kV, 1 nA)
8. A "landing zone" was milled into a Omniprobe Mo grid to provide a clean edge to place the sample (30 kV, 60 nA)
9. The sample was attached to the grid (30 kV, 100 pA) and the needle was detached (30 kV, 1 nA)
10. The sample was thinned to roughly 750 nm alternating at ± 3° (30 kV, 1 nA)
11. The sample was thinned to roughly 300 nm alternating at ± 2° (30 kV, 300 pA)
12. The sample was thinned to roughly 150 nm alternating at ± 1.5° (30 kV, 100 pA) (*note – this large tilting angle created a wedge shape at the bottom of the specimen*)
13. Broad beam milling reduced the sample thickness to less than 100 nm and removed damage incurred from 30 kV thinning (5 kV, 48 pA)
14. The sample final polished in the NanoMill (900 eV, 150 pA)

Appendix B: TEM Sample Thickness Determination

In-situ thickness determination is critical to determine if the tilting angle is too steep (extreme wedge) or too narrow (inverse wedge). Other research groups have developed similar sample thickness determination techniques [140–142]. In this research, the accelerating voltage of the electron beam was adjusted between 3 kV and 15 kV, and images were taken using secondary electrons (SE) or backscattered electrons (BSE). Differences in image contrast between accelerating voltages are correlated to differences in the sample thickness because the electron traveling distance through the sample depends on the accelerating voltage. Table B.0.1 compares the interaction depths for SE and BSE electrons in a Ni-20 at.% W alloy that were simulated using the Casino (Monte Carlo) simulation [143].

Table B.0.1. Secondary and backscattered electron interaction depths in a Ni-20 at.% W alloy

kV	BSE Depth (nm)	SE Depth (nm)	kV	BSE Depth (nm)	SE Depth (nm)
1	3	6	**8**	75	170
2	8	18	**9**	90	210
3	15	31	**10**	110	240
4	23	52	**15**	220	510
5	34	76	**20**	340	840
6	43	96	**25**	540	1200
7	61	130	**30**	720	1700

Using the BSE and SE interaction depths, it is now possible to accurately determine sample thickness. If a Ni-W sample is 150 nm thick in some areas and if the electron beam is set to 8 kV, the 150 nm regions will appear relatively brighter in SE images relative to the thicker regions. Furthermore, if the acceleration voltage is lowered to 7 kV, the sample will have uniform intensity because the sample thickness is greater than the SE interaction

depth. The contrast in BSE images will be reverse. If BSE electrons pass through the sample, the region will appear dark because the electrons will not be detected. Figure B.0.1 shows multiple BSE images of a Ni-23 at.% W alloy imaged with different accelerating voltages. Again, the areas that appear dark indicate the sample is thinner than the thickness summarized in Table B.0.1. An initial diagnosis of this sample would be that the region at the bottom is thinner than 34 nm, but thicker than 8 nm. In addition, the majority of the sample is thinner than 110 nm but thicker than 34 nm. Overall, BSE images are used to determine the final sample thickness, and SE images are used during thinning to monitor the sample.

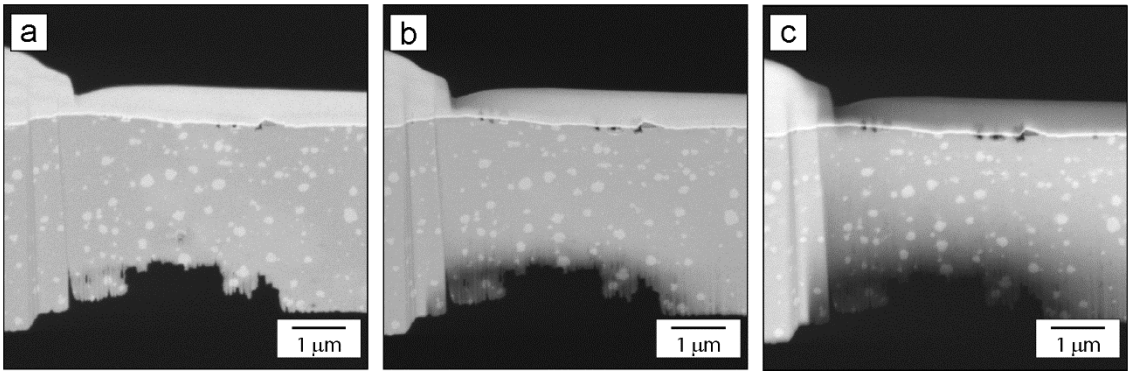

Figure B.0.1. BSE images collected to determine TEM sample thickness: (a) 2 kV, (b) 5 kV, and (c) 10 kV.

A series of BSE images are taken with different accelerating voltages to generate thickness maps. Once acquired, the images are converted into binary so that the pixels that appeared darker are given a value of 0 (*i.e.* BSE electrons transmitted through the sample), and pixels that were not darker are given a value of 1. Next, the images were aligned using a DigitalMicrograph™ script written by David Mitchell and added together. Now, each pixel in the summed image will a value between 0 and the number of summed images (n), where 0 is the thinnest regions and n is the thickest regions. Lastly, the image was converted

to RGB to more effectively expose differences in sample thickness. Figure B.0.2 shows sample thickness maps of the same specimen before and after NanoMilling. After directly comparing both maps, it is clear that the NanoMilling process removed roughly 20 nm.

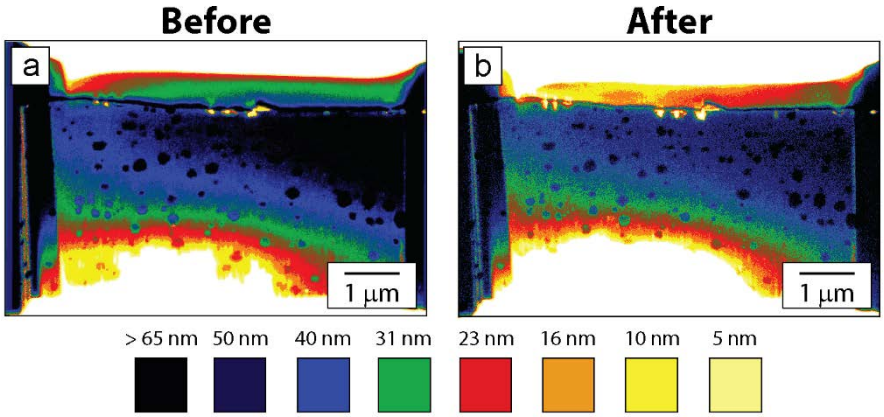

Figure B.0.2. BSE thickness maps before and after NanoMilling of a Ni-23 at.% W alloy.

A BSE thickness map was compared to an electron energy loss spectroscopy (EELS) thickness map to validate the BSE technique, and both are shown in Figure B.0.2. EELS thickness mapping is commonly used to determine sample thickness [126,144], but EELS is not readily available at Lehigh. Both maps were recorded from the same region of interest, and it is evident that the BSE thickness mapping technique is reliable. However, there is significant error in the BSE mapping. The accuracy of the BSE thickness map depends on simulated electron trajectories and the electron interaction distance threshold. In the maps presented above, a threshold value of 98% was chosen because the predicted BSE values matched well with the EELS results. Thus, if the BSE technique is used, the recommended threshold is 98%. Nonetheless, this technique may be used for quantitative thickness mapping, but it is in no regard an absolute method.

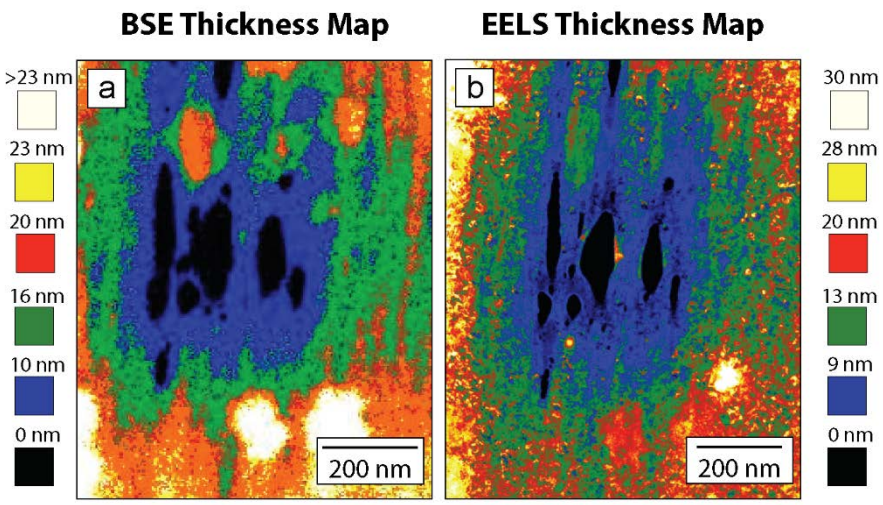

Figure B.0.3. Comparison between BSE and EELS thickness maps.

Appendix C: Ion-channeling Grain Size Determination

If the average grain size was too large to measure with TEM, but too small for more conventional electron backscatter electron diffraction techniques, ion-channeling contrast (iCC) images were used to determine the grain size distributions. Grains closely oriented to a low index direction appear darker. There is less ion interaction with the surface and subsequently less secondary electrons are emitted. The advantage of using iCC imaging is the higher analytical resolution (*i.e.* can quantify lower grain sizes). Electron backscattered diffraction (EBSD) generally has a 50 nm resolution limit. If grains are on that scale, the diffraction signal is noisy because the software struggles to determine if a pixel belongs to one of the neighboring grains. The disadvantages of iCC imaging are that it does not determine crystal orientations, it is time intensive to outline each grain boundary, and the risk of ion induced grain growth [145–147]. The grains analyzed during this research using iCC were over 100 nm and did not coarsen during imaging. Grains below 100 nm were analyzed by TEM-DF imaging. As a further precaution, images were collected with short pixel dwell times and integrated 10 times to limit temperature spikes that may be produced by long exposure times on a single pixel.

Approximately 10 images were taken of each alloy on polished cross sections to measure as many grains as possible. Adobe Photoshop was used to outline the grains, and ImageJ was used to extract individual grain sizes. The procedural steps to record iCC images and extract grain sizes are listed below:

1. Polished samples were etched with 1 nA until the maximum contrast was reached.
2. The imaging conditions were 3072 pixels × 2048 pixels, 50 pA ion beam current, 1 μs dwell time, 10 integrated frames, and 8-bit black/white TIFF format.

3. The images were imported into Photoshop and converted into RGB to change the outline color to red (grey outlines are hard to see in black/white images).
4. A new image layer was placed above the raw image file to outline the boundaries and the scale bar was re-drawn onto the outline layer.
5. All grain boundaries were traced with a 2 pixel wide brush.
6. Completed outline layers were exported as TIFF files.
7. The TIFF files were imported into ImageJ and calibrated using the scale bar.
8. The image was converted to greyscale and thresholded to select the boundaries.
9. The analyze particle size function was used, and the boxes labeled display results, clear results, summarize, and exclude on edges were selected. Dhow masks was also chosen in the dropdown menu.
10. Each file was saved and the calculated areas in the Results file were converted to equivalent spherical diameters.

Figure C.0.1 shows the outlines and masks analyzed images of the Ni-12 at.% W annealed at 728 °C and the Ni-17 at.% W alloy annealed at 1019 °C. Grains on the image dissected by the image borders or sample surface were excluded.

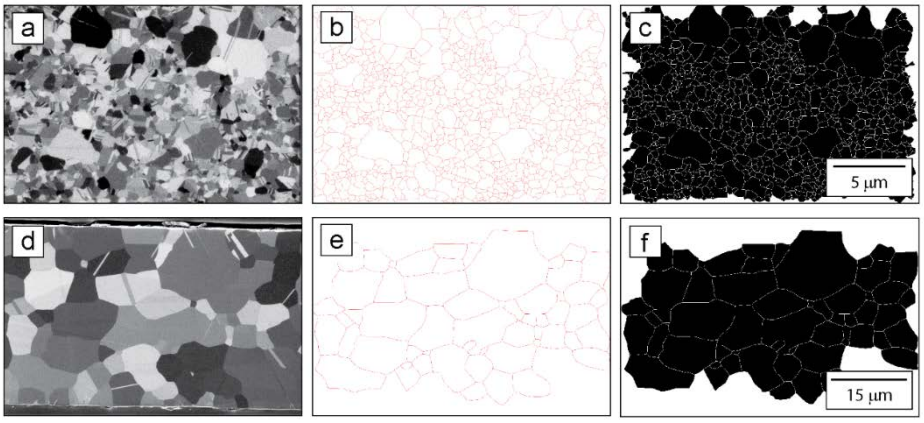

Figure C.0.1. Grain size analysis using iCC imaging of (a-c) Ni-12 at.% W alloy annealed at 728 °C for 24 hrs and (d-f) Ni-17 at.% W alloy annealed at 1019 °C for 24 hrs. Images (a,d) are the raw images, (b,e) are the outline layers, and (c,f) are the masks.

Vita

Christopher J. Marvel was born on October 3, 1989 to Richard and Nancy Marvel. He was raised in Ellicott City, MD with his younger sister Jessica. He attended Mt. Hebron High School and graduated in 2008. Chris then enrolled at Lehigh University in the P.C. Rossin College of Engineering, and later graduated with a Bachelor of Science in Materials Science and Engineering in 2012. Afterwards, Chris joined Dr. Martin Harmer's research group to study thermal stability of nanocrystalline materials, and also collaborated with Dr. Wojciech Misiolek and Dr. Masashi Watanabe on characterizing electron beam welded titanium. During his time at Lehigh, Chris contributed to teams that won several microscopy honors, including the Jacquet-Lucas and George L. Kehl awards for excellence in metallography in 2011, and the Roland B. Snow award for the best in show of the ceramographic competition at MS&T in 2014. During graduate school, he was also awarded the 2015 Lehigh Valley Chapter of ASM International Outstanding Young Member Award for his efforts in organizing the ASM sponsored Student Materials Camps in the summers of 2014 and 2015. After graduation Chris will remain in Dr. Harmer's research group as a post-doctoral research associate.